Identifying relativistic effects in the light-matter interaction between a high-intensity laser pulse and a one-dimensional atomic model

Master Thesis in Physics

Anders Oskar Herland Dalseng

Department of Physics and Technology

Universiy of Bergen

December 13, 2021

Acknowledgements

Submitting this thesis, I am reminded of how many people that were essential to me making it here. Without the people around me support and encourage me along the way, this dream would never have come through.

To my supervisor Morten Førre, I wish to declare my sincerest appreciation for the enormous effort and constant support. It takes a special kind of professor to be as giving as you.

To my mother Astrid and my father Geir, without which I would quite literally not exist. You've facilitated my curiosity for as long as I can remember, and I will be forever grateful for it.

To my partner Sarra, for your steady support and for helping me focus on the important things in life,

to my stepbrother and roommate Johan, who for years has tolerated my unsolicited physics lectures,

and to everyone whose previous work I have been able to rely on,

this work would not have been completed without any of you.

Abstract

In this thesis, I intend to study the mechanisms that unfold during the light-matter interactions between an atomic system and a high-intensity laser. In an effort to investigate the system in its smallest components, the system is interpreted as a one-dimensional hydrogenic atom with a central potential. As the Coulomb-potential lacks a one-dimensional equivalent, it is approximated by a soft-core potential. Stationary solutions to the modelled 1D system will be represented in some B-spline basis, yielding solutions in both Dirac and Schrödinger frameworks. From these solutions, time can be introduced to the modelled systems, and the light-matter interaction will be regarded. The modelled system is exposed to the high-intensity laser for a short time, and the excitation energy of the electron is used as a measure for relativistic effects within the system. Initially, the Dirac and Schrödinger modelled systems will interact near identically to one another, and relativistic effects cannot be observed. Later, by adjusting the basis from which the time-dependent Dirac equation is solved, the relativistic effects can be seen in the one-dimensional system.

Contents

Chapter 1

Introduction and background

1.1 On the laser and light-matter interaction

The laser has, since its inception in 1960[21], enabled humanity to achieve things that are incomprehensible to many among us. It enables the functionality of DVDs and fibre-optic communication, can cut through thick sheets of metal, and can even be used in medicine to combat tumours. More importantly, at least pertaining to the current work, is the laser's persistence as an invaluable tool in the pursuit of further understanding the inner workings of the universe. Being able to precisely influence systems governed by quantum mechanics has led to entire new fields of research within physics, as well as in other realms of science. One such field, under which the majority of the contents of this thesis fall, is the study of light-matter interactions of an atom in a high-intensity laser field.

Research of light-matter interactions in high-intensity laser fields has been a topic prevalent in physics for decades[4, 15, 24, 6, 5, 7, 19, 26, 11]. As with all things on the quantum scale, physically observing individual processes require tremendous time, funding, and effort, without any guarantee of achieving reliable observations. Separate physical mechanisms can manifest their effects on a system in complex ways, making them difficult to disentangle and describe independently. As such, we are nudged in the direction of theoretical research - attacking the problem with pen, computer, and the intent to predict how the physical world will unfold itself. This does not imply, however, that investigating the quantum world in this way is a breeze. With choices of which frameworks, approximations, and corrections to include - or exclude - from one's calculations, one faces the risk of leaving out some crucial component of the physical problem one had set out to investigate.

1.2 Common approaches to the research of light-matter interactions

The world, as we understand it, is often described as 3+1 dimensional, with three spatial dimensions plus time[17]. Precise calculations in this framework demand significant computational power to carry out, while also requiring whoever might attempt to solve such problems be particularly meticulous in composing it. The most important tools in this type of research comes in the form of approximations and corrections to the time-dependent Schrödinger equation [9, p. 131],

$$i\hbar\frac{\partial\Psi(\vec{x},t)}{\partial t} = -\frac{\hbar^2}{2m}\nabla^2\Psi(\vec{x},t)\,, \tag{1.1}$$

as well as the inherently relativistic Dirac equation [17, p. 57].

$$i\hbar\frac{\partial\Psi(\vec{x},t)}{\partial t} = \left[-i\hbar c\boldsymbol{\alpha}\cdot\nabla + \beta mc^2\right]\Psi(\vec{x},t) \tag{1.2}$$

A common approach to simplifying the light-matter interactions of an atom in an external laser field is to apply the dipole approximation. In doing this, one can essentially remove the spatial dependency of the laser's electric field, while also discarding the effects of its magnetic field. This non-relativistic approximation does come with some constraints for the intensity and frequency of the incident laser, however. As the intensity and/or frequency of the laser goes up, relativistic effects must be given higher importance when trying to describe the system. This is most often done by introducing relativistic or semi-relativistic corrections to the TDSE.

1.3 Skewed energy probability differential

Exposing a model hydrogenic atom to a high-intensity laser potential can stimulate the emission of the electron[9]. Theoretical research in a TDSE framework on this sort of system can, depending on the set of approximations and corrections being applied, produce significantly different results from other sets of approximations [28, 14, 6, 15, 24]. Given photons of equal energy, classically, one could assume that the energy spectrum of the emitted electrons would have peaks near integer multiples of the photon energy. Through recent numerical research, however, this is not always the case, and the multi-photon resonance peaks appear to shift out of integer amounts of laser-emitted monochromatic photons depending on which approximations are being used [31, 7, 8].

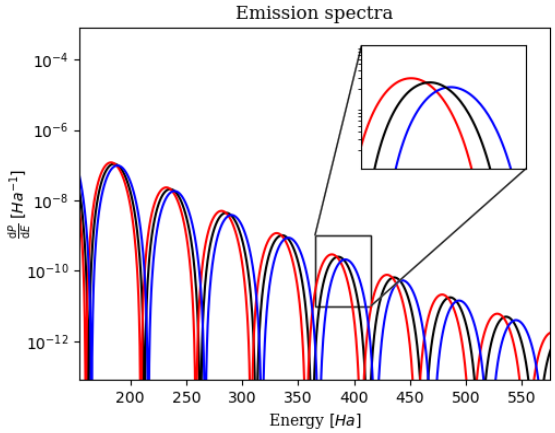

Figure 1.3: Illustration of skewed electron emission spectre. The primary axis corresponds to the energy of the emitted electron, while the secondary axis signifies the probability of observing an electron with this energy as a function of the density of energy states in its proximity. The black curve corresponds to emissions where the probability peaks are exactly 50 Ha apart, while the red and blue curves corresponds to the shifts resulting from differences in the model used.

Figure 1.3 is an exaggerated illustration meant to express the findings from [31, 7, 8], and is not the result of any physical model. The intent is to show the variation in results, from different sets of approximations and corrections, for some 3D model hydrogenic atom that has been exposed to a high-intensity laser pulse. The inclusion of relativistic effects seems to increase the distance between peaks corresponding to multi-photon resonances in the emission spectrum (blue shift, Fig. 1.3), while including higher-order terms of the dipole approximation tends to move these peaks closer to one another (red shift, Fig. 1.3). Furthermore, with these shifts being of similar magnitude and opposite directions, they nearly exactly cancel each other out when both are taken into account. Further research is being done on this problem to determine how the model can be represented precisely in a numerical framework. Still, as earlier noted, three dimensional models of light-matter interactions tend to be very computationally involved, and many approximations are still essential to their methods.

In the effort of identifying specific mechanisms in composite systems, such as the light-matter interaction found in three-dimensional hydrogenic atom models in the presence of a high-intensity laser field mentioned above, reducing the problem to its smallest parts can potentially be useful.

1.4 One-dimensional model

Previous research [13, 15, 26] has taken a peculiar approach to investigate the mechanisms involved in such systems as described in sec. 1.3, namely by reducing the dimensionality of the system. By doing away with two of the spatial dimensions altogether, the dipole approximation is no longer an approximation of the system - but an inherent attribute of the one-dimensional variant. Assuming that the laser encompasses an area which is orders of magnitude larger than the atom being

considered, there is no longer any spatial dependency for the light-matter interaction between the electron and photons. Previous studies have made efforts to devise accurate (within the one-dimensional framework, at least) mathematical models for the 1D atom, both in regards to the Coulomb-potential and the electron "orbits" [13, 15, 28].

Besides previous research in this field, there are other good arguments for why one-dimensional models have applications in physical research. Many problems in classical mechanics can be analytically reduced to one dimension by substitution of variables [18], sometimes even allowing for applications within a relativistic regime. Furthermore, in systems where interaction with a magnetic field is of little significance, reducing a system containing electromagnetic fields to one dimension allows for simple inspection of such system if the polarization is aptly chosen.

While discussing the results found from studying some numerical one-dimensional model of a real-world system, having concerns regarding their validity would be justified. Any such model could be articulated as a vastly simplified interpretation of the quantum mechanical framework, a framework that itself is a simplified interpretation of the real world. As such, and as with any scientific research, the intention should not be to find some definitive proof or exact explanation of any physical phenomena. Rather, the goal should be to make accounts of such phenomena from different perspectives, so as to further the wealth of information one could review in an effort to gain a better understanding of the world. My argument for the validity of this work, based on the current paragraph as well as the paragraphs above, is this: The investigation of a numerical, one-dimensional model of a hydrogenic atom, in the presence of a high-intensity laser potential, could grant some insight into the light-matter interactions that are present in the physical, real-world system.

1.5 Aim and approach of the thesis

After the introductions made above, it is opportune to present the main goals of this thesis.

It is my intention within this thesis to investigate the energy emission spectra of one-dimensional hydrogenic model atom interacting with a high-intensity laser beam, within the confines of both the Schrödinger equation and the Dirac equation. This will initially be done by constructing time-independent models in the B-spline basis, with the intent to solve the resulting eigenvalue problems. The solutions to these problems, in the form of energy levels and wave functions, will then be used as a basis to investigate the time-dependent light-matter interactions between these model atoms and the laser pulse. The resulting energy-emission spectra will be discussed in regard to their convergence and differences. The ionization probabilities will be commented on, and possible future applications for these models will be considered.

This thesis will have as its main goal to determine whether the shifts in the energy spectra (as illustrated in Fig. 1.3), corresponding to multi-photon resonances in a one-dimensional model, can be observed.

1.6 Atomic units

For ease of notation, all formulas and equations are written in atomic units. The SI values of all physical constants given in the table below are found in [30].

Physical Unit	Symbol	Physical origin	Value (SI)	Value (a.u.)	Expression
Mass	m_e	Electron mass	$9.109 \cdot 10^{-31}\, kg$	1 a.u.	
Charge	e	Absolute value of electron charge	$1.602 \cdot 10^{-19}\, C$	1 a.u.	
Action	$\hbar$	The reduced Planck constant	$1.055 \cdot 10^{-34}\, Js$	1 a.u.	
Length	a_0	Bohr radius for atomic hydrogen	$0.529 \cdot 10^{-10}\, m$	1 a.u.	
Energy	E_h	$E_{g.s.}$ of atomic hydrogen	$4.359 \cdot 10^{-18}\, J$	1 a.u.	$\frac{\hbar^2}{m_e a_0^2}$
Permittivity	$\frac{1}{4\pi\epsilon_0}$	Permittivity factor in vacuum	$8.988 \cdot 10^{9}\, \frac{Nm^2}{C^2}$	1 a.u.	$\frac{a_0 \hbar^2}{m_e e^2}$
Fine-structure constant	α	Electromagnetic interaction	$7.297 \cdot 10^{-3}$	$\simeq 1/137$	
Velocity	c	Speed of light in vacuum	$2.998 \cdot 10^{8}\, m/s$	$\simeq 137$ a.u.	$\frac{a_0 E_h}{\hbar \alpha}$

Table 1.6: List of atomic units for use in calculations.

Specifically regarding the Somerfield fine-structure constant α, calculations within the present work will use the 2018 CODATA recommended value [30].

$$\alpha \coloneqq 7.2973525693 \cdot 10^{-3} \tag{1.3}$$

Consequently, the speed of light in vacuum c, which in atomic units is expressed as $c = \frac{1}{\alpha}$ has the following value:

$$c \coloneqq 137.035999084 \tag{1.4}$$

1.7 Formalisms and naming conventions

Mathematical operation	Effect
Hermitian conjugate of a square matrix	$\begin{pmatrix} a_{1,1} & a_{1,2} & \cdots & a_{1,n} \\ a_{2,1} & a_{2,2} & \cdots & a_{2,n} \\ \vdots & \vdots & \ddots & \vdots \\ a_{n,1} & a_{n,2} & \cdots & a_{n,n} \end{pmatrix}^{\dagger} \coloneqq \begin{pmatrix} a^*_{1,1} & a^*_{2,1} & \cdots & a^*_{1,n} \\ a^*_{1,2} & a^*_{2,2} & \cdots & a^*_{2,n} \\ \vdots & \vdots & \ddots & \vdots \\ a^*_{1,n} & a^*_{2,n} & \cdots & a^*_{n,n} \end{pmatrix}$
Hermitian conjugate of a vector	$\begin{pmatrix} a_1 \\ a_2 \\ \vdots \\ a_n \end{pmatrix}^{\dagger} = \begin{pmatrix} a^*_1 & a^*_2 & \cdots & a^*_n \end{pmatrix}$

Object	Symbol		Definition
Identity matrix	$\mathbb{I}_n$	$\coloneqq$	$\begin{pmatrix} 1 & 0 & \cdots & 0 \\ 0 & 1 & \cdots & 0 \\ \vdots & \vdots & \ddots & \vdots \\ 0 & 0 & \cdots & 1 \end{pmatrix}_{n \times n}$
Kronecker delta	$\delta_{i,j}$	$\coloneqq$	$\begin{cases} 1, & i = j \\ 0, & i \neq j \end{cases}$
Inner product (Analytic)	$\left\langle A \middle\vert \hat{Q} \middle\vert B \right\rangle$	$\coloneqq$	$\int_\Omega A^\dagger (\hat{Q} B)\, dx$, where $\hat{Q}$ is an arbitrary operator
Inner product (Numerical, 1D)	$\left\langle A \middle\vert \hat{Q} \middle\vert B \right\rangle$	$\coloneqq$	$\int_a^b A^\dagger (\hat{Q} B)\, dx$, where $\hat{Q}$ is an arbitrary operator and $a, b \in \mathbb{R}$ are bounded numbers satisfying $a < b$
Time-dependent wave-function	Ψ	$\coloneqq$	$\Psi(x, t)$
Time-independent wave-function	ψ	$\coloneqq$	$\psi(x)$
Pauli matrices	σ_1	$\coloneqq$	$\begin{pmatrix} 0 & 1 \\ 1 & 0 \end{pmatrix}$
	σ_2	$\coloneqq$	$\begin{pmatrix} 0 & -i \\ i & 0 \end{pmatrix}$
	σ_3	$\coloneqq$	$\begin{pmatrix} 1 & 0 \\ 0 & -1 \end{pmatrix}$

For minimal coupling, the following convention will be used within the present work:

$\begin{matrix} p \to p + qeA \\ E \to E + qe\phi \end{matrix}$, where $qe \coloneqq -1\, a.u.$ is the charge of a single electron.

In mathematical expressions, this is shortened to $\begin{matrix} p \to p - A \\ E \to E - \phi \end{matrix}$, for ease of notation.

All illustrations presented within this thesis are created by the author. For a handful of illustrations presented in chapter 4, some input data for graphs were contributed by M. Førre. When this is the case, it will be explicitly stated. The process of making all illustrations contained within the current work has been done by using the Python-package MATPLOTLIB v.3.3.4 [12].

This thesis has been written in a free, open source TEX/LATEX interpreter, LYX [29].

Chapter 2

Theory and derivations of formulae

2.1 More about emission spectra

The system that is to be considered in the present work is a hydrogenic atom in the presence of an external vector field. More precisely, the aim is to investigate the emission spectra of the electron after interacting with the pulse. This is to be done numerically by modeling the system in one spatial dimension, within both the Dirac and Schrödinger framework. The current chapter will describe the approach taken in the effort to facilitate this, before presenting theory, formulae, and approximations pertinent to the current work. Looking at the problem which was posed in sec. 1.5 is composed of several different elements, and some room is set aside to give a brief explanation of how the present work will go about to solve it.

First and foremost, to describe a quantum mechanical system, one needs a framework on which the description will be based. As previously stated, the present work aims to compare findings from models based on Dirac and Schrödinger, in an effort to describe differences between them. It is therefore necessary to examine the methods and applications for both of these, as well as how they can eventually be translated into numerical models. These models, upon which most of the presented results will be based, are also to be confined to a single spatial dimension. As such, great care must be taken when considering how the Dirac and Schrödinger equations change when applied in such a way.

In describing the transitions from three to one spatial dimensions, the Dirac (TDDE) and Schrödinger (TDSE) equations are to be presented in many shapes. In their general forms, they are partial differential equations which can be used to predict how the configuration of a system evolves in time [9, 17]. For the predictions put forth from these equations to be precise, it is necessary to apply them to well-defined descriptions of the systems they are to evolve.

The basis for the time-evolution of the system will be constructed by solving the eigenvalue problems arising from the applications of the time-independent Dirac (TIDE) and Schrödinger (TISE) equations. Both of these equations give accurate predictions for the energy levels of 3D hydrogenic atoms, where the Coulomb-potential can be represented without much issue. This potential does not, however, have

a well-defined analytic transformation into 1D, and the TIDE and TISE must be adjusted to ensure their applicability within the confines of such a model.

After the adapting these equations to a 1D numerical model, the process to solve the eigenvalue problems that arise from them will be discussed. The eigenstates resulting from this process will then be used as a starting point for the system which will be subjected to a high-intensity laser pulse. To express this time-evolution, appropriate one-dimensional interpretations of the TDDE and TDSE will be utilised, and the final product will be formulated. This will be presented as the emission spectra of the emitted electron, in the form of a probability differential with regard to the density of energy states.

2.2 3D Dirac

The time-dependent three-dimensional Dirac equation (3D TDDE) for a free electron in atomic units is given by (1.2).

$$i\frac{\partial\Psi(\vec{x},t)}{\partial t} = \left[c\boldsymbol{\alpha}\cdot\hat{\mathbf{p}} + \beta c^2\right]\Psi(\vec{x},t) \tag{2.1}$$

This equation is the starting point for future calculations relating to the Dirac framework. As noted, this equation has proven exceedingly difficult to find converging solutions for. To make a solution more manageable, it is simplified to act on an electron constrained to movement in only the direction of polarization for the electric field.

First it is necessary to express this equation using a Hamiltonian and its corresponding energy. This is done by assuming that $\Psi(\vec{x},t)$ can be written on the form

$$\Psi(\vec{x},t) = \psi(\vec{x})\cdot e^{-iEt}\,, \tag{2.2}$$

which when differentiated with regards to time returns

$$i\frac{\partial\Psi(\vec{x},t)}{\partial t} = i\psi(\vec{x})\frac{\partial}{\partial t}(e^{-iEt}) = E\psi(\vec{x})e^{-iEt} = E\Psi(\vec{x},t)\,. \tag{2.3}$$

The three-dimensional momentum operator $\hat{\mathbf{p}}$ is defined as

$$\hat{\mathbf{p}} \coloneqq -i\nabla\,. \tag{2.4}$$

By performing the substitutions stated by the minimal coupling rule [9, p. 181], namely

$$\hat{\mathbf{p}} \to \hat{\mathbf{p}} - \vec{A} = -i\nabla - \vec{A}\,, \tag{2.5}$$

and

$$E \to E - \phi\,, \tag{2.6}$$

equation (2.1) can be expanded to include electric fields.

$$E\Psi(\vec{x},t) = \left[c\boldsymbol{\alpha}\cdot\left(-i\nabla - \vec{A}\right) + \beta c^2 + \mathbb{I}_4\phi\right]\Psi(\vec{x},t) \tag{2.7}$$

From the dipole approximation, the spatial dependency of the vector field is ignored ($\vec{A} \to \vec{A}(t)$, or $\nabla\cdot\vec{A} = 0$), and the vector field can be expressed as only a function of time. The vector field is for now assumed to be zero ($\vec{A}(t=0) = 0$), but will be reintroduced later.

The scalar potential ϕ which was introduced by minimal coupling is assumed to be a Coulomb potential, which in atomic units can be expressed as

$$\phi \to \phi(r) = -\frac{z}{|\vec{r}|} \tag{2.8}$$

To further explore equation (2.7), a common representation of the $\boldsymbol{\alpha}$ and β matrices are the Dirac matrices, given by

$$\beta = \gamma^0 = \begin{pmatrix} \mathbb{I}_2 & 0 \\ 0 & -\mathbb{I}_2 \end{pmatrix} \tag{2.9}$$

$$\boldsymbol{\alpha} = \alpha^i = \gamma^0\gamma^i = \begin{pmatrix} 0 & \sigma_i \\ \sigma_i & 0 \end{pmatrix}, \qquad i = 1,\, 2,\, 3 \tag{2.10}$$

where σ_i are the Pauli spin matrices.

The 3D TIDE (2.1) can, with $\Psi(\vec{x}, t=0) = \psi(\vec{x})$ at $t = 0$ (2.2), be expressed as

$$E\psi(\vec{x}) = \left[c\boldsymbol{\alpha}\cdot\mathbf{p} + \beta c^2 + \mathbb{I}_4\phi(x)\right]\psi(\vec{x}) \tag{2.11}$$

From the RHS of this equation, the Hamiltonian can simply be extracted:

$$H_{3D}^{TIDE} = \left[c\boldsymbol{\alpha}\cdot\mathbf{p} + \beta c^2 + \mathbb{I}_4\phi(\vec{x})\right] \tag{2.12}$$

For the three dimensional system, multiple attempts have been made to simulate the energy probability differential to as high accuracy as possible. This does, due to the complexity of the system, pose some requirements to approximations along the way. In this framework (as with most numerical calculations), any result found by simulating some model of a physical system can be heavily influenced by whichever approximations have been made. Therefore, in the effort of simplifying this system, it will in this work instead be simulated in one dimension. This removes the need for dipole approximations, as there is no possibility of the electromagnetic field of the photon beam to have any spatial dependency. The axis of movement is chosen to be co-directional with the polarization of the electric field carried by the photons, to further investigate their effect on electron energy.

2.3 Representing the Dirac equation in one spatial dimension

To justify the removal of two spatial dimensions from the Dirac equation, it must undergo significant changes. Most easily apparent is the momentum operator $\hat{\mathbf{p}}$ (2.4)

$$\hat{\mathbf{p}} \rightarrow \hat{\mathrm{p}} \equiv -i\frac{\partial}{\partial x} \tag{2.13}$$

which can only retain one of its components. A good starting point for derivation of the 1D time-independent Dirac equation is to consider the relativistic energy-momentum relation

$$E = c\sqrt{p^2 + m^2c^2} \tag{2.14}$$

By assuming, as Dirac did, that the expression under the square root can be rewritten as a sum of matrices and operators, eq. (2.14) can be expressed in atomic units as

$$\hat{H} = c\alpha\hat{\mathrm{p}} + \beta c^2 \tag{2.15}$$

Still, the following constraints must be placed on the α and β matrices:

$$\begin{aligned} \mathrm{tr}(\alpha) &= \mathrm{tr}(\beta) &&= 0 \\ \alpha^2 &= \beta^2 &&= \mathbb{I}_2 \\ &\{\alpha, \beta\} &&= 0_2 \end{aligned}$$

A set of already known matrices that fulfill these conditions are the Pauli spin-matrices.

$$\sigma_1 \equiv \begin{pmatrix} 0 & 1 \\ 1 & 0 \end{pmatrix}, \quad \sigma_2 \equiv \begin{pmatrix} 0 & -i \\ i & 0 \end{pmatrix}, \quad \sigma_3 \equiv \begin{pmatrix} 1 & 0 \\ 0 & -1 \end{pmatrix}$$

As any pairing of two spin-matrices are valid, it becomes trivial to choose two from the three to form the required basis for our 1D Dirac equation. For ease of calculation, the β matrix is set as $\beta \rightarrow \sigma_3$, while the α matrix (which now only retains one of its three configurations) is defined as $\alpha \rightarrow \sigma_2$.

The 1D Dirac Hamiltonian from (2.15) for a free particle can now be rewritten as

$$H_{1D}^{fp,Dirac} = \left[c\sigma_2\hat{\mathrm{p}} + \sigma_3 c^2\right] \tag{2.16}$$

Using this, as well as the energy operator $\hat{H} = i\frac{\partial}{\partial t}$, gives rise to the 1D TDDE for a free particle.

$$i\frac{\partial\Psi(x,t)}{\partial t} = \left[c\sigma_2\hat{\mathrm{p}} + \sigma_3 c^2\right]\Psi(x,t) \tag{2.17}$$

By applying the substitutions provided by minimal coupling to this equation, the 1D TDDE can be expanded to include its interaction with the scalar and vector fields.

$$i\frac{\partial\Psi(x,t)}{\partial t} = \left[c\sigma_2(\hat{\mathrm{p}} - A) + \sigma_3 c^2 + \mathbb{I}_2\phi\right]\Psi(x,t) \tag{2.18}$$

The scalar potential $\phi = \phi(x)$ is assumed to be some one-dimensional model of the 3D Coulomb potential (2.8). Coulomb potentials on this form do, however, introduce some problematic properties in one dimension. While the electron can take any arbitrary path around the nucleus in a three dimensional world, there exists no such option in 1D. Corrections must therefore be made to avoid the singularity of the Coulomb potential at $x = 0$. A plethora of models for the one-dimensional Coulomb potential have been investigated (see [10, 28] and references therein), with a wide variety of attributes. For this thesis, the most important bound state of the system is the ground state, and the soft-core potential expressed in [28] will suffice. The one-dimensional scalar potential $\phi = \phi(x)$ will, for the remainder of this thesis (unless explicitly stated) be defined by

$$\phi(x) = -\frac{z}{\sqrt{x^2 + \xi}}\,, \qquad \xi = \frac{2}{z^2}\,, \tag{2.19}$$

with z as the proton number for the nucleus. Now considering the vector potential, by applying the same arguments as with the dipole approximation, the vector field $A = A(t)$ is assumed to be exclusively time-dependent. Including these assumptions in eq. (2.18) yields an expression for the 1D TDDE, which will be the starting point for further calculations.

$$i\frac{\partial\Psi(x,t)}{\partial t} = \left[c\sigma_2(\hat{\mathrm{p}} - A(t)) + \sigma_3 c^2 + \mathbb{I}_2\phi(x)\right]\Psi(x,t)\,, \tag{2.20}$$

From this equation, the corresponding Hamiltonian can be easily extracted.

$$H_{1D}^{TDDE} = \left[c\sigma_2\left(-i\frac{\partial}{\partial x} - A(t)\right) + \sigma_3 c^2 + \mathbb{I}_2\phi(x)\right] \tag{2.21}$$

2.3.1 Deriving the 1D TIDE

To describe the time-evolution of the system, it is useful to first find the eigenstates of the time-independent system. By separating the wave function $\Psi(x,t)$ into its space and time-dependent components,

$$\Psi(x,t) = \exp(-iEt)\psi(x), \tag{2.22}$$

and then performing the time-derivative from the LHS, the equation (2.20) takes the form

$$E\Psi(x,t) = H_{1D}^{TDDE}\Psi(x,t) \tag{2.23}$$

Now, setting $t = 0 \Longrightarrow \begin{cases} \Psi(x, t=0) &= \psi(x) \\ A(t=0) &= 0 \end{cases}$, the 1D Dirac equation can be expressed without time-dependence

$$E\psi(x) = \left[c\sigma_2\hat{\mathrm{p}} + \sigma_3 c^2 + \mathbb{I}_2\phi\right]\psi(x)\,, \tag{2.24}$$

with corresponding Hamiltonian

$$H_{1D}^{TIDE} = \left[c\sigma_2\hat{\mathrm{p}} + \sigma_3 c^2 + \mathbb{I}_2\phi\right] \tag{2.25}$$

Writing this Hamiltonian on matrix form, with the momentum-operator represented explicitly, yields

$$H_{1D}^{TIDE} = \left[\begin{pmatrix} 0 & -c\frac{d}{dx} \\ c\frac{d}{dx} & 0 \end{pmatrix} + \begin{pmatrix} c^2 & 0 \\ 0 & -c^2 \end{pmatrix} + \begin{pmatrix} \phi & 0 \\ 0 & \phi \end{pmatrix}\right] = \begin{pmatrix} c^2+\phi & -c\frac{d}{dx} \\ c\frac{d}{dx} & -c^2+\phi \end{pmatrix} \tag{2.26}$$

The 1D TIDE (2.24) can now be expressed with the Hamiltonian (2.26),

$$E\psi = H_{1D}^{TIDE}\psi = \begin{pmatrix} c^2+\phi & -c\frac{\mathrm{d}}{\mathrm{d}x} \\ c\frac{\mathrm{d}}{\mathrm{d}x} & -c^2+\phi \end{pmatrix}\psi \tag{2.27}$$

From this, the wave function $\psi = \psi(x)$ must be expressed in the way of spinors.

$$\psi = \begin{pmatrix} P(x) \\ Q(x) \end{pmatrix} = \begin{pmatrix} P \\ Q \end{pmatrix}, \tag{2.28}$$

where $P = P(x)$ and $Q = Q(x)$ represent the large and small components of the 1D Dirac wave spinor, respectively.

As the solution to the Dirac equation can be represented as a linear combination of an infinite amount of eigenstates, one can write the total wave function ψ as

$$\psi = \sum_{n=1}^{\infty} c_n\psi_n\,, \tag{2.29a}$$

$$\psi = \sum_{n=1}^{\infty} c_n \begin{pmatrix} P_n \\ Q_n \end{pmatrix} \tag{2.29b}$$

Now, substituting the expression for ψ from (2.29a) into eq. (2.27), one can in bracket notation write

$$\sum_{n=1}^{\infty} c_n E_n \left|\psi_n\right\rangle = \sum_{n=1}^{\infty} c_n H_{1D}^{TIDE} \left|\psi_n\right\rangle \tag{2.30}$$

From this equation it is useful to apply the orthonormality condition for eigenstate solutions to the Dirac equation. This is done by multiplying the above equation with an arbitrary eigenstate $\langle\psi_k|$ from the left, and then finding the inner product.

$$\sum_{n=1}^{\infty} c_n E_n \langle\psi_k|\psi_n\rangle = \sum_{n=1}^{\infty} c_n \left\langle\psi_k\middle|H_{1D}^{TIDE}\middle|\psi_n\right\rangle \tag{2.31}$$

In the case of analytical models, the inner product on the LHS of (2.31) could be reduced by enforcing orthonormality on the system, allowing for the use of the Kronecker delta $\langle\psi_k|\psi_n\rangle = \delta_{k,n}$. By doing this, all terms of the infinite series except the case where $n = k$ vanishes, and the above equation can be expressed as

$$c_k E_k = \sum_{n=1}^{\infty} c_n \left\langle\psi_k\middle|H_{1D}^{TIDE}\middle|\psi_n\right\rangle \tag{2.32}$$

Writing out the inner product of the RHS in the way of vectors and matrix yields

$$\begin{aligned} c_k E_k &= \textstyle\sum_{n=1}^{\infty} c_n \int_{-\infty}^{\infty} \left[\begin{pmatrix} P_k(x) \\ Q_k(x) \end{pmatrix}^{\dagger} \begin{pmatrix} c^2+\phi(x) & -c\frac{\mathrm{d}}{\mathrm{d}x} \\ c\frac{\mathrm{d}}{\mathrm{d}x} & -c^2+\phi(x) \end{pmatrix} \begin{pmatrix} P_n(x) \\ Q_n(x) \end{pmatrix} \right] dx \\ &= \textstyle\sum_{n=1}^{\infty} c_n \int_{-\infty}^{\infty} \Big[P_k^*(x)\cdot\big(c^2+\phi(x)\big)\cdot P_n(x) - cP_k^*(x)\cdot\frac{\mathrm{d}Q_n(x)}{\mathrm{d}x} + \\ &\qquad + cQ_k^*(x)\cdot\frac{\mathrm{d}P_n(x)}{\mathrm{d}x} + Q_k^*(x)\cdot(-c^2+\phi(x))\cdot Q_n(x)\Big]\, dx \end{aligned} \tag{2.33}$$

By doing this for every eigenstate $\langle\psi_k|$, the above equation can be expressed as an infinite matrix equation in the form of a general eigenvalue problem,

$$A\vec{x} = \lambda\vec{x} \tag{2.34}$$

where A has matrix elements $A_{k,n} = \left\langle\psi_k\middle|H_{1D}^{TIDE}\middle|\psi_n\right\rangle$, the eigenvalue $\lambda = E$ is the energy of the system, and the eigenvector $\vec{x} = \vec{c} = \begin{pmatrix} c_1 \\ c_2 \\ \vdots \end{pmatrix}$ gives the coefficient of each eigenstate.

2.3.2 Adaptations for numerical representation of the 1D TIDE

To be able to represent an eigenvalue problem such as the one in eq. (2.31) numerically, some approximations must be made. Most of the steps taken will be left to section 3.2 and the subsections therein, but it is important to note some differences already at this point. First among these is the presence of the infinite sum in eq. (2.31). Infinite sums are impossible for computers to regard, and as such the

series will be truncated at some number M. Furthermore, as this is no longer an analytical problem (consider the approximation from (2.19)), the orthonormality condition no longer holds for the system. Therefore, it is useful to introduce notation for the inner products present in (2.31). The notation that will be used for the matrix elements of this eigenvalue problem in derivations of numerical methods are listed below.

$$\mathrm{S}_{k,n} \;\coloneqq\; \langle\psi_k|\psi_n\rangle \tag{2.35}$$

$$\mathrm{H}_{k,n} \;\coloneqq\; \big\langle\psi_k\big|H_{1D}^{TIDE}\big|\psi_n\big\rangle \tag{2.36}$$

The eigenvalue problem in eq. (2.34) will also have a slightly different form. As the inner product $\langle\psi_k|\psi_n\rangle$ in the LHS of eq. (2.31) does not vanish from the Kronecker delta, (2.34) is instead written as

$$\boldsymbol{h}\vec{c} = E\boldsymbol{s}\vec{c}, \tag{2.37}$$

where $\vec{c}$ is the eigenvector of coefficients for each eigenstate, and $\boldsymbol{h}$ and $\boldsymbol{s}$ are the $M \times M$ Hamiltonian matrix and overlap matrix, respectively. Written out on their matrix forms, $\boldsymbol{h}$ and $\boldsymbol{s}$ can be represented as

$$\boldsymbol{h} \;=\; \begin{pmatrix} \mathrm{H}_{1,1} & \mathrm{H}_{1,2} & \cdots & \mathrm{H}_{1,\mathrm{M}} \\ \mathrm{H}_{2,1} & \mathrm{H}_{2,2} & \dots & \mathrm{H}_{2,\mathrm{M}} \\ \vdots & \vdots & \ddots & \vdots \\ \mathrm{H}_{\mathrm{M},1} & \mathrm{H}_{\mathrm{M},2} & \dots & \mathrm{H}_{\mathrm{M,M}} \end{pmatrix}, \tag{2.38}$$

and

$$\boldsymbol{s} \;=\; \begin{pmatrix} \mathrm{S}_{1,1} & \mathrm{S}_{1,2} & \cdots & \mathrm{S}_{1,\mathrm{M}} \\ \mathrm{S}_{2,1} & \mathrm{S}_{2,2} & \dots & \mathrm{S}_{2,\mathrm{M}} \\ \vdots & \vdots & \ddots & \vdots \\ \mathrm{S}_{\mathrm{M},1} & \mathrm{S}_{\mathrm{M},2} & \dots & \mathrm{S}_{\mathrm{M,M}} \end{pmatrix} \tag{2.39}$$

Finally, for the integration contained in the inner products of (2.35) & (2.36), the domain of the wave function must be truncated to be numerically solvable. Whereas the interval of integration for analytic solutions is the entire real line $x \in (-\infty, \infty)$, it is shortened to $x \in (a, b)$ with $a < b$ for numerical solutions. With this truncation of the real line, the integral which is present in the overlap matrix element $\mathrm{S}_{k,n}$ (2.35) can be expressed numerically as

$$\mathrm{S}_{k,n} = \int_a^b \psi_k^\dagger(x)\psi_n(x)\,\mathrm{d}x \tag{2.40}$$

2.4 Introduction of the vector field

After solving the eigenvalue problem from eq. (2.32), the modeled system is set to evolve in time. This time-evolution is governed by the 1D TDDE (2.20), and uses solutions to the 1D TIDE (2.32) as its basis. Now, for The electric field of the photon beam is polarized in the x-direction, parallel to the direction of movement for the electron. Since the electron is locked on the x-axis, the positional dependency of its interaction with the electric field can be neglected.

The time evolution of the system is now influenced by the interaction between the electron and the electric field of the photon beam. This can be modeled by considering the Hamiltonian of interaction (H_I), expressed by reinstating the term $-A(t)$ to the momentum operator in the gauge transformation that was performed previously.

$$H_{1D}^{D,I} = H_{1D}^{D}(t) = -c\sigma_2 A(t) = -icA(t)\begin{pmatrix} 0 & -1 \\ 1 & 0 \end{pmatrix} \tag{2.41}$$

The time evolution is determined by incrementally propagating the 1D TDDE in time. The Hamiltonian governing this time-evolution is given by

$$H_{1D}^{TDDE} = H_{1D}^{TIDE} + H_{1D}^{D}(t), \tag{2.42}$$

with H_{1D}^{TIDE} defined as in (2.26). This yields a corresponding 1D TDDE on the form

$$i\frac{\partial \Psi(x,t)}{\partial t} = \left[H_{1D}^{TIDE} + H_{1D}^{D}(t)\right]\Psi(x,t) \tag{2.43}$$

Now, still keeping the total wave function as a product of separate time and space dependent functions, it can be written out as

$$\Psi(x,t) = \sum_{n=1}^{\infty} c_n(t)\,|\psi_n(x)\rangle \tag{2.44}$$

Inserting this into the 1D TDDE (2.43), it takes the form

$$\sum_{n=1}^{\infty} i\frac{\partial}{\partial t}[c_n(t)\,|\psi_n(x)\rangle] = \sum_{n=1}^{\infty} c_n(t)\left[H_{1D}^{TIDE} + H_{1D}^{D}(t)\right]|\psi_n(x)\rangle \tag{2.45}$$

Which, given the separation of time and space dependent functions, can be expressed as

$$\sum_{n=1}^{\infty} i\dot{c}_n(t)\,|\psi_n\rangle = \sum_{n=1}^{\infty} c_n(t)\left[H_{1D}^{TIDE} + H_{1D}^{D}(t)\right]|\psi_n\rangle \tag{2.46}$$

With the intent to formulate an eigenvalue problem, multiplying with $\langle\psi_k(x)|$ from the left gives

$$\langle\psi_k|\sum_{n=1}^{\infty} i\dot{c}_n(t)\,|\psi_n\rangle = \langle\psi_k|\sum_{n=1}^{\infty} c_n(t)\left[H_{1D}^{TIDE} + H_{1D}^{D}(t)\right]|\psi_n\rangle\,, \tag{2.47}$$

or, sorting the summations outside of the inner products,

$$\sum_{n=1}^{\infty} i\dot{c}_n(t)\underbrace{\langle\psi_k|\psi_n\rangle}_{=\delta_{k,n}} = \sum_{n=1}^{\infty} c_n(t)\left(\underbrace{\left\langle\psi_k\middle|H_{1D}^{TIDE}\middle|\psi_n\right\rangle}_{=E\delta_{k,n}} + \left\langle\psi_k\middle|H_{1D}^{D}(t)\middle|\psi_n\right\rangle\right) \tag{2.48}$$

Recognizing that the inner product $\left\langle\psi_k(x)\middle|H_{1D}^{TIDE}\middle|\psi_n(x)\right\rangle$ in the RHS of this equation can be substituted by (2.32), as well as applying the orthonormality condition to the LHS $[\sum_n i\dot{c}_n(t)\delta_{k,n} \to i\dot{c}_k(t)]$, the only term left to expand on is the time-dependent component of the RHS.

By substituting $H_{1D}^{D}(t) \to -icA(t)\begin{pmatrix} 0 & -1 \\ 1 & 0 \end{pmatrix}$ and $\psi_j(x) \to \begin{pmatrix} P_j(x) \\ Q_j(x) \end{pmatrix}$, $j = \{k, n\}$ into $\left\langle\psi_k(x)\middle|H_{1D}^{D}(t)\middle|\psi_n(x)\right\rangle$, the result is

$$\begin{aligned} \left\langle\psi_k(x)\middle|H_{1D}^{D}(t)\middle|\psi_n(x)\right\rangle &= -icA(t)\int_\Omega \left[\begin{pmatrix} P_k(x) \\ Q_k(x) \end{pmatrix}^\dagger \begin{pmatrix} 0 & -1 \\ 1 & 0 \end{pmatrix}\begin{pmatrix} P_n(x) \\ Q_n(x) \end{pmatrix}\right] dx \\ &= -icA(t)\int_\Omega \left[P_k^*(x)\cdot Q_n(x) - Q_k^*(x)\cdot P_n(x)\right] dx \end{aligned} \tag{2.49}$$

For ease of notation, the integral is annotated as $V_{k,n} = \int_\Omega \left[P_k^*(x)\cdot Q_n(x) - Q_k^*(x)\cdot P_n(x)\right] dx$. Thus, the 1D TDDE (2.48) can be simplified to

$$i\dot{c}_k(t) = \sum_{n=1}^{\infty} c_n(t)(E\delta_{k,n} - icA(t)V_{k,n}) \tag{2.50}$$

or, by multiplying both sides with $-i$,

$$\dot{c}_k(t) = \sum_{n=1}^{\infty} c_n(t)(-iE\delta_{n,k} - cA(t)V_{k,n}) \tag{2.51}$$

This equation will be taken as the grounds for time-evolution of the system. As it is impossible to regard infinite of this sort using computers, the rest of the derivation of the time-propagator is left to the chapter about numerical solutions.

2.5 1D TISE

Given the 1D TDSE (1.1) for a free particle

$$\frac{1}{2}\hat{\mathrm{p}}^2\Psi(x,t) = i\frac{\partial\Psi(x,t)}{\partial t}\,, \tag{2.52}$$

still with the same momentum operator $\hat{\mathrm{p}} = -i\frac{\partial}{\partial x}$ as in the Dirac equation (2.13). Separation of variables in Ψ can be performed by substituting

$$\Psi(x,t) \to T(t)\psi(x) = e^{-iEt}\psi(x)\,, \tag{2.53}$$

which allows for carrying out the derivative on the RHS of the equation.

$$i\frac{\partial}{\partial t}e^{-iEt}\psi(x) = E\Psi(x,t) \tag{2.54}$$

Again applying substitutions (2.6) & (2.5) from minimal coupling to the system,

$$\hat{\mathrm{p}} \quad \to \quad \hat{\mathrm{p}} - A(t) \tag{2.55}$$

$$E \quad \to \quad E - \phi(x)\,, \tag{2.56}$$

the Schrödinger equation can be rewritten as

$$\left[\frac{1}{2}(\hat{\mathrm{p}} - A(t))^2 + \phi(x)\right]\Psi(x,t) = E\Psi(x,t) \tag{2.57}$$

By setting $t = 0$, causing $A(t=0) = 0$ and $\Psi(x, t=0) = \psi(x)$, one gets the 1D TISE for an electron in a Coulomb potential.

$$\left[-\frac{1}{2}\frac{d^2}{dx^2} + \phi(x)\right]\psi(x) = E\psi(x) \tag{2.58}$$

The corresponding Hamiltonian becomes

$$H_{1D}^{TISE} = \left[-\frac{1}{2}\frac{d^2}{dx^2} + \phi(x)\right] \tag{2.59}$$

To explore this equation further, the total wave function $\psi(x)$ is expressed as a linear combination of its eigenstates,

$$\psi(x) = \sum_{n=1}^{\infty} c_n\psi_n(x)\,, \tag{2.60}$$

which by substitution makes eq. (2.58) take the form

$$\sum_{n=1}^{\infty} c_n\left[-\frac{1}{2}\frac{\mathrm{d}^2}{\mathrm{d}x^2} + \phi(x)\right]\psi_n(x) = E\sum_{n=1}^{\infty} c_n\psi_n(x) \tag{2.61}$$

Again introducing bracket notation, and then multiplying by an arbitrary eigenstate $\langle\psi_k(x)|$ from the left to find the inner products, one can transform eq. 2.61.

$$\left\langle \psi_k(x) \middle| \sum_{n=1}^{\infty} c_n \left[-\frac{1}{2}\frac{\mathrm{d}^2}{\mathrm{d}x^2} + \phi(x) \right] \middle| \psi_n(x) \right\rangle = \left\langle \psi_k(x) \middle| E \sum_{n=1}^{\infty} c_n \middle| \psi_n(x) \right\rangle \tag{2.62}$$

Moving the sum operator and constants out of the inner products yields

$$\sum_{n=1}^{\infty} c_n \left\langle \psi_k(x) \middle| \left[-\frac{1}{2}\frac{\mathrm{d}^2}{\mathrm{d}x^2} + \phi(x) \right] \middle| \psi_n(x) \right\rangle = E \sum_{n=1}^{\infty} c_n \left\langle \psi_k(x) | \psi_n(x) \right\rangle, \tag{2.63}$$

which when when exposed to the orthonormality condition $[\langle \psi_k(x)|\psi_n(x)\rangle \to \delta_{k,n},\ \sum_{n=1}^{\infty} c_n\delta_{k,n} \to c_n\delta_{k,n}]$ becomes

$$\begin{aligned} &\textstyle\sum_{n=1}^{\infty} c_n \left\langle \psi_k(x) \middle| \left[-\frac{1}{2}\frac{\mathrm{d}^2}{\mathrm{d}x^2} + \phi(x) \right] \middle| \psi_n(x) \right\rangle \\ &= \quad \textstyle\sum_{n=1}^{\infty} c_n \left\langle \psi_k(x) \middle| H_{1D}^{TISE} \middle| \psi_n(x) \right\rangle \quad = \quad E c_n \delta_{k,n} \end{aligned} \tag{2.64}$$

Rewriting the inner product on the LHS to integral form, the equation reads

$$\sum_{n=1}^{\infty} c_n \int_{\Omega} \psi_k^*(x) \left[-\frac{1}{2}\frac{\mathrm{d}^2}{\mathrm{d}x^2} + \phi(x) \right] \psi_n(x)\, dx = E c_n \delta_{k,n} \tag{2.65}$$

As the goal of this thesis is to find numerical solutions to the system, further work on transforming this equation into an eigenvalue problem is left for the corresponding chapter on numerical methods. Eq. (2.65) does, however, provide a useful relation when trying to solve the time-dependent system in sec. 2.6 & 3.5.

2.6 1D TDSE in a laser field

The time-evolution of the 1D model is governed by the 1D TDSE, formulated in eq. (2.57). It is helpful to reconstruct it into separate time and space dependent terms, starting with the minimal coupling momentum operator.

$$i\frac{\partial}{\partial t} |\Psi(x,t)\rangle = \left[\frac{1}{2}\left(-i\frac{\partial}{\partial x} - A(t) \right)^2 + \phi(x) \right] |\Psi(x,t)\rangle \tag{2.66}$$

The electric field from the photon beam is, due to the dipole approximation, assumed to be exclusively time-dependent. the total Hamiltonian for the 1D TDSE can be expressed as

$$
\begin{aligned}
H_{1D}^{TDSE} = & \; -\tfrac{1}{2}\tfrac{\partial^2}{\partial x^2} + iA(t)\tfrac{\partial}{\partial x} + \tfrac{1}{2}A(t)^2 + \phi(x) \\
= & \; \underbrace{-\frac{1}{2}\frac{\partial^2}{\partial x^2} + \phi(x)}_{=H_{1D}^{TISE}} + \underbrace{iA(t)\frac{\partial}{\partial x} + \frac{1}{2}A(t)^2}_{=H_I^{SE}} \\
& \Downarrow \\
H_{1D}^{TDSE} = & \; H_{1D}^{TISE} + H_I^{SE}
\end{aligned}
\tag{2.67}
$$

Explicitly, the Hamiltonian of interaction for the 1D Schrödinger model in a laser field (2.67) can be written as

$$
H_I^{SE} = iA(t)\frac{\partial}{\partial x} + \frac{1}{2}A(t)^2 \,. \tag{2.68}
$$

Still assuming that the total wave function $|\Psi(x,t)\rangle$ can be expressed as a linear combination of all eigenstates, the time-dependent component can inserted into the coefficient.

$$
|\Psi(x,t)\rangle = \sum_{n=1}^{\infty} c_n(t)\,|\psi_n(x)\rangle \tag{2.69}
$$

The 1D TDSE can now be rewritten as

$$
i\sum_{n=1}^{\infty} \underbrace{\frac{\partial}{\partial t}c_n(t)}_{=\dot{c}_n(t)}\,|\psi_n(x)\rangle = \sum_{n=1}^{\infty} c_n(t)\big[H_{1D}^{TISE} + H_I^{SE}\big]\,|\psi_n(x)\rangle \tag{2.70}
$$

By again finding the inner product with an arbitrary eigenstate $\langle\psi_k(x)|$ of the time-independent system from the left, the equation takes the form

$$
i\sum_{n=1}^{\infty} \dot{c}_n(t)\,\underbrace{\langle\psi_k(x)|\psi_n(x)\rangle}_{=\delta_{k,n}} = \sum_{n=1}^{\infty} c_n(t)\Big[\underbrace{\big\langle\psi_k(x)\big|H_{1D}^{TISE}\big|\psi_n(x)\big\rangle}_{=E\delta_{k,n}} + \underbrace{\big\langle\psi_k(x)\big|H_I^{SE}\big|\psi_n(x)\big\rangle}_{=V_{k,n}^{'}}\Big] \tag{2.71}
$$

This expression allows for some substitutions into the equation.

- From orthonormality, and again using the interaction between the Kronecker delta with a series, the LHS of this equation is simplified to LHS$\rightarrow \dot{c}_k(t)$.
- From the relation found in (2.64), the inner product with the H_{1D}^{TISE} operator can be replaced with $Ec_n(t)\delta_{k,n}$.
- Finally, for ease of notation, the last inner product of the equation above is substituted with $V_{k,n}^{'}$, given by

$$V_{k,n}^{'} = A(t) \int_{\Omega} \left[i\psi_k(x) \cdot \frac{\mathrm{d}\psi_n(x)}{\mathrm{d}x} + \frac{A(t)}{2} \cdot \psi_k(x) \cdot \psi_n(x) \right] \mathrm{d}x = \left\langle \psi_k(x) \middle| H_I^{SE} \middle| \psi_n(x) \right\rangle , \tag{2.72}$$

where H_I^{SE} is defined as in (2.68). The equation for the time-dependent system can now take the following form:

$$\dot{c}_k(t) = \sum_{n=1}^{\infty} c_n(t) \left[-iE_n \delta_{k,n} - iV_{k,n}^{'} \right] \tag{2.73}$$

The above eq. 2.73 will, in league with its corresponding Dirac counterpart 2.51, form the basis for time-evolution of the system in high-intensity laser potential. Further derivations and transformation into a matrix eigenvalue problem will be presented in a numerical framework, in chapter 3.

2.7 Radial solution to 3D TISE

For the sake of checking the validity of the script, it is reasonable to compare the results of a numeric solution to the analytic solution. Given how well-established the analytic solutions to the radial Schrödinger equation in 3D are, specifically in hydrogenic atoms, they pose as a practical tool for comparison.

The 3D TISE for an electron in a coulomb field is given by [9]

$$Eu(r) = \left[-\frac{1}{2} \frac{\mathrm{d}^2}{\mathrm{d}r^2} - \frac{z}{r} + \frac{l(l+1)}{2r^2} \right] u(r) , \tag{2.74}$$

with corresponding Hamiltonian

$$H_{3D}^{TISE} = \left[-\frac{1}{2} \frac{\mathrm{d}^2}{\mathrm{d}r^2} - \frac{z}{r} + \frac{l(l+1)}{2r^2} \right] . \tag{2.75}$$

In the same way as before, the radial wave function is written out as a sum of its eigenstates,

$$u(r) = \sum_{n=1} c_n u_n(r) , \tag{2.76}$$

and the inner product is found by multiplying with an arbitrary eigenstate $\langle u_k(r)|$ from the left.

$$\sum_{n=1} c_n E \left\langle u_k(r) | u_n(r) \right\rangle = \sum_{n=1} c_n \left\langle u_k(r) \middle| \left[-\frac{1}{2} \frac{\mathrm{d}^2}{\mathrm{d}r^2} - \frac{z}{r} + \frac{l(l+1)}{2r^2} \right] \middle| u_n(r) \right\rangle \tag{2.77}$$

Orthonormality is applied, and the resulting eigenvalue problem becomes

$$c_k E = \sum_{n=1} \int_0^{\infty} \left[-\frac{1}{2} u_k(r) \cdot \frac{\mathrm{d}^2 u_n(r)}{\mathrm{d}r^2} - u_k(r) \cdot \frac{z}{r} \cdot u_n(r) + u_k(r) \cdot \frac{l(l+1)}{2r^2} \cdot u_n(r) \right] \mathrm{d}r \tag{2.78}$$

2.8 The form of the vector potential

Before continuing to chapter 3 on numerical methods, the time-dependent vector potential $A(t)$ introduced in minimal coupling (2.5) should be discussed. As the subject of this thesis is to investigate the light-matter interaction between some model atom and a high-intensity laser pulse, the modeled vector potential $A(t)$ will be produced by the aforementioned laser. For the sake of simplicity, the field is assumed to be identical across the to-be-established models governed by both the 1D TDSE (2.66) and the 1D TDDE (2.51). To give results which are comparable to previous models [7, 27, 31], the form of the pulse is modeled as a sine wave contained in an "envelope" function. That is, assuming total spatial independence from the dipole approximation $\left(\frac{\mathrm{d}A}{\mathrm{d}x} \coloneqq 0\right)$,

$$A(t) = \frac{E_0}{\omega} \sin^2\left(\frac{\pi t}{T}\right) \sin(\omega t)\,, \tag{2.79}$$

with E_0 as the amplitude of the electric field strength, ω as the angular frequency of the field, and T as the total time of the pulse. The component $\sin^2\left(\frac{\pi t}{T}\right)$ will act as the envelope of the pulse, while $\sin(\omega t)$ governs the oscillations taking place within the envelope. The shape of the pulse will be presented in sec. 3.6 on numerical methods.

Chapter 3

Numerical methods

3.1 B-splines as a basis for representing wave functions

To accurately represent some as of yet unknown wave functions, which are not polynomials, as a linear combination of piece-wise polynomial basis functions, sounds counter-intuitive. However, with a finite basis set consisting of piece-wise polynomials which have been constructed in a specific way and which fulfill a set of conditions, representing them in this way has been shown to produce highly accurate results [1]. The choice of B-splines as a basis for representing the wave functions facilitates some computational advantages, such as being able to employ Gauss-Legendre integrals for inner products.

In this section, theory relating to the creation and applications of B-splines will be discussed.

3.1.1 Basic properties of B-splines

The foundation for understanding of B-splines in the present work, as well as the definitions and properties given in this section, are largely based on [16] (with light adjustments to notation).

B-splines are sets of piece-wise polynomials with specific intervals within which they have non-zero values. These intervals are defined by a knot sequence $\{T_i\}_{i=1}^{m}$ containing m elements of non-decreasing values, such that

$$T_1 \leq T_i \leq T_j \leq T_m \; \forall \; 1 \leq i \leq j \leq m$$

The knot sequence can be used to define B-splines of degree k if it has $m \geq k+2$ elements.

The individual B-spline $B_i^k(x)$ is a real polynomial of degree k that is non-negative everywhere. It also satisfies

$$B_i^k(x) > 0, \qquad x \in (T_i, T_{i+k+1}), \tag{3.1}$$

$$\sum_{i=1}^{m} B_i^k(x_1) = 1, \qquad x_1 \in (T_0, T_m), \tag{3.2}$$

Both of these attributes make B-splines suitable for the calculations at hand.

For the creation of B-splines, a common method is by using the Cox-de Boor recursion formula [3]. In [16]'s **Definition 2** (p. 4), this is expressed as

$$B_{j,}^{k}(x) \coloneqq \frac{x - T_j}{T_{j+k} - T_j} B_j^{k-1}(x) + \frac{T_{j+k+1} - x}{T_{j+k+1} - T_{j+1}} B_{j+1}^{k-1}(x)\,, \tag{3.3}$$

with the first B-spline being defined as

$$B_i^{k=0}(x) \coloneqq \begin{cases} 1\,, & \text{if } x \in [T_i, T_{i+1}) \\ 0\,, & \text{otherwise.} \end{cases} \tag{3.4}$$

In the current work, generation of B-splines is done by using the "BSpline" and "basis_element" functions included in the Python package "SciPy" [32]. This makes for quicker generation, and also makes extrapolation to higher resolutions much more efficient since each B-spline is stored as a callable object instead of as an array of numbers.

The knot sequence which will be used for the present work has knot vectors with the following properties:

$$T_1 = T_2 = \cdots = T_{k+1} = x_{min} \tag{3.5}$$

$$T_m = T_{m-1} = \cdots = T_{m-k-1} = x_{max} \tag{3.6}$$

$$T_i - T_{i-1} = \Delta t\,, \quad k+2 < i < m-k-1, \tag{3.7}$$

where Δt is a constant defined by the number of internal knots in the knot sequence. Particularly, the knot sequence will have its upper and lower bound padded with $k+1$ knots of equal value on each end, with the intent to avoid issues with the boundary conditions (this will be further discussed in section 3.1.3 during the test run of the 3D Schrödinger script). In particular, the padding of the original knot sequence T' can be expressed as follows:

$$T = T_{pad} = (\underbrace{x_{min}, x_{min}, \ldots, x_{min}}_{k+1 \text{ times}}, T', \underbrace{x_{max}, \ldots, x_{max}, x_{max}}_{k+1 \text{ times}}) \tag{3.8}$$

Below will be presented two illustrations of different-ordered B-spline basis function sets.

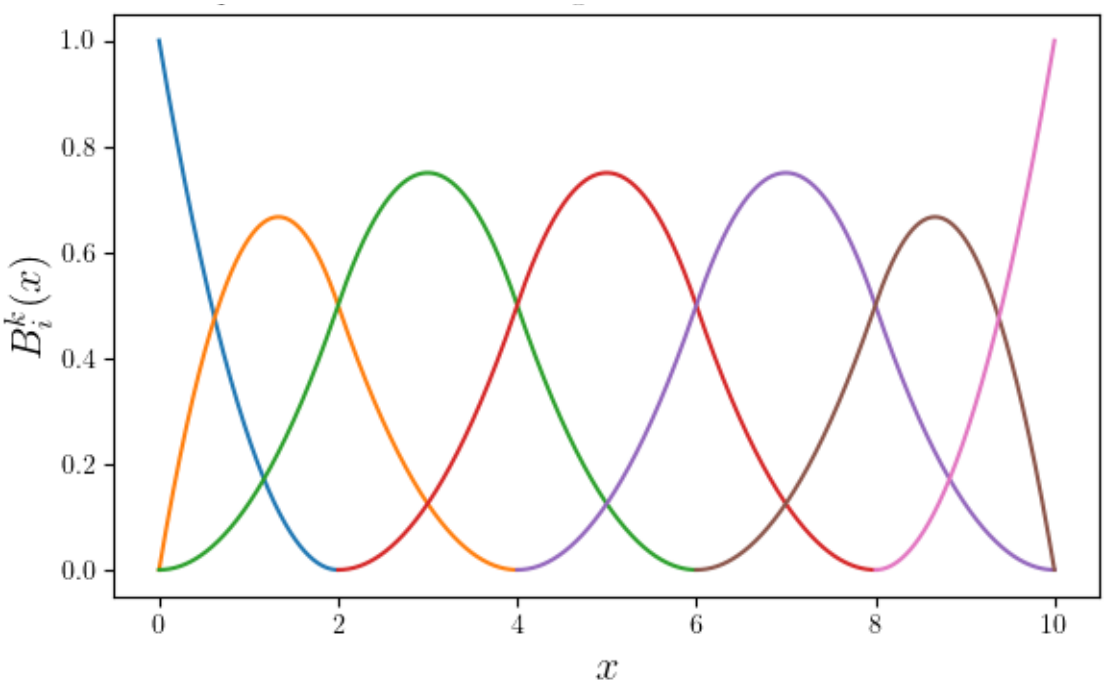

Figure 3.1a: B-spline basis functions of degree $k = 2$ with $m = 6$ internal knots.

Fig. 3.1a shows the general shape of the B-spline basis functions. Within the illustration, the internal knots of the knot sequence T can also be spotted, at $x = \{0, 2, 4, 6, 8, 10\}$. Noticeably, the two curves that descend from the upper right (Blue) and left (Pink) corners only give values in what seems like a single knot interval $[T_i, T_{i+1})$ each. This, however, is not the case due to the padding taking place at the ends of the knot sequence (3.8). As the initial 3.5 and final 3.6 $k+1$ values on the knot sequence of T have equal values of T_i, each B-spline basis function can still have non-zero values in the full interval $[T_i, T_{i+k+1})$ as it requires.

Now, to illustrate how the B-spline basis functions scale with increasing order k, Fig. 3.1b is given below.

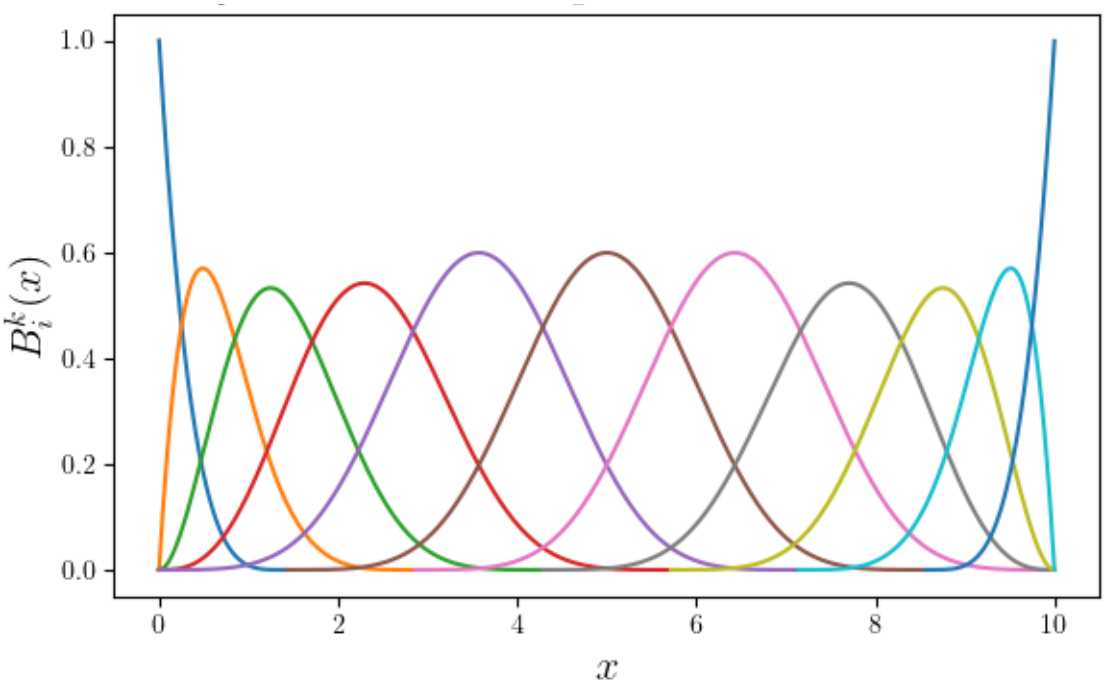

Figure 3.1b: B-spline basis functions of degree $k = 4$ with $m = 8$ internal knots.

Increasing the order k of the B-spline basis has a few effects on the basis functions, as well as on the knot sequence T. Most noticeably, it allows for sharper curvature within each basis function, while also increasing the number of intervals on the knot sequence T in which each B-spline basis function has non-zero values. From (3.1), an increase in k also increases the number of knots that allow non-zero values for the basis function.

Following this short introduction to B-splines, it is appropriate to proceed by introducing the Gauss-Legendre quadrature - a concept that furthers the suitableness of B-splines for use within numerical quantum mechanics.

3.1.2 Gauss-Legendre quadrature

Numerical methods for integration come in many shapes, but the one pertinent to the present paper is governed by the Gauss-Legendre quadrature, given by [2]

$$\int_{-1}^{1} f(x)\mathrm{d}x \simeq \sum_{i=1}^{n} \omega_i f(x_i)\,. \tag{3.9}$$

Here, $f(x)$ is some well-defined function, and ω_i are weights given by the roots of the n-th degree Legendre polynomial. The weights ω_i, which will be determined by using the SciPy [32] function "scipy.special.roots_legendre" in the following numerical calculations, will not be discussed in detail within the present work (though a comprehensive presentation can be found in [2, pp. 126-129]).

This quadrature provides exact values for integrals where $f(x) = P^k(x)$ are polynomials with degree $k \leq 2n-1$. As of right now, however, the integral is restricted to the interval $(-1, 1)$, though this is remediable through change of variable. For some $y \in \mathbb{Z}$ such that the knots $\{T_{y-1}, T_y\}$ of the knot sequence T (3.8) giving the x-interval $[T_{y-1}, T_y)$ with a non-zero length, and x_1, x_n as the first and last root of the n-th degree Legendre polynomial, the change of variable can be expressed as

$$u = \frac{(T_y - T_{y-1})(x+1)}{2(x_1 + x_n)} + T_{y-1}\,. \tag{3.10}$$

Adapting the Gauss-Legendre quadrature (3.9) to fulfill the needs for the calculations at hand is done in a few steps. Notably, the integrals that need to be computed (e.g. eqs. (2.65) & (2.33)) will be expressed as products of two polynomials of degree k. Using similar notation as what will be used for B-splines in later calculations, integrating over the product of two B-spline basis functions can be expressed as

$$\int_{T_y}^{T_{y+1}} B_i^k(x) \cdot B_j^k(x) \mathrm{d}x\,, \tag{3.11}$$

where y is an integer such that $B_i^k(x)$ and $B_j^k(x)$ both have non-zero values in the interval $[T_y, T_{y+1})$. Now, for some $k \in \mathbb{Z}^+$, the product between the B-splines can be expressed on the form

$$P^{2k}(x) \coloneqq B_i^k(x) \cdot B_j^k(x) \tag{3.12}$$

This means that the integral can be approximated exactly by the Gauss-Legendre quadrature if the value of n is chosen to be $n \geq k+1$. This also holds for integrals which contain ν-th derivatives of B-splines, as these are simply polynomials of degree $k - \nu$. To illustrate how this is done, Fig. 3.1c contains the same set of B-spline basis functions as Fig. 3.1b in high resolution (Black, solid curves), and in only finding their values in the integration points from the Legendre-polynomials (Red, dashed lines).

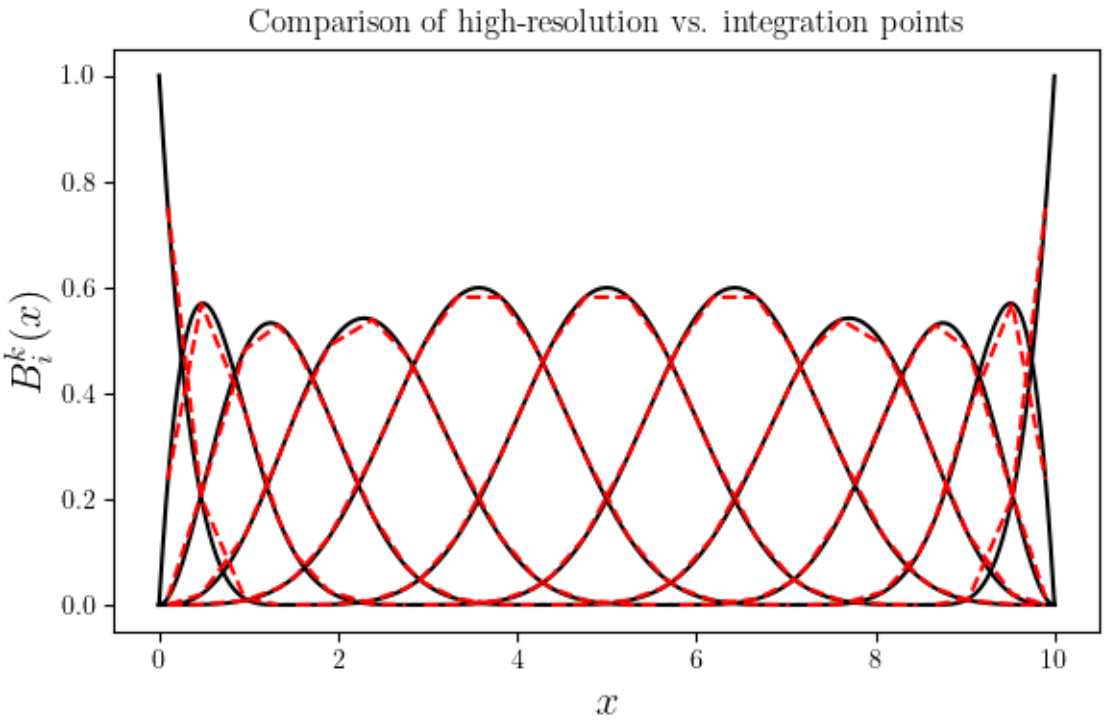

Figure 3.1c: Comparison of B-spline basis functions with degree $k = 4$ and $m = 8$ internal knots. Black, solid curves: 30001 discrete x-values. Red, dashed lines: Only values that correspond to roots of the Legendre polynomials of $n = k + 1 = 5$ are given.

From Fig. 3.1c, the discrepancy in resolution is apparent when comparing the black and red curves. With the Gauss-Legendre quadrature being able to exactly integrate the product of two k-th order polynomials with $n \geq k + 1$ discrete data points, only this amount of points is required. Because of the comparatively small amount of values needed, the computations become less intensive, and larger data sets can practically be solved.

Before proceeding to implementing the B-spline representation, it is important to consider the approximation that has been done in regard to the Coulomb potential (2.19). Since it contains the denominator $\sqrt{x^2 + \xi}$, with $\xi \in \mathbb{R}$, it does not have the shape of a polynomial, and is not exactly integrated by the Gauss-Legendre quadrature. Still, the Gauss-Legendre quadrature proves adept at approximating even this integral, which will be shown at a later point.

3.1.3 Preliminary tests for B-splines as basis functions for the 3D TISE

To consider the validity of using B-splines as basis functions within a quantum mechanical framework, a good comparison comes in the shape of the radial wave functions of the three-dimensional time-independent Schrödinger equation. This eigenvalue problem has well-defined analytical solutions for hydrogenic atoms, and a relatively simple form in comparison to the Dirac counterpart. Much of the derivations of these solutions will be left out, as they are all but repeated in section 3.4 about the 1D TISE solution. Starting from eq. (2.74) for some arbitrary eigenstate $u(r) = u_n(r)$,

$$E_n u_n(r) = \left[-\frac{1}{2}\frac{\mathrm{d}^2}{\mathrm{d}r^2} - \frac{z}{r} + \frac{l(l+1)}{2r^2} \right] u_n(r)\,. \tag{3.13}$$

Now, reintroducing bracket notation, multiplying by some arbitrary eigenstate $\langle u_k|$ from the left, and then taking the inner product, eq. (3.13) transforms.

$$E_n \langle u_k | u_n \rangle = \left\langle u_k \middle| H_{3D}^{TISE} \middle| u_n \right\rangle \tag{3.14}$$

It is assumed that any wave function which solves (3.13) can be approximated as a linear combination of B-spline basis functions [1].

$$u_n(x) \simeq \sum_{j=1}^{N} c_j B_j(x) \tag{3.15}$$

Note also the change of variables as $r \to x$. This is merely to keep consistent notation within the B-spline basis. In the radial equation 3.13, it is assumed that x is limited to the domain of $x > 0$. For the sake of being able to solve this numerically, the interval of integration is also restricted to some finite bound in $0 = a < x < b < \infty$. Since the coefficients are unknown at the present (and they are to be found by solving an eigenvalue problem), they are discarded. By combination with the B-spline representation 3.15 of the radial wave functions, eq. (3.14) can be transformed.

$$\begin{aligned} \sum_{i=1}^{N}\sum_{j=1}^{N} c_j E_n \int_a^b B_i(x) \cdot B_j(x)\mathrm{d}x \quad &= \quad \sum_{i=1}^{N}\sum_{j=1}^{N} c_j \int_a^b \left[-\frac{1}{2} B_i(x) \cdot \frac{\mathrm{d}^2 B_j(x)}{\mathrm{d}x^2} - \dots \right. \\ &\left. -B_i(x) \cdot \frac{z}{x} \cdot B_j(x) + B_i(x) \cdot \frac{l(l+1)}{2x^2} \cdot B_j(x) \right] \mathrm{d}x \end{aligned} \tag{3.16}$$

To shorten this expression, the integrals in eq. 3.16 are substituted for the matrix elements $\mathrm{H}_{i,j}$ for the Hamiltonian matrix (RHS) and the matrix elements $\mathrm{S}_{i,j}$ of the overlap matrix (LHS). The above equation can be rewritten as

$$E_n \sum_{i=1}^{N}\sum_{j=1}^{N} c_j \mathrm{S}_{i,j} = \sum_{i=1}^{N}\sum_{j=1}^{N} c_j \mathrm{H}_{i,j}\,, \tag{3.17}$$

or in the matrix form of the eigenvalue problem,

$$E_n \boldsymbol{s}\vec{c}_n = \boldsymbol{h}\vec{c}_n\,. \tag{3.18}$$

Solving eq. (3.18) will yield the eigenvalue E_n corresponding to energy level of the eigenstate $u_n(x)$. Furthermore, the eigenvector $\vec{c}_n$ will contain the coefficients required to represent the wave function $u_n(x)$ in the B-spline basis. To facilitate this, all matrix elements $\mathrm{H}_{i,j}$ and $\mathrm{S}_{i,j}$ are calculated using a self-created Python script, before being solved by an eigenvalue solver. The solver is contained in the package "SciPy", and the specific command being utilised is "scipy.linalg.decomp.eigh(H, S)" [32].

As the intent of computing these wave functions is to consider the validity of the B-spline representation of wave functions, running the script with $l = 0$ will suffice. The following parameters for the generation of the B-spline basis functions and Gauss-Legendre integration points are fed to the program:

- B-spline polynomial order: $k = 7$
- Interval for knot sequence: $a = 0 < T_i < 50 = b$
- Number of internal knots: $m = 200$

Furthermore, the proton number z is set to $z = 1$, so as to regard a modeled hydrogen atom. With this input, the first few wave function solutions to 3.18 are presented in the illustration below.

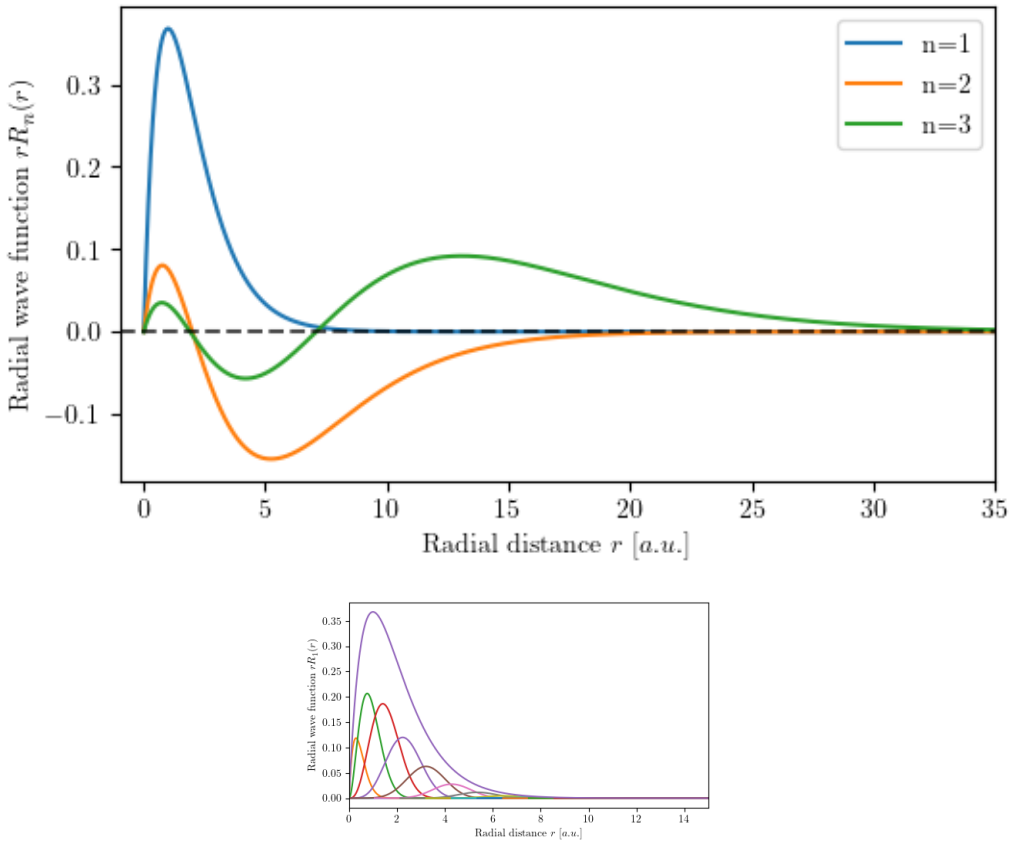

Figure 3.1d: Above – the three lowest–energy solutions to the radial 3D TISE (3.13), represented in a B-spline basis 3.15. Below – the ground state ($n = 1$) graph with illustrated B-spline basis functions.

The resulting wave functions from Fig. 3.1d have similar shapes to the $1s$, $2s$ and $3s$ wave functions. Still, to evaluate the validity of these results, it is necessary to see them in comparison to the analytic solution. This is done in Fig. 3.1e below.

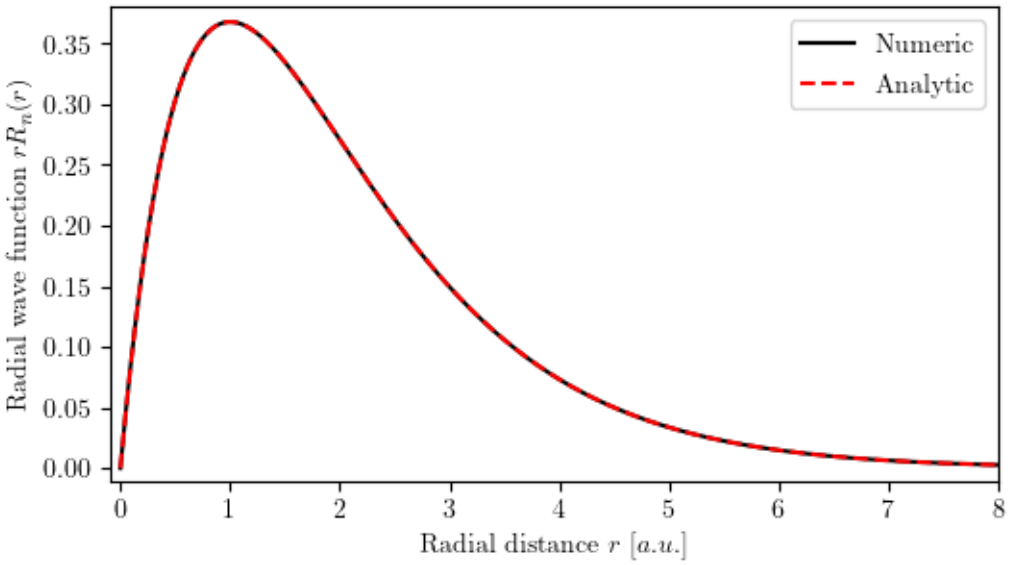

Figure 3.1e: Numeric solution (black, solid line) and analytical solution (red, dotted line) to the strongest-bound
solutions to the radial 3D TISE (3.13).

The ground state of the radial 3D TISE (3.13), as drawn in Fig. 3.1e above, has the exact solution [9],

$$u_{10}(r) = xe^{-x}\,, \qquad \text{in atomic units.} \tag{3.19}$$

The B-spline representation of the ground state radial wave function seems to be very spot on, with the largest single-point difference (from corresponding x-values, as in Fig. 3.1e) coming out to a total of $6.6 \cdot 10^{-11}$. This result bolster the credibility of the B-spline representation for the wave functions, but the energy levels are still yet to be considered. In solving the equation numerically, one has to discard the infinite number of bound states within the atom. Therefore, it is to be expected that energy levels corresponding to less tightly bound states will diverge. Energy levels corresponding to the numerical solution of eq. (3.13), as well as analytical energy solutions to the 3D TISE (with $E_n = -\frac{1}{2n^2}$ for hydrogen [9]), are presented in table 3.1.

State (n)	Numerical value	Analytic value	Absolute difference
1	-0.50000	-0.50000	$1.2 \cdot 10^{-14}$
2	-0.12500	-0.12500	$1.9 \cdot 10^{-14}$
3	-0.05556	-0.05556	$7.7 \cdot 10^{-9}$
4	-0.03120	-0.03125	$4.6 \cdot 10^{-5}$
5	-0.01786	-0.02000	$2.1 \cdot 10^{-3}$

Table 3.1: Numeric and analytic solutions for energy levels of the hydrogen atom

From table 3.1, it is apparent that something happens as the model moves to higher energy states. The immediate and obvious solution to this comes from looking at such wave functions near the upper boundary of the permitted values of x, as illustrated below.

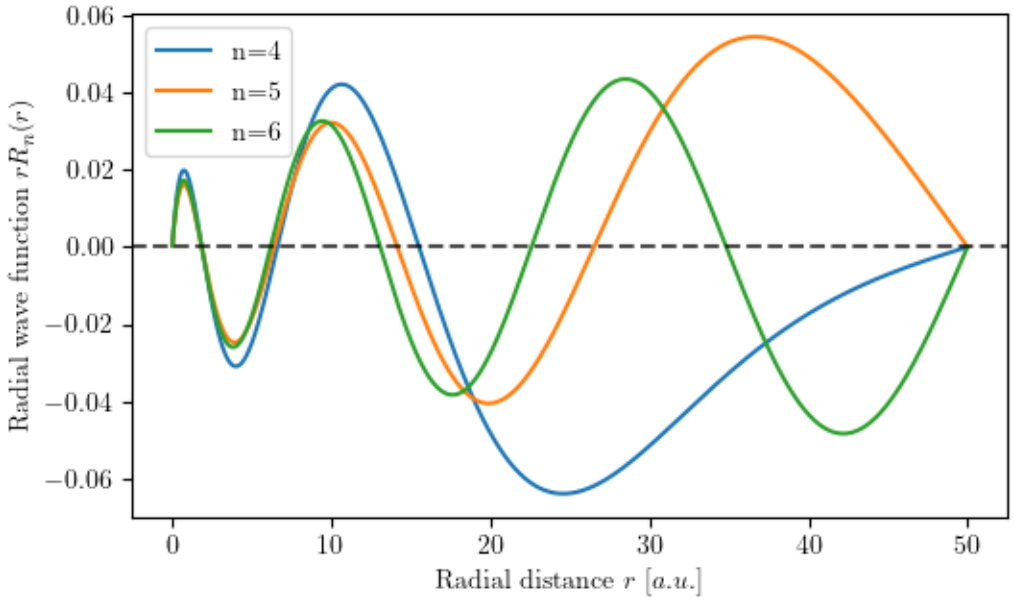

Figure 3.1f: Numerical solutions to eq. (3.13) in a B-spline basis, $n = \{4, 5, 6\}$

As expected, the numerical solutions are limited by the interval in which the electron is allowed to propagate. A possible explanation for why they are still relatively close to the correct answer (see table 3.1) comes in the form of the boundary conditions. From previous research [31, 27] and based on advice from the supervisor to the current thesis, this component has been a part of the script since the beginning. It proves to be a useful feature in dampening the boundary values of wave functions produced by this method, and its effect can be seen at the right edge of Fig. 3.1f.

Now, having somewhat thoroughly tested the validity of representing wave functions in a B-spline basis, as well as to have given my Python-script a test run, it is time to get on with something more squarely in the purview of this thesis - to solve the one-dimensional problem in such a way.

3.2 Approach to numerical solutions of the 1D TIDE in a central potential

Within this section, the methods and approximations used to obtain a numerical solution to the eigenvalue problem in eq. (2.31) are presented. For the sake of clarity, the 1D TIDE that will be the foundation for all calculations is given from eq. (2.30) is repeated:

$$\sum_{n=1}^{\infty} c_n E_n \left|\psi_n\right\rangle = \sum_{n=1}^{\infty} c_n H_{1D}^{TIDE} \left|\psi_n\right\rangle \tag{3.20}$$

Here, c_n and E_n is the coefficient and energy corresponding to the n-th eigenstate $|\psi_n\rangle$, H_{1D}^{TIDE} is the Hamiltonian

$$H_{1D}^{TIDE} \coloneqq \begin{pmatrix} c^2+\phi & -c\frac{d}{dx} \\ c\frac{d}{dx} & -c^2+\phi \end{pmatrix}, \tag{3.21}$$

as defined by (2.26), wherein ϕ is some soft-core approximation of the Coulomb potential, as found in (2.19)

$$\phi \equiv \phi(x) \coloneqq -\frac{z}{\sqrt{x^2+\xi}}\,, \qquad \xi \coloneqq \frac{2}{z^2} \tag{3.22}$$

To articulate the numerical adaptation of the eigenvalue problem in (2.31), it is helpful to apply the adaptations discussed in sec. 2.3.2. In the case of solutions in the Dirac frame, the dimensions of the matrices in the eigenvalue problem (2.37) are set as $2N$, to account for negative energy solutions. As such, the series in (2.31) is also truncated at this number, and can be rewritten as

$$\sum_{n=1}^{2N} c_n E_n \langle\psi_k|\psi_n\rangle = \sum_{n=1}^{2N} c_n \left\langle\psi_k\middle|H_{1D}^{Dirac}\middle|\psi_n\right\rangle\,, \tag{3.23}$$

or by using the matrix elements introduced in (2.35) and (2.36), as

$$\sum_{n=1}^{2N} c_n E_n \mathrm{S}_{k,n} = \sum_{n=1}^{2N} c_n \mathrm{H}_{k,n} \tag{3.24}$$

By inserting the matrix form of the 1D TIDE Hamiltonian from eq. (3.21), as well as by substituting ψ_k and ψ_n for the form introduced in (2.29b), eq. 3.23 can be rewritten on the form

$$\sum_{n=1}^{2N} c_n E_n \int_a^b \left[\begin{pmatrix} P_k(x) \\ Q_k(x) \end{pmatrix}^\dagger \begin{pmatrix} P_n(x) \\ Q_n(x) \end{pmatrix}\right] \mathrm{d}x = \sum_{j=1}^{2N} c_n \int_a^b \left[\begin{pmatrix} P_k(x) \\ Q_k(x) \end{pmatrix}^\dagger \begin{pmatrix} c^2+\phi & -c\frac{\mathrm{d}}{\mathrm{d}x} \\ c\frac{\mathrm{d}}{\mathrm{d}x} & -c^2+\phi \end{pmatrix} \begin{pmatrix} P_n(x) \\ Q_n(x) \end{pmatrix}\right] \mathrm{d}x \tag{3.25}$$

From the formulation of the eigenvalue problem (3.25), each matrix element of the Hamiltonian matrix $\boldsymbol{h}$ and the overlap matrix $\boldsymbol{s}$ (as defined in (2.38) and (2.39)) can be expressed as

$$\mathrm{H}_{k,n} = \int_a^b \left[\begin{pmatrix} P_k(x) \\ Q_k(x) \end{pmatrix}^\dagger \begin{pmatrix} c^2+\phi & -c\frac{\mathrm{d}}{\mathrm{d}x} \\ c\frac{\mathrm{d}}{\mathrm{d}x} & -c^2+\phi \end{pmatrix} \begin{pmatrix} P_n(x) \\ Q_n(x) \end{pmatrix}\right] \mathrm{d}x \tag{3.26}$$

$$\mathrm{S}_{k,n} = \int_a^b \left[\begin{pmatrix} P_k(x) \\ Q_k(x) \end{pmatrix}^\dagger \begin{pmatrix} P_n(x) \\ Q_n(x) \end{pmatrix}\right] \mathrm{d}x \tag{3.27}$$

From (3.26) and (3.27), the matrix and vector multiplication is carried out, yielding

$$\mathrm{H}_{k,n} = \int_a^b \left[P_k^*(x)\big(c^2+\phi\big)P_n(x) - cP_k^*(x)\frac{\mathrm{d}Q_n(x)}{\mathrm{d}x} + cQ_k^*(x)\frac{\mathrm{d}P_n(x)}{\mathrm{d}x} + Q_k^*(x)\big(-c^2+\phi\big)Q_n(x)\right]\mathrm{d}x\,, \tag{3.28}$$

and

$$\mathrm{S}_{k,n} = \int_a^b \left[P_k^*(x)\cdot P_n(x) + Q_k^*(x)\cdot Q_n(x)\right]\mathrm{d}x \tag{3.29}$$

The expressions (3.28) and (3.29) will be the starting point from which the large and small components of the eigenstates are represented in a B-spline basis.

3.2.1 B-spline representation of wave function eigenstates

Before proceeding to the next section, some remarks about the notation which will be used going forwards needs to be introduced. Specifically, notation related to the indices pertaining to the matrix elements of the eigenvalue problems. To signify matrix elements of the eigenvalue problem relating to the wave functions, the indices k, n are used. To avoid the confusion that can be caused by introducing another sum over indices to the mix, the indices i, j will be used to specify B-spline basis functions and matrix elements consisting of these. To further clarify:

- When presented with indices k, n, the Hamiltonian matrix element $\mathrm{H}_{k,n}$ (3.28) corresponds to the inner product of two eigenstates ψ_k, ψ_n surrounding the 1D TIDE Hamiltonian operator H_{1D}^{TIDE} (3.21).
- On the other hand, when written with indices i, j, the Hamiltonian matrix element $\mathrm{H}_{i,j}$ is to be understood as the inner product of two basis functions $B_i(x), B_j(x)$ surrounding the same (3.21) operator.

Additionally, it is useful to write a more general form for the integrals contained in the matrix elements of (3.28) and (3.29). Instead of using the large and small component of the wave spinor, they are to be represented as integrals over arbitrary two-component spinors. Additionally, as all B-spline basis functions are real polynomials, they are also self-adjoint. Using the notation which was introduced in the paragraph above this one, the substitution

$$\begin{pmatrix} P_k(x) \\ Q_k(x) \end{pmatrix} \longrightarrow \begin{pmatrix} f_i(x) \\ g_i(x) \end{pmatrix},$$

allows for rewriting the Hamiltonian matrix elements (3.28) as

$$\mathrm{H}_{i,j} = \int_a^b \left[f_i(x)\big(c^2+\phi\big)f_j(x) - cf_i(x)\frac{\mathrm{d}g_j(x)}{\mathrm{d}x} + cg_i(x)\frac{\mathrm{d}f_j(x)}{\mathrm{d}x} + g_i(x)\big(-c^2+\phi\big)g_j(x)\right]\mathrm{d}x\,, \tag{3.30}$$

while the overlap matrix elements (3.27) can be expressed as

$$\mathrm{S}_{i,j} = \int_a^b \left[f_i(x) \cdot f_j(x) + g_i(x) \cdot g_j(x) \right] \mathrm{d}x \tag{3.31}$$

Going forward, in the subsections 3.2.2-3.2.4 three different approaches to representing the wave functions of the Dirac equation will be described. Furthermore, each approach will be evaluated in terms of their qualities, before only one approach will be kept when moving into time-evolution in sec. 3.3.

3.2.2 First approach - exclusive large and small components

The first approach taken to represent the solutions to the 1D TIDE (3.23) in a B-spline basis, is by assuming that some eigenstate ψ_n can be written as separate sums of exclusive large and small components.

$$\psi_n = \begin{pmatrix} P_n(x) \\ Q_n(x) \end{pmatrix} = \sum_{i=1}^{N} c_{i,n} B_i^\kappa(x) \begin{pmatrix} 1 \\ 0 \end{pmatrix} + \sum_{i=N+1}^{2N} c_{i,n} B_{i-N}^\kappa(x) \begin{pmatrix} 0 \\ 1 \end{pmatrix}, \tag{3.32}$$

where κ is the order of the B-spline basis functions. For ease of notation, κ will be omitted from calculations until sec. 3.2.3. Proceeding to represent the wave functions on this (3.32) form, the matrix of the Hamiltonian matrix $\mathrm{H}_{i,j}$ (3.30) and the overlap matrix $\mathrm{S}_{i,j}$ (3.31) of eq. (3.24) may be expressed in the same way. To facilitate this split into upper and lower components, the $\boldsymbol{h}$ and $\boldsymbol{s}$-matrices are split into four block submatrices. This is done by the following partition:

$$\left[\begin{array}{c|c} \alpha & \beta \\ -- & -- \\ \gamma & \delta \end{array} \right] \tag{3.33}$$

Explicitly, the four submatrices have corresponding intervals of the indices i, j given as follows:

$\alpha:$	1	$\leq$	i	$\leq$	N	$\beta:$	1	$\leq$	i	$\leq$	N
	1	$\leq$	j	$\leq$	N		$N+1$	$\leq$	j	$\leq$	$2N$
$\gamma:$	$N+1$	$\leq$	i	$\leq$	$2N$	$\delta:$	$N+1$	$\leq$	i	$\leq$	$2N$
	1	$\leq$	j	$\leq$	N		$N+1$	$\leq$	j	$\leq$	$2N$

Table 3.2.2.1: Intervals for the values of i and j belonging to each submatrix

Inner products included in the matrix elements $\mathrm{H}_{i,j}$ (3.30) and $\mathrm{S}_{i,j}$ (3.31) can then be written out for each submatrix.

$$\textbf{Submatrix } \alpha: \begin{cases} 1 \leq i \leq N \\ 1 \leq j \leq N \end{cases} \quad \rightarrow \quad \begin{matrix} f_i = B_i(x) \\ g_i = 0 \end{matrix}, \quad \begin{matrix} f_j = B_j(x) \\ g_j = 0 \end{matrix}$$

For the overlap matrix,

$$\mathrm{S}_{i,j}^{[\alpha]} = \int_a^b B_i(x) \cdot B_j(x)\, dx \tag{3.34}$$

and for the Hamiltonian,

$$\mathrm{H}_{i,j}^{[\alpha]} = \int_a^b B_i(x)\big(c^2 + \phi\big)B_j(x)\, dx \tag{3.35}$$

$$= c^2 \underbrace{\int_a^b B_i(x) \cdot B_j(x)\, dx}_{=\mathrm{S}_{i,j}^{[\alpha]}} + \underbrace{\int_a^b B_i(x) \cdot \phi(x) \cdot B_j(x)\, dx}_{=\mathrm{V}_{i,j}^{[\alpha]}} \tag{3.36}$$

$$\mathrm{H}_{i,j}^{[\alpha]} = c^2\mathrm{S}_{i,j}^{[\alpha]} + \mathrm{V}_{i,j}^{[\alpha]}\,, \qquad \text{with} \qquad \mathrm{V}_{i,j}^{[\alpha]} \equiv \int_a^b B_i(x) \cdot \phi(x) \cdot B_j(x)\, dx \tag{3.37}$$

This process is repeated for each submatrix, and the results with some calculations are presented below. respective matrix elements:

$$\textbf{Submatrix } \beta : \left\{ \begin{array}{rcccl} N+1 & \leq & i & \leq & 2N \\ 1 & \leq & j & \leq & N \end{array} \right. \quad \rightarrow \quad \begin{array}{ll} f_i = 0 & f_j = B_j(x) \\ g_i = B_{i-N}(x) & g_j = 0 \end{array}$$

Overlap:

$$\mathrm{S}_{i,j}^{[\beta]} = 0 \tag{3.38}$$

Hamiltonian:

$$\mathrm{H}_{i,j}^{[\beta]} = c \underbrace{\int_a^b B_{i-N}(x) \cdot \frac{\mathrm{d}B_j(x)}{\mathrm{d}x}\, dx}_{=D_{i,j}^{[\beta]}} = c\mathrm{D}_{i,j}^{[\beta]} \tag{3.39}$$

$$\textbf{Submatrix } \gamma : \left\{ \begin{array}{rcccl} 1 & \leq & i & \leq & N \\ N+1 & \leq & j & \leq & 2N \end{array} \right. \quad \rightarrow \quad \begin{array}{ll} f_i = B_i(x) & f_j = 0 \\ g_i = 0 & g_j = B_{j-N}(x) \end{array}$$

Overlap:

$$\mathrm{S}_{i,j}^{[\gamma]} = 0 \tag{3.40}$$

Hamiltonian:

$$\mathrm{H}_{i,j}^{[\gamma]} = -c \underbrace{\int_a^b B_i(x) \cdot \frac{\mathrm{d}B_{j-N}(x)}{\mathrm{d}x}\, dx}_{=\mathrm{D}_{i,j}^{[\gamma]}} = -c\mathrm{D}_{i,j}^{[\gamma]} \tag{3.41}$$

$$\textbf{Submatrix } \delta : \begin{cases} N+1 \leq i \leq 2N \\ N+1 \leq j \leq 2N \end{cases} \rightarrow \begin{matrix} f_i = 0 \\ g_i = B_{i-N}(x) \end{matrix} , \begin{matrix} f_j = 0 \\ g_j = B_{j-N}(x) \end{matrix}$$

Overlap:

$$\mathrm{S}_{i,j}^{[\delta]} = \int_a^b B_{i-N}(x) \cdot B_{j-N}(x)\, dx \tag{3.42}$$

Hamiltonian:

$$\mathrm{H}_{i,j}^{[\delta]} = -c^2 \underbrace{\int_a^b B_{i-N}(x) \cdot B_{j-N}(x)\, dx}_{=\mathrm{S}_{i,j}^{[\delta]}} + \underbrace{\int_a^b B_{i-N}(x) \cdot \phi(x) \cdot B_{j-N}(x)\, dx}_{=\mathrm{V}_{i,j}^{[\delta]}} \tag{3.43}$$

$$\mathrm{H}_{i,j}^{[\delta]} = -c^2 \mathrm{S}_{i,j}^{[\delta]} + \mathrm{V}_{i,j}^{[\delta]} \qquad \text{with} \qquad \mathrm{V}_{i,j}^{[\delta]} = \int_a^b B_{i-N}(x) \cdot \phi(x) \cdot B_{j-N}(x)\, dx \tag{3.44}$$

By inserting the findings from eqs. (3.34), (3.37), (3.38), (3.39), (3.40), (3.41), (3.42) and (3.44) into the Hamiltonian matrix and the overlap matrix, each submatrix can be represented by the following block matrices:

$$\boldsymbol{h} = \begin{bmatrix} c^2\mathrm{S}_{i,j}^{[\alpha]} + \mathrm{V}_{i,j}^{[\alpha]} & | & c\mathrm{D}_{i,j}^{[\beta]} \\ - - - - - & + & - - - - - \\ -c\mathrm{D}_{i,j}^{[\gamma]} & | & -c^2\mathrm{S}_{i,j}^{[\delta]} + \mathrm{V}_{i,j}^{[\delta]} \end{bmatrix} \tag{3.45}$$

$$\boldsymbol{s} = \begin{bmatrix} \mathrm{S}_{i,j}^{[\alpha]} & | & 0 \\ - - - & + & - - - \\ 0 & | & \mathrm{S}_{i,j}^{[\delta]} \end{bmatrix} \tag{3.46}$$

By formulating the matrix elements in this way, the number of computations required to represent the matrices can be greatly reduced. Another reduction can be found in limiting the amount of matrix elements even considered for computation, by using an inherent attribute of the B-spline basis functions. Since any basis function $B_i(x)$ only has a limited interval $T_i \leq x \leq T_{i+k+1}$ in which it is non-zero (3.1), the inner product between two basis functions can only return a non-zero value if the intervals in which they have non-zero values overlap. That is,

$$\mathrm{H}_{i,j} \equiv 0 \equiv \mathrm{S}_{i,j} \quad \forall\, i,j \text{ such that } \quad \max(T_i, T_j) \geq \min(T_{i+k+1}, T_{j+k+1}) \tag{3.47}$$

With this, any matrix elements of $\boldsymbol{h}$ and $\boldsymbol{s}$ which do not fulfill the condition of $|i-j| \leq k+1$ must contain the value 0, and does not require calculation. This condition also applies to the diagonals of the submatrices β and γ, with mildly modified notation; Since one of the two indices i, j must be larger than N

Additionally, with these being Hermitian matrices with real elements, it can also be assumed that they are symmetrical. Therefore, only values on and above the diagonal need to be calculated. This can be formulated as

$$\mathrm{H}_{i,j} \equiv 0 \quad \forall\, i, j \;\Rightarrow 0 \leq i - j \leq k + 1 \tag{3.48}$$

This, in effect, means that all non-zero elements of the $\boldsymbol{h}$ and $\boldsymbol{s}$ matrices will be located on or near the diagonal of each submatrix. In the case of the $\boldsymbol{s}$ matrix, only the α and δ submatrices will have non-zero elements.

By taking the approach described in this section, the script is able to come up with solutions to the 1D TIDE (3.23). To inspect their accuracy, some illustrations and solutions for the energy are given below.

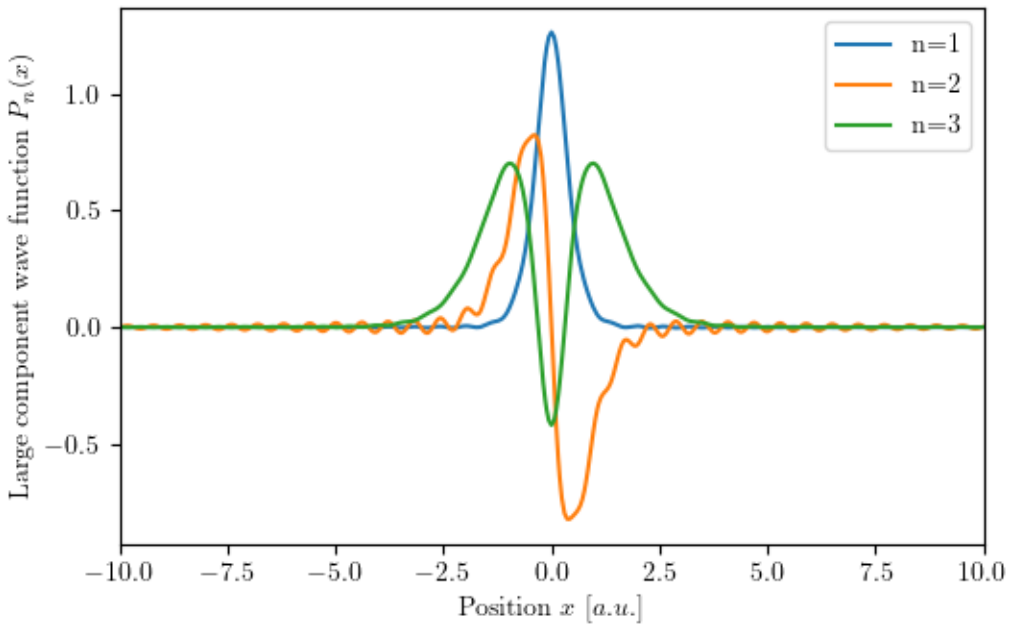

Figure 3.2a: Large component of the first few positive energy solutions of the 1D TIDE(3.20) in B-spline basis (3.32). $k = 7$, $(a, b) = (-30, 30)$, $n_{internal\,knots} = 200$, $Z = 5$

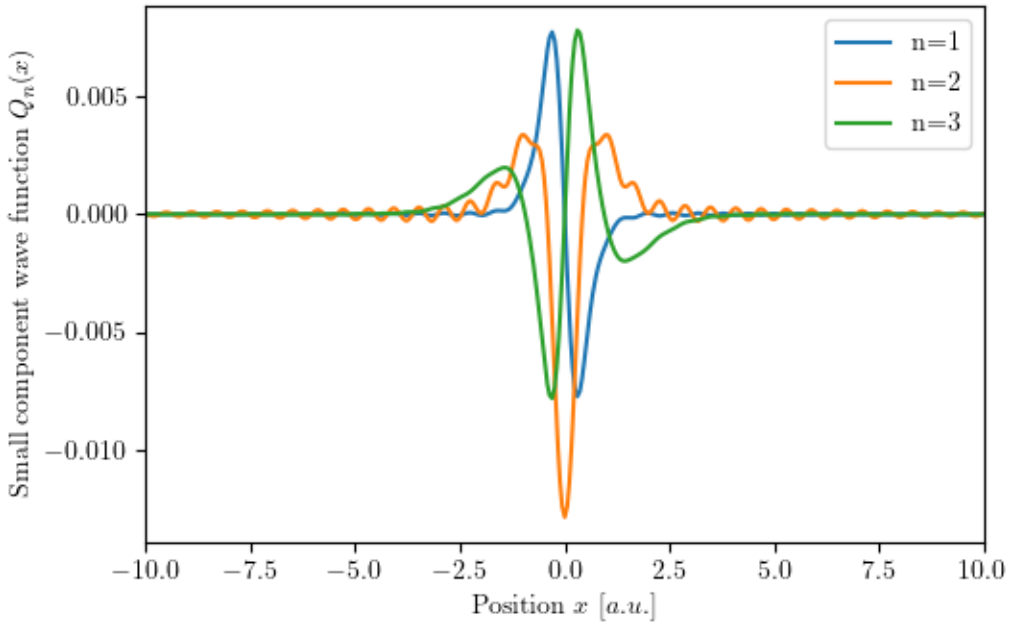

Figure 3.2b: Small component of the first few positive energy solutions of the 1D TIDE (3.20) in B-spline basis (3.32). $k = 7$, $(a, b) = (-30, 30)$, $n_{internal\,knots} = 200$, $Z = 5$

Looking at Figs. 3.2a & b above, something is clearly wrong in this representation. The waviness that is present within all of them, though which is especially prevalent in the $n = 2$ state, is likely due to some misrepresentation of the wave function of the wave functions. In addition to looking at the wave functions, it is helpful to inspect the energy levels corresponding to each state. The analytical energy values below are given from a 3D model[22] from the expression

$$\epsilon = \frac{1}{\sqrt{1 + \frac{Z^2\alpha^2}{\left(n+\sqrt{(j+1/2)^2 - Z^2\alpha^2}\right)^2}}}, \qquad \text{with } j = 0 \text{ corresponding to 1D.} \tag{3.49}$$

State n	Numerical energy 1D $[a.u.]$	Analytical energy 3D $[a.u.]$	Absolute difference
1	$E_1^{e.o.} = -12.49275$	-12.52086	0.02811
2	$E_2^{e.o.} = -5.85523$	-3.12839	2.72386
3	$E_3^{e.o.} = -3.34361$	-1.38997	1.95364
4	$E_4^{e.o.} = -2.36280$	-0.78172	1.58108

Table 3.2.2.1: Energy levels of numerical [$k = 7$, $(a, b) = (-30, 30)$, $n_{internal\,knots} = 200$, $Z = 5$, 1D TIDE (3.20), equal-order B-spline rep. (3.32)] and analytical [(2.11), values from (3.49)] solutions of the first few positive energy states.

As expected, the energy levels for non-ground state energies have a much larger difference from the analytical energy than the ground state does. In table 3.2.2.1 there is, however, another interesting point of data: The ground state energy of the model hydrogenic Boron ($Z = 5$) is less tightly bound in

the numerical Dirac than what you would expect from the Schrödinger frame ($E_{g.s} = -\frac{Z^2}{2n^2} \to -12.5$ [21]). In sec. 3.3, this will be further investigated when results from a 1D TISE model are presented.

Continuing with the investigation into what might have set the model off-balance, it is useful to look at the wave functions for some negative energy states.

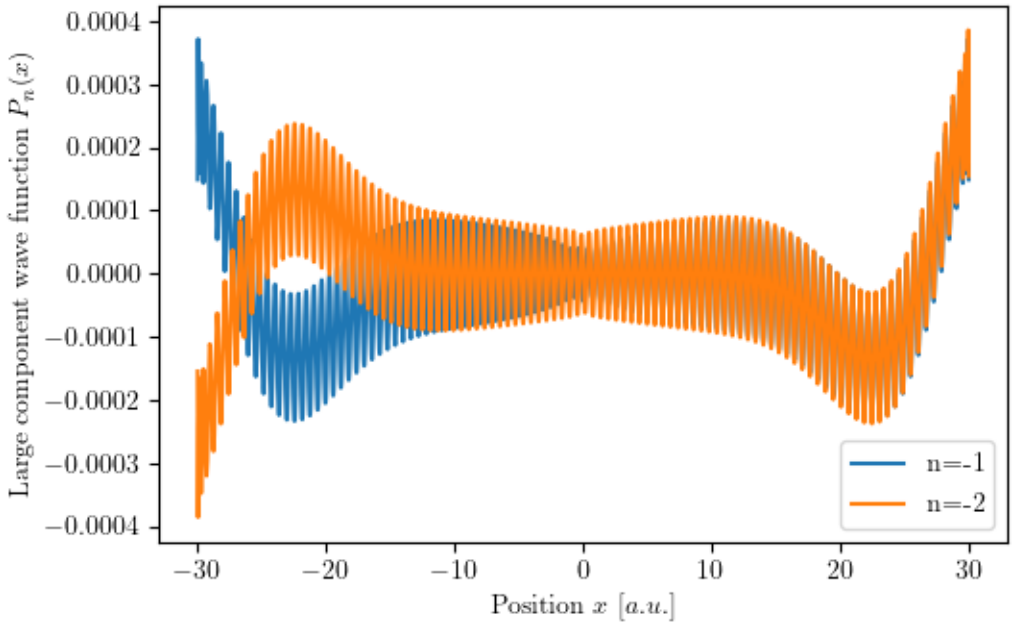

Figure 3.2c: Large component of the first two negative energy solutions to the 1D TIDE (3.20) in B-spline basis (3.32). $k = 7$, $(a, b) = (-30, 30)$, $n_{internal\,knots} = 200$, $Z = 5$

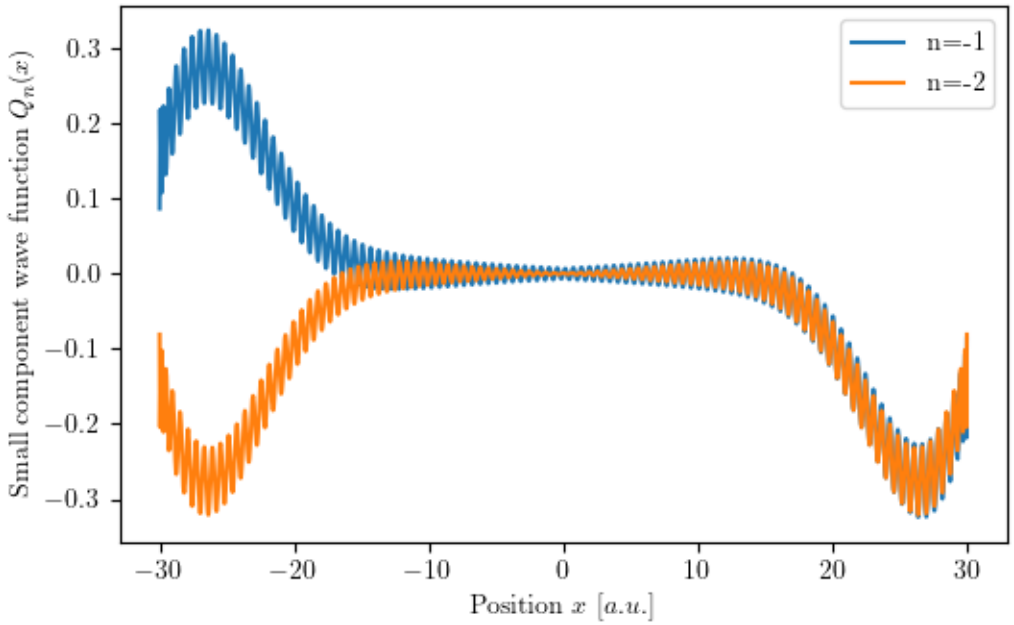

Figure 3.2d: Small component of the first two negative energy solutions to the 1D TIDE (3.20) in B-spline basis (3.32). $k = 7$, $(a, b) = (-30, 30)$, $n_{internal\,knots} = 200$, $Z = 5$

Looking at Figs. 3.2c & d, it is more apparent than ever that something is going wrong with the representation given by (3.32), at the start of this subsection. Now, by inspecting the solutions for the energy of the first 4 negative energy states (presented in Table 3.2.2.2), another pattern emerges.

Energy state n	Energy $[a.u.]$
-1	-0.2221
-2	-0.2232
-3	-0.2882
-4	-0.2898

Table 3.2.2.2: Numerical solutions of the 1D TIDE (3.20) in B-spline basis (3.32) for the energy of the first four negative energy states. $k = 7$, $(a, b) = (-30, 30)$, $n_{internal\,knots} = 200$, $Z = 5$

From table 3.2.2.2, it might seem as if the energy solutions are paired up with one another. Previous studies have discovered similar results (see e.g. [25] and references therein), and the phenomenon is called spurious states. Graphing the density of negative energy states,

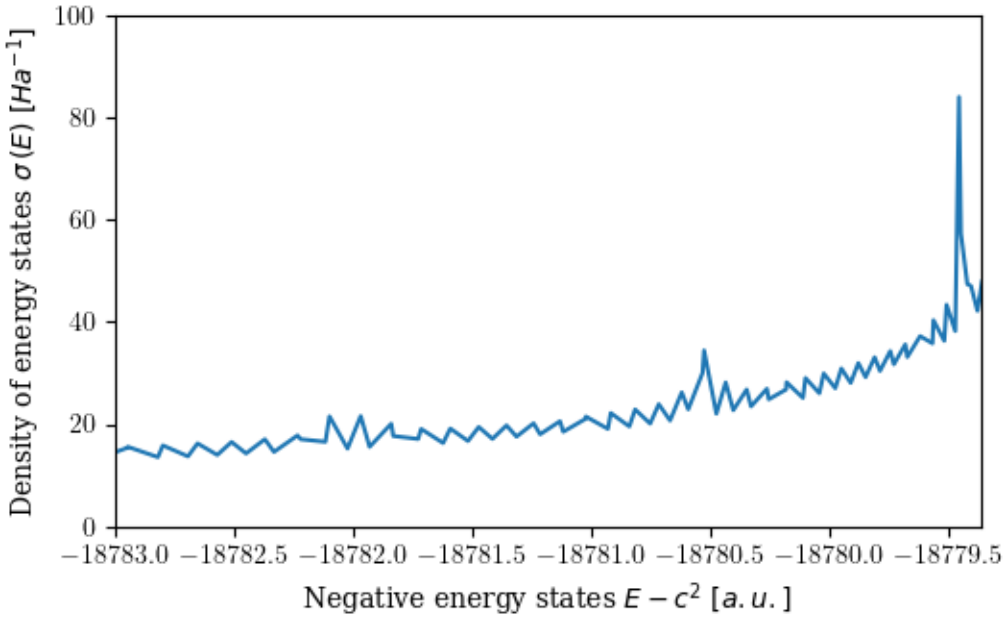

Fig. 3.2-1: Density of negative energy solutions to the 1D TIDE (3.20) in B-spline basis (3.32) $k = 7$, $(a, b) = (-30, 30)$, $n_{internal\,knots} = 200$, $Z = 5$, $\sigma(E) = \frac{2}{E_{i+1} - E_{i-1}}$.

It has become apparent that this method (3.32) for representing solutions to the 1D TIDE (3.20) is unsatisfactory. Rather immediately discarding this method, however, the professor supervising the current thesis proposed an adjustment to the representation, by including different-order B-spline basis functions for the large and small components of the wave functions. This approach will be discussed in the next subsection.

3.2.3 Second approach - Different ordered B-splines for large and small component

The adjustment which will be applied to the B-spline representation (3.32) from last subsection is relatively simple. The order of the B-splines used to represent the small component of solutions to the 1D TIDE (3.20) is increased by one. Specifically, this different-order B-spline representation can be written as

$$\psi_k = \begin{pmatrix} P_n(x) \\ Q_n(x) \end{pmatrix} = \sum_{i=1}^{N} c_{i,n} B_i^{\kappa}(x) \begin{pmatrix} 1 \\ 0 \end{pmatrix} + \sum_{i=N+1}^{2N+1} c_{i,n} B_{i-N}^{\kappa+1}(x) \begin{pmatrix} 0 \\ 1 \end{pmatrix}. \tag{3.50}$$

Very few significant changes are introduced by applying this adjustment, and most calculations pertaining to the solutions of the 1D TIDE (3.20) are done near identically to the process which was described in sec. 3.2.2. The main differences come in the form of now having to generate two separate B-splines, as well as by altering the formulation of (3.47). Regarding the latter of these differences, as a direct result of (3.1), each B-spline basis function can have non-zero values in a higher amount of

intervals $[T_i, T_{i+1})$ laid out by the knot sequence T. This can be accounted for by simply calculating the values in matrix elements one position further from the diagonal in each submatrix of $\boldsymbol{h}$ (3.45) and $\boldsymbol{s}$ (3.46), compared to (3.47). By adjusting the Python-script in the way that is being put forth in the current paragraph, in combination with the different-order B-spline representation, the following results are found.

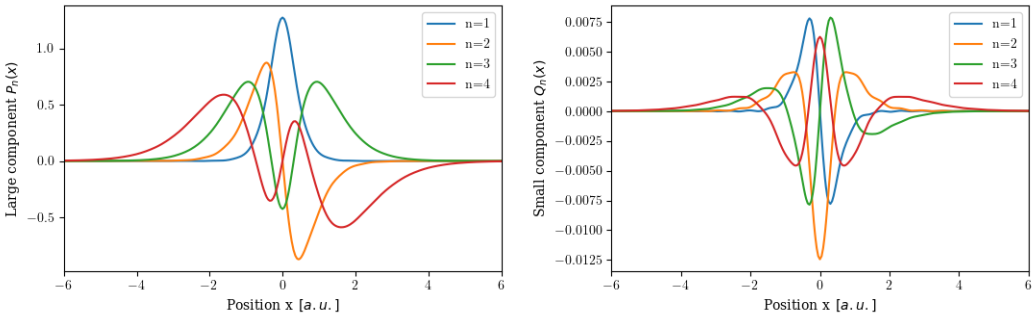

Figure 3.2e: Large (left image) and small (right image) components of the first four positive energy solutions to the 1D TIDE (3.20) in different-order B-spline basis (3.50).

$$k = \begin{cases} 7, & P_n(x) \text{ [left image]} \\ 8, & Q_n(x) \text{ [right image]} \end{cases}, \; (a,b) = (-30,30), \; n_{internal\,knots} = 200, \; Z = 5$$

From Fig. 3.2e, there is obvious improvement when seen in comparison to Figs. 3.2a & b. The curves are much smoother and significantly less jittery. Still, through closer investigation of the wave function for the small component, they are not fully satisfactory. This error is further illustrated by viewing the corresponding graphs for the negative energy values, given in Figs. 3.2f & g.

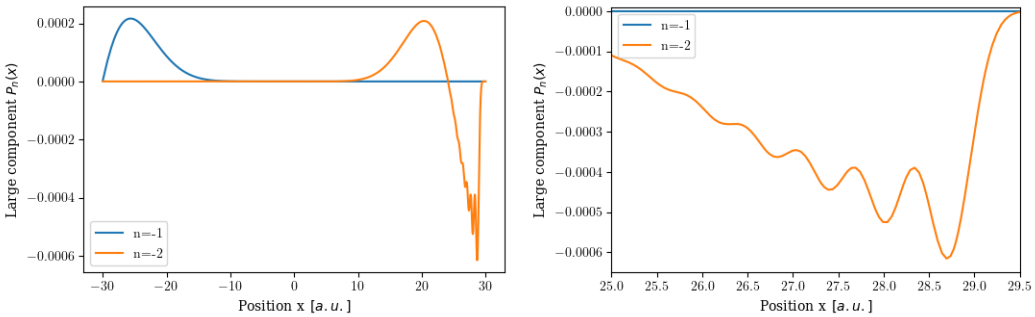

Figure 3.2f: Large component of the first two negative energy solutions to the 1D TIDE (3.20) in different-order B-spline representation (3.50).
[The right-side image is an up-scaled version of the left-side one.]

$$k = \begin{cases} 7, & P_n(x) \text{ [illustrated]} \\ 8, & Q_n(x) \text{ [not pictured]} \end{cases}, \; (a,b) = (-30,30), \; n_{internal\,knots} = 200, \; Z = 5$$

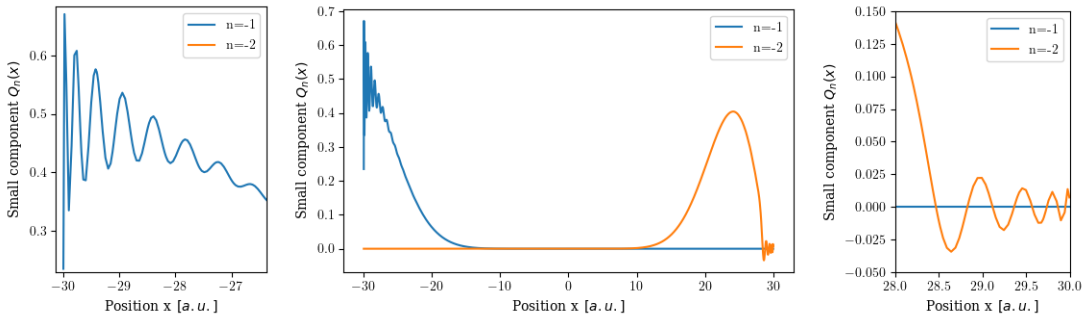

Figure 3.2g: Small component of the first two negative energy solutions to the 1D TIDE (3.20) in different-order B-spline representation (3.50).
[The left and right images are up-scaled versions of the center image.]

$$k = \begin{cases} 7, & P_n(x) \text{ [not pictured]} \\ 8, & Q_n(x) \text{ [illustrated]} \end{cases}, \ (a,b) = (-30,30), \ n_{internal\,knots} = 200, \ Z = 5$$

The two figures 3.2f&g clearly show the jittering that was observable in Figs. 3.2a-e, though in a much more dampened intensity. Still, to be certain that discarding this representation is a good decision, the energy solutions should also be considered. Graphing the density of states, as was done in Fig. 3.2-1, now for the different-order B-spline representation:

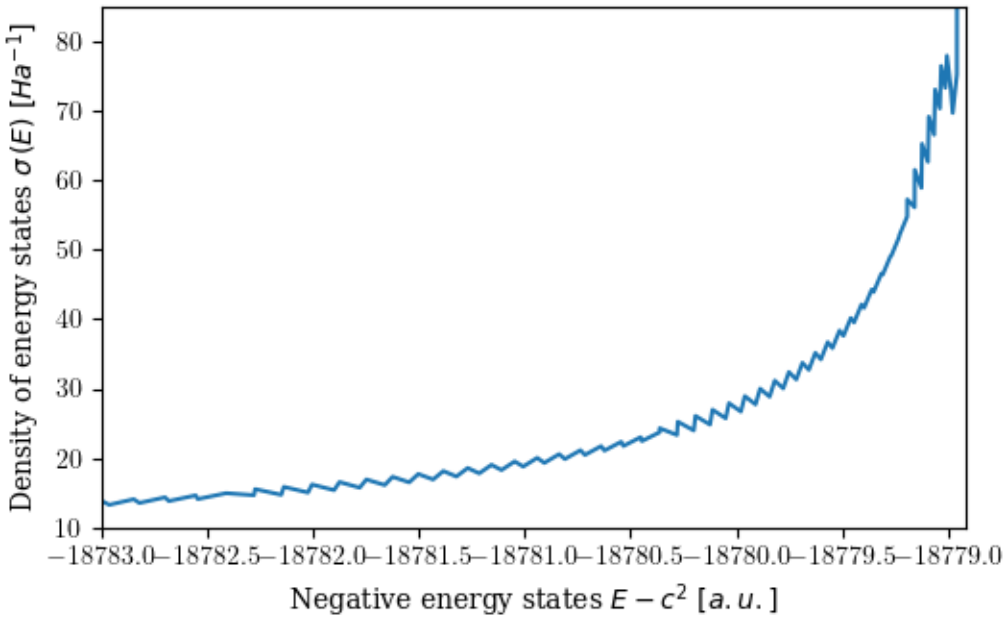

Figure 3.2-2: Density of negative energy solutions to the 1D TIDE (3.20) in different-order B-spline representation (3.50).

$$k = \begin{cases} 8 \\ 7 \end{cases}, \ (a,b) = (-30,30), \ n_{internal\,knots} = 200, \ Z = 5$$

The lowest positive energy solution $E_1^{d.o.}$ to the 1D TIDE (3.20) in different-order B-spline repre-

sentation (3.50) comes out to $E_1^{d.o.} = -12.49846\,a.u.$, with $k = \begin{cases} 7, & P_n(x)\,[\text{not pictured}] \\ 8, & Q_n(x)\,[\text{illustrated}] \end{cases}$, $(a,b) = (-30,30)$, $n_{internal\,knots} = 200$ and $Z = 5$. When compared to the solution for the ground state energy $E_1^{e.o.}$ in equal-order B-spline representation (3.32), given in table 3.2.2.1 as $E_1^{e.o.} = -12.49275\,a.u.$, it can be seen that the change of representation has yielded results which are in closer agreement with the 3D analytical value, found from (3.49). Still, the prevalence of spurious states arising from both approaches indicate that another approach is in order.

3.2.4 Third approach - Dual Kinetic Balance

By discarding both previous attempts [formulated in (3.32) and (3.50)] at representing the solutions to the 1D TIDE (3.20), it is time for a third approach. Inspired by the methods found in [25], and by the encouragement of my supervisor, this next approach makes use of something called *Dual Kinetic Balance*. This approach redefines the basis in which the wave functions are to be represented in the following way [25]:

$$|\psi_n\rangle_{DKB} = \begin{pmatrix} P_n \\ Q_n \end{pmatrix} = \sum_{i=1}^{N} c_i \begin{pmatrix} B_i(x) \\ \frac{1}{2c}\frac{\mathrm{d}B_i(x)}{\mathrm{d}x} \end{pmatrix} + \sum_{i=N+1}^{2N} c_i \begin{pmatrix} \frac{1}{2c}\frac{\mathrm{d}B_{i-N}(x)}{\mathrm{d}x} \\ B_{i-N}(x) \end{pmatrix} \tag{3.51}$$

Each matrix element of the eigenvalue matrices is still some integral over the corresponding basis function, with the following representation:

$$\begin{pmatrix} f_i \\ g_i \end{pmatrix} = \begin{cases} \begin{pmatrix} B_i(x) \\ \frac{1}{2c}\frac{\mathrm{d}B_i(x)}{\mathrm{d}x} \end{pmatrix} & 1 \leq i \leq N \\ \begin{pmatrix} \frac{1}{2c}\frac{\mathrm{d}B_{i-N}(x)}{\mathrm{d}x} \\ B_{i-N}(x) \end{pmatrix} & N+1 \leq i \leq 2N \end{cases}, \tag{3.52}$$

From here, (3.52) can be inserted into the expression for the matrix elements described in (3.30) & (3.31),

$$\mathrm{H}_{i,j} = \int_\Omega \left[f_i\big(c^2 + \phi\big) f_j - c f_i \frac{\mathrm{d}g_j}{\mathrm{d}x} + c g_i \frac{\mathrm{d}f_j}{\mathrm{d}x} + g_i\big(-c^2 + \phi\big) g_j \right] dx \tag{3.53}$$

and

$$\mathrm{S}_{i,j} = \int_\Omega \left[f_i \cdot f_j + g_i \cdot g_j \right] dx\,. \tag{3.54}$$

Repeating the derivations from subsection 3.2.2 in this new representation yields the following terms for the calculation of each submatrix:

$$\textbf{Submatrix } \alpha : \begin{cases} 1 \leq i \leq N \\ 1 \leq j \leq N \end{cases} \implies \begin{array}{l} \begin{pmatrix} f_i \\ g_i \end{pmatrix} = \begin{pmatrix} B_i(x) \\ \frac{1}{2c}\frac{\mathrm{d}B_i(x)}{\mathrm{d}x} \end{pmatrix} \\ \\ \begin{pmatrix} f_j \\ g_j \end{pmatrix} = \begin{pmatrix} B_j(x) \\ \frac{1}{2c}\frac{\mathrm{d}B_j(x)}{\mathrm{d}x} \end{pmatrix} \end{array}$$

Overlap matrix:

$$\begin{aligned} \mathrm{S}_{i,j}^{[\alpha]} &= \int_a^b \left[B_i(x) \cdot B_j(x) + \tfrac{1}{2c}\tfrac{\mathrm{d}B_i(x)}{\mathrm{d}x} \cdot \tfrac{1}{2c}\tfrac{\mathrm{d}B_j(x)}{\mathrm{d}x} \right] dx \\ &= \int_a^b \left[B_i(x) \cdot B_j(x) + \tfrac{1}{4c^2}\tfrac{\mathrm{d}B_i(x)}{\mathrm{d}x} \cdot \tfrac{\mathrm{d}B_j(x)}{\mathrm{d}x} \right] dx \end{aligned} \tag{3.55}$$

Hamiltonian matrix:

$$\begin{aligned} \mathrm{H}_{i,j}^{[\alpha]} &= \int_a^b \Big[B_i(x)\big(c^2 + \phi(x)\big) B_j(x) - cB_i(x) \cdot \tfrac{1}{2c}\tfrac{\mathrm{d}^2 B_j(x)}{\mathrm{d}x^2} + \\ &\quad + \tfrac{c}{2c}\tfrac{\mathrm{d}B_i(x)}{\mathrm{d}x} \cdot \tfrac{\mathrm{d}B_j(x)}{\mathrm{d}x} + \tfrac{1}{2c}\tfrac{\mathrm{d}B_i(x)}{\mathrm{d}x}\big(-c^2 + \phi(x)\big)\tfrac{1}{2c}\tfrac{\mathrm{d}B_j(x)}{\mathrm{d}x} \Big] \, dx \end{aligned} \tag{3.56}$$

$$\begin{aligned} \mathrm{H}_{i,j}^{[\alpha]} &= \int_a^b \Big[\big(c^2 + \phi(x)\big) \cdot \Big(B_i(x) \cdot B_j(x) + \tfrac{1}{4c^2}\tfrac{\mathrm{d}B_i(x)}{\mathrm{d}x} \cdot \tfrac{\mathrm{d}B_j(x)}{\mathrm{d}x} \Big) - \\ &\quad - \tfrac{1}{2} B_i(x) \cdot \tfrac{\mathrm{d}^2 B_j(x)}{\mathrm{d}x^2} \Big] \, dx \end{aligned} \tag{3.57}$$

$$\textbf{Submatrix } \beta : \begin{cases} N+1 \leq i \leq 2N \\ 1 \leq j \leq N \end{cases} \implies \begin{array}{rcl} \begin{pmatrix} f_i \\ g_i \end{pmatrix} &=& \begin{pmatrix} \frac{1}{2c}\frac{\mathrm{d}B_{i-N}(x)}{\mathrm{d}x} \\ B_{i-N}(x) \end{pmatrix} \\ \\ \begin{pmatrix} f_j \\ g_j \end{pmatrix} &=& \begin{pmatrix} B_j(x) \\ \frac{1}{2c}\frac{\mathrm{d}B_j(x)}{\mathrm{d}x} \end{pmatrix} \end{array}$$

Overlap matrix:

$$\begin{aligned} \mathrm{S}_{i,j}^{[\beta]} &= \int_a^b \left[\tfrac{1}{2c}\tfrac{\mathrm{d}B_{i-N}(x)}{\mathrm{d}x} \cdot B_j(x) + B_{i-N}(x) \cdot \tfrac{1}{2c}\tfrac{\mathrm{d}B_j(x)}{\mathrm{d}x} \right] dx \\ &= \tfrac{1}{2c} \int_a^b \left[\tfrac{\mathrm{d}B_{i-N}(x)}{\mathrm{d}x} \cdot B_j(x) + B_{i-N}(x) \cdot \tfrac{\mathrm{d}B_j(x)}{\mathrm{d}x} \right] dx \end{aligned} \tag{3.58}$$

Hamiltonian matrix:

$$\mathrm{H}_{i,j}^{[\beta]} = \int_a^b \Big[\tfrac{1}{2c}\tfrac{\mathrm{d}B_{i-N}(x)}{\mathrm{d}x}\big(c^2+\phi(x)\big)B_j(x) - c\tfrac{1}{2c}\tfrac{\mathrm{d}B_{i-N}(x)}{\mathrm{d}x}\cdot\tfrac{1}{2c}\tfrac{\mathrm{d}^2B_j(x)}{\mathrm{d}x^2} + \tag{3.59}$$

$$+ cB_{i-N}(x)\cdot\tfrac{\mathrm{d}B_j(x)}{\mathrm{d}x} + B_{i-N}(x)\big(-c^2+\phi(x)\big)\tfrac{1}{2c}\tfrac{\mathrm{d}B_j(x)}{\mathrm{d}x}\Big]\,dx$$

$$\mathrm{H}_{i,j}^{[\beta]} = \frac{1}{2c}\int_a^b \Big[\big(-c^2+\phi(x)\big)\cdot\Big(\tfrac{\mathrm{d}B_{i-N}(x)}{\mathrm{d}x}\cdot B_j(x) + B_{i-N}(x)\cdot\tfrac{\mathrm{d}B_{j-N}(x)}{\mathrm{d}x}\Big) + \tag{3.60}$$

$$+ \tfrac{1}{2}\tfrac{\mathrm{d}B_{i-N}(x)}{\mathrm{d}x}\cdot\tfrac{\mathrm{d}^2B_j(x)}{\mathrm{d}x^2}\Big]\,dx$$

$$\textbf{Submatrix } \gamma: \begin{cases} 1 \le i \le N \\ N+1 \le j \le 2N \end{cases} \Longrightarrow \begin{array}{l} \begin{pmatrix} f_i \\ g_i \end{pmatrix} = \begin{pmatrix} B_i(x) \\ \frac{1}{2c}\frac{\mathrm{d}B_i(x)}{\mathrm{d}x} \end{pmatrix} \\ \begin{pmatrix} f_j \\ g_j \end{pmatrix} = \begin{pmatrix} \frac{1}{2c}\frac{\mathrm{d}B_{j-N}(x)}{\mathrm{d}x} \\ B_{j-N}(x) \end{pmatrix} \end{array}$$

Overlap matrix:

$$\begin{aligned} \mathrm{S}_{i,j}^{[\gamma]} &= \int_a^b \Big[B_i(x)\cdot\tfrac{1}{2c}\tfrac{\mathrm{d}B_{j-N}(x)}{\mathrm{d}x} + \tfrac{1}{2c}\tfrac{\mathrm{d}B_i(x)}{\mathrm{d}x}\cdot B_{j-N}(x)\Big]\,dx \\ &= \tfrac{1}{2c}\int_a^b \Big[B_i(x)\cdot\tfrac{\mathrm{d}B_{j-N}(x)}{\mathrm{d}x} + \tfrac{\mathrm{d}B_i(x)}{\mathrm{d}x}\cdot B_{j-N}(x)\Big]\,dx \end{aligned} \tag{3.61}$$

Hamiltonian matrix:

$$\mathrm{H}_{i,j}^{[\gamma]} = \int_a^b \Big[B_i(x)\big(c^2+\phi(x)\big)\tfrac{1}{2c}\tfrac{\mathrm{d}B_{j-N}(x)}{\mathrm{d}x} - cB_i(x)\cdot\tfrac{\mathrm{d}B_{j-N}(x)}{\mathrm{d}x} + \tag{3.62}$$

$$+ \tfrac{c}{2c}\tfrac{\mathrm{d}B_i(x)}{\mathrm{d}x}\cdot\tfrac{1}{2c}\tfrac{\mathrm{d}B_{j-N}(x)}{\mathrm{d}x} + \tfrac{1}{2c}\tfrac{\mathrm{d}B_i(x)}{\mathrm{d}x}\big(-c^2+\phi(x)\big)B_{j-N}(x)\Big]\,dx$$

$$\mathrm{H}_{i,j}^{[\gamma]} = \frac{1}{2c}\int_a^b \Big[\big(c^2+\phi(x)\big)\cdot\Big(B_i(x)\cdot\tfrac{\mathrm{d}B_{j-N}(x)}{\mathrm{d}x} + \tfrac{\mathrm{d}B_i(x)}{\mathrm{d}x}\cdot B_{j-N}(x)\Big) - \tag{3.63}$$

$$- \tfrac{1}{2}\tfrac{\mathrm{d}B_i(x)}{\mathrm{d}x}\cdot\tfrac{\mathrm{d}^2B_{j-N}(x)}{\mathrm{d}x^2}\Big]\,dx$$

$$\textbf{Submatrix } \delta: \begin{cases} N+1 \le i \le 2N \\ N+1 \le j \le 2N \end{cases} \Longrightarrow \begin{array}{l} \begin{pmatrix} f_i \\ g_i \end{pmatrix} = \begin{pmatrix} \frac{1}{2c}\frac{\mathrm{d}B_{i-N}(x)}{\mathrm{d}x} \\ B_{i-N}(x) \end{pmatrix} \\ \begin{pmatrix} f_j \\ g_j \end{pmatrix} = \begin{pmatrix} \frac{1}{2c}\frac{\mathrm{d}B_{j-N}(x)}{\mathrm{d}x} \\ B_{j-N}(x) \end{pmatrix} \end{array}$$

Overlap matrix:

$$
\begin{aligned}
\mathrm{S}_{i,j}^{[\delta]} &= \int_a^b \left[\tfrac{1}{2c} \tfrac{\mathrm{d}B_{i-N}(x)}{\mathrm{d}x} \cdot \tfrac{1}{2c} \tfrac{\mathrm{d}B_{j-N}(x)}{\mathrm{d}x} + B_{i-N}(x) \cdot B_{j-N}(x) \right] dx \\
&= \int_a^b \left[B_{i-N}(x) \cdot B_{j-N}(x) + \tfrac{1}{4c^2} \tfrac{\mathrm{d}B_{i-N}(x)}{\mathrm{d}x} \cdot \tfrac{\mathrm{d}B_{j-N}(x)}{\mathrm{d}x} \right] dx
\end{aligned}
\tag{3.64}
$$

Hamiltonian matrix:

$$
\begin{aligned}
\mathrm{H}_{i,j}^{[\delta]} &= \int_a^b \left[\tfrac{1}{2c} \tfrac{\mathrm{d}B_{i-N}(x)}{\mathrm{d}x} \big(c^2 + \phi(x)\big) \tfrac{1}{2c} \tfrac{\mathrm{d}B_{j-N}(x)}{\mathrm{d}x} - \tfrac{c}{2c} \tfrac{\mathrm{d}B_{i-N}(x)}{\mathrm{d}x} \cdot \tfrac{\mathrm{d}B_{j-N}(x)}{\mathrm{d}x} + \right. \qquad (3.65) \\
&\qquad \left. + cB_{i-N}(x) \cdot \tfrac{1}{2c} \tfrac{\mathrm{d}^2 B_{j-N}(x)}{\mathrm{d}x^2} + B_{i-N}(x) \big(-c^2 + \phi(x)\big) B_{j-N}(x) \right] dx \\
\mathrm{H}_{i,j}^{[\delta]} &= \int_a^b \left[\big(-c^2 + \phi(x)\big) \cdot \Big(B_{i-N}(x) \cdot B_{j-N}(x) + \tfrac{1}{4c^2} \tfrac{\mathrm{d}B_{i-N}(x)}{\mathrm{d}x} \cdot \tfrac{\mathrm{d}B_{j-N}(x)}{\mathrm{d}x} \Big) - \right. \qquad (3.66) \\
&\qquad \left. - \tfrac{1}{2} B_{i-N}(x) \cdot \tfrac{\mathrm{d}^2 B_{j-N}(x)}{\mathrm{d}x^2} \right] dx
\end{aligned}
$$

From the simplifications performed in this subsection, the set of integrands that need to be calculated has been reduced to the following 10:

(α, δ)		(β, γ)	
$B_i(x) \cdot B_j(x)$	$\frac{\mathrm{d}B_i(x)}{\mathrm{d}x} \cdot \frac{\mathrm{d}B_j(x)}{\mathrm{d}x}$	$B_i(x) \cdot \frac{\mathrm{d}B_j(x)}{\mathrm{d}x}$	$\frac{\mathrm{d}B_i(x)}{\mathrm{d}x} \cdot B_j(x)$
$\phi(x) \cdot B_i(x) \cdot B_j(x)$	$\phi(x) \cdot \frac{\mathrm{d}B_i(x)}{\mathrm{d}x} \cdot \frac{\mathrm{d}B_j(x)}{\mathrm{d}x}$	$\phi(x) \cdot B_i(x) \cdot \frac{\mathrm{d}B_j(x)}{\mathrm{d}x}$	$\phi(x) \cdot \frac{\mathrm{d}B_i(x)}{\mathrm{d}x} \cdot B_j(x)$
$B_i(x) \cdot \frac{\mathrm{d}^2 B_j(x)}{\mathrm{d}x^2}$		$\frac{\mathrm{d}B_i(x)}{\mathrm{d}x} \cdot \frac{\mathrm{d}^2 B_j(x)}{\mathrm{d}x^2}$	

Table 3.2.3.1: Integrands that need to be calculated in the numerical solution of the 1D TIDE (3.23) in the DKB B-spline basis representation (3.51).

Most results from implementing the DKB B-spline representation (3.51) as solutions to the 1D TIDE (3.23) will be retained until section 4.3, where they will be discussed at length. For now, it will suffice to show that the jittering that was present in both previous approaches [see (3.32) and (3.50), with illustrations in Figs. 3.2a-g], does not present itself when the DKB B-spline representation (3.51) is used.

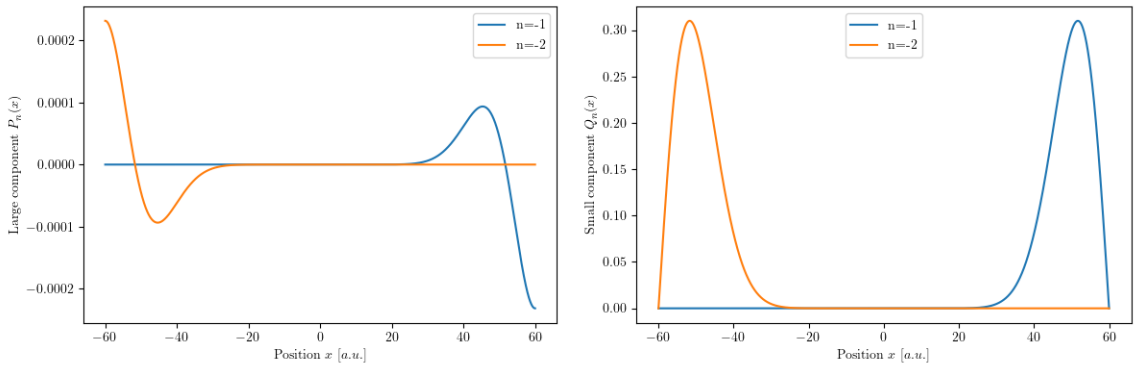

Figure 3.2h: Large (left image) and small (right image) components to the first two negative energy solutions to the 1D TIDE (3.20) in DKB B-spline representation (3.51).
$k = 8$, $(a, b) = (-60, 60)$, $n_{internal\,knots} = 8000$, $Z = 5$

Looking at the wave functions in fig. 3.2h, and specifically at the smoothness of the curves, one will immediately notice the absence of the jittering which was so prevalent in the previous B-spline bases (See figs. 3.2c, d, f and g). Additionally, one might from fig. 3.2h notice that the negative energy solutions to the 1D TIDE (3.20) in DKB B-spline representation (3.51) are heavily weighted toward the edges of the one-dimensional "box". This is in fact the case for all box sizes (a, b) which have been tested during the current work, for both the large and small components. To illustrate the density of states, as was done in Figs. 3.2-1 and 3.2-2, but now for a DKB B-spline basis:

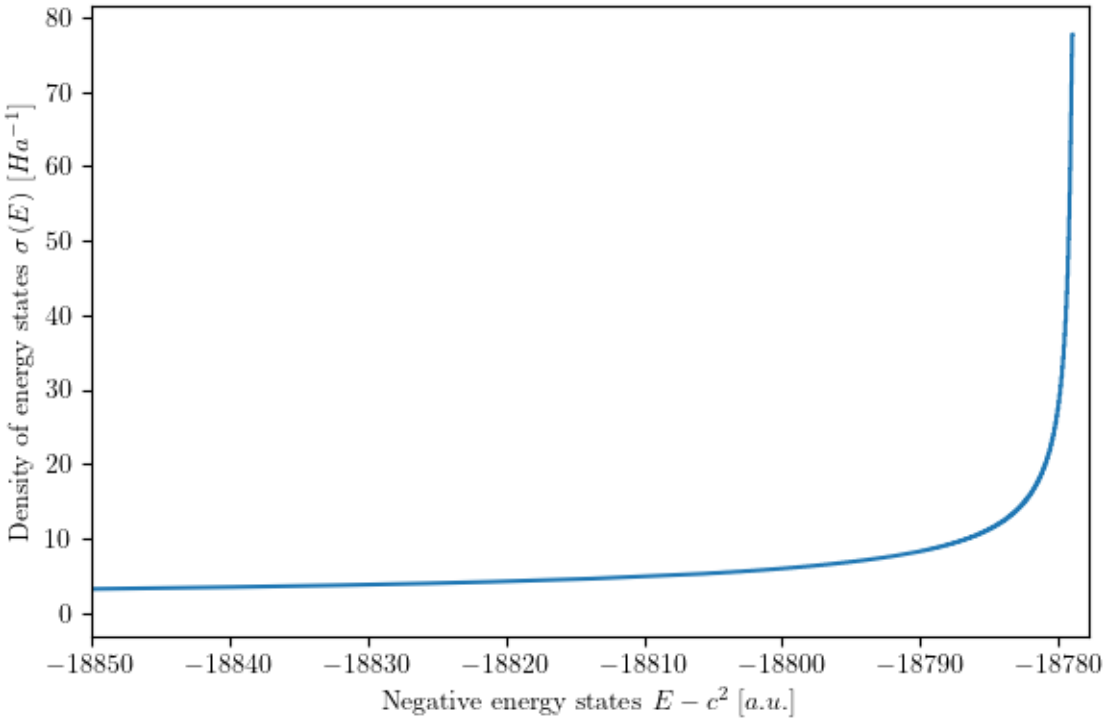

Figure 3.2-3: Density of negative energy solutions to the 1D TIDE (3.20) in DKB B-spline representation (3.51). $k = 8$, $(a, b) = (-60, 60)$, $n_{internal\,knots} = 8000$, $Z = 5$

Fig. 3.2-3 shows that implementing a DKB B-spline representation (3.51) to solve the 1D TIDE (3.20) gets rid of the spurious states that were present in the two first approaches, as illustrated in figs. 3.2-1 and 3.2-2. Therefore, going forwards, it is assumed that the 1D TIDE (3.20) for an electron in a central potential has known solutions in DKB B-spline representation (3.51). The solutions will be further discussed in sec. 4.3, but it is helpful to first formulate an approach which will be used to investigate the time-evolution of the model.

3.3 Time propagation of the Dirac model

To regard the time-evolution of some model, for which an initial state has been determined by solving the 1D TIDE (2.30), it is only natural to remain within the Dirac-framework. As a reminder, the one-dimensional time-dependent Dirac equation (1D TDDE) which will be used to model the time-evolution of the system is given by eq. (2.20).

$$i\frac{\partial\Psi(x,t)}{\partial t} = \big[c\sigma_2(\hat{\mathrm{p}} - A(t)) + \sigma_3 c^2 + \mathbb{I}_2\phi(x)\big]\Psi(x,t) \tag{3.67}$$

The Hamiltonian corresponding to eq. (3.67) can be expressed as (2.21)

$$H_{1D}^{TDDE} = \left[c\sigma_2\left(-i\frac{\partial}{\partial x} - A(t)\right) + \sigma_3 c^2 + \mathbb{I}_2\phi(x)\right], \tag{3.68}$$

from which the time-dependent and space-dependent parts can be separated, as described in eq. (2.42).

$$H_{1D}^{TDDE} = H_{1D}^{TIDE} + H_{1D}^{D}(t) \tag{3.69}$$

In (3.69), H_{1D}^{TIDE} is given by (2.26), while $H_{1D}^{D}(t)$ "the Hamiltonian of Interaction" is expressed as in eq. (2.41):

$$H_{1D}^{D}(t) = -c\sigma_2 A(t) = -icA(t)\begin{pmatrix} 0 & -1 \\ 1 & 0 \end{pmatrix} \tag{3.70}$$

From the expressions above, coupled with the assumption that solutions to the 1D TIDE are known, some substitutions can be made. From (2.47)

$$\langle\psi_k| \sum_{n=1}^{2N} i\dot{c}_n(t)\,|\psi_n\rangle = \langle\psi_k| \sum_{n=1}^{2N} c_n(t)\big[H_{1D}^{TIDE} + H_{1D}^{D}(t)\big]\,|\psi_n\rangle\,, \tag{3.71}$$

with known, orthonormal solutions for $\langle\psi_k|$ and $|\psi_n\rangle$, and the 1D TIDE (3.23), these substitutions (also expressed in the underbraces of eq. (2.48)) can be written as below.

$$\langle \psi_k | \psi_n \rangle \quad \longrightarrow \quad \delta_{k,n} \tag{3.72}$$

$$\langle \psi_k | H_{1D}^{TIDE} | \psi_n \rangle \quad \longrightarrow \quad E_n \delta_{k,n} \tag{3.73}$$

Furthermore, a name change is performed for the remaining inner product of (3.71), by inserting the expression for the Hamiltonian of interaction from (3.70). The inner product is expressed as

$$\langle \psi_k | H_{1D}^{D}(t) | \psi_n \rangle = -icA(t) \underbrace{\int_b^a [P_k^*(x) \cdot Q_n(x) - Q_k^*(x) \cdot P_n(x)] \, \mathrm{d}x}_{=V_{k,n}}, \tag{3.74}$$

or, in shorthand,

$$\langle \psi_k | H_{1D}^{D}(t) | \psi_n \rangle \quad = \quad -iA(t) V_{k,n} \, , \tag{3.75}$$

$$\text{with} \qquad V_{k,n} \quad \coloneqq \quad \int_b^a [P_k^*(x) \cdot Q_n(x) - Q_k^*(x) \cdot P_n(x)] \, \mathrm{d}x \, . \tag{3.76}$$

Inserting the substitutions from (3.72), (3.73) and (3.75) to the 1D TDDE (3.71), the equation for the time-evolution of the system can be transformed to the following.

$$\underbrace{i \sum_{n=1}^{2N} \dot{c}_n(t) \delta_{k,n}}_{=\dot{c}_k(t)} = \sum_{n=1}^{2N} c_n(t) [E_n \delta_{k,n} - iA(t) V_{k,n}] \tag{3.77}$$

Now, multiplying eq. (3.77) by $-i$, for every k such that $1 \leq k \leq 2N$, the equation can be rewritten in the form of a matrix eigenvalue problem.

$$\frac{d}{dt} \begin{bmatrix} c_1(t) \\ c_2(t) \\ \vdots \\ c_N(t) \end{bmatrix} = \left(-i \begin{bmatrix} E & 0 & \cdots & 0 \\ 0 & E_2 & \cdots & 0 \\ \vdots & \vdots & \ddots & \vdots \\ 0 & 0 & \cdots & E_N \end{bmatrix} - cA(t) \begin{bmatrix} V_{1,1} & V_{1,2} & \cdots & V_{1,N} \\ V_{2,1} & V_{2,2} & \cdots & V_{2,N} \\ \vdots & \vdots & \ddots & \vdots \\ V_{N,1} & V_{N,2} & \cdots & V_{N,N} \end{bmatrix} \right) \begin{bmatrix} c_1(t) \\ c_2(t) \\ \vdots \\ c_N(t) \end{bmatrix} \tag{3.78}$$

By expressing the two matrices on the RHS of (3.78) as a Hermitian, time-dependent Hamiltonian $H(t)$, this can again be rewritten.

$$\frac{d}{dt} \vec{c}(t) = \left(-i\vec{E} \mathbb{1}_{N \times N} - cA(t) \mathrm{V}_{N \times N} \right) \vec{c}(t) = H(t) \vec{c}(t) \tag{3.79}$$

The form of eq. (3.79) can be recognised as a system of first-order differential equations. A common way to solve such systems is by integrating factor. By setting μ as

$$\mu \quad = \quad \exp\left(- \int_0^t H(\tau) \, d\tau \right) \, , \tag{3.80}$$

its time-derivative $\frac{\mathrm{d}\mu}{\mathrm{d}t}$ can be written as

$$\frac{d\mu}{dt} = -\exp\left(-\int_0^t H(\tau)\,d\tau\right) H(t) = -\mu H(t)\,. \tag{3.81}$$

Now the integrating factor μ (3.80) is multiplied with eq. (3.79) from the left,

$$\mu\frac{d\vec{c}(t)}{dt} = \mu H(t)\vec{c}(t) = -\frac{d\mu}{dt}\vec{c}(t)\,, \tag{3.82}$$

which, when exposed to the product rule, can be rephrased as

$$\mu\frac{d\vec{c}(t)}{dt} + \frac{d\mu}{dt}\vec{c}(t) = 0 \tag{3.83}$$

$$\frac{d}{dt}(\mu\vec{c}(t)) = 0\,. \tag{3.84}$$

In spite of its miniscule size and unassuming form, eq. (3.84) is still the identity which governs the time-evolution of any system of eigenstates which solve the 1D TIDE (3.20). As such, with the intent of solving this equation, an expansion is in order. First, integrating over the time-interval $t \to t + \Delta t$ is performed on 3.84, . By applying some tricks for integration (specifically setting $t \to t'$ within the integral) and inserting the expression for μ as it was written in (3.80), the integral of eq. (3.84) can be expressed and manipulated as below.

$$0 = \int_t^{t+\Delta t}\left[\frac{d}{dt'}(\mu\vec{c}(t'))\right]\mathrm{d}t' \tag{3.85}$$

$$= \int_t^{t+\Delta t}\frac{d}{dt'}\left[\exp\left(-\int_0^{t'} H(\tau)\,d\tau\right)\vec{c}(t')\right]dt' \tag{3.86}$$

$$= \exp\left(-\int_0^{t'} H(\tau)\,d\tau\right)\vec{c}(t')\Bigg|_{t'=t}^{t'=t+\Delta t} \tag{3.87}$$

$$= \exp\left(-\int_0^{t+\Delta t} H(\tau)\,d\tau\right)\vec{c}(t+\Delta t) - \exp\left(-\int_0^{t} H(\tau)\,d\tau\right)\vec{c}(t) \tag{3.88}$$

Now, since the matrix contained within the exponential must be a Hermitian matrix, eq. (3.88) can be multiplied with $\exp\left(\int_0^{t+\Delta t} H(\tau)\,d\tau\right)$ from the left to give

$$\vec{c}(t+\Delta t) = \exp\left(\int_0^{t+\Delta t} H(\tau)\,d\tau - \int_0^{t} H(\tau)\,d\tau\right)\vec{c}(t) \tag{3.89}$$

$$= \exp\left(\int_t^{t+\Delta t} H(\tau)\,d\tau\right)\vec{c}(t)\,, \tag{3.90}$$

which, through Riemann integration (as $\Delta t \ll 1$), becomes

$$\vec{c}(t + \Delta t) = \exp(H(t)\Delta t)\, \vec{c}(t) \tag{3.91}$$

This formulation brings with it some issues, as matrix exponentials oftentimes are unwieldy. Due to the system only existing in one dimension, however, brute-forcing the calculations by simply diagonalising the matrix in the exponential becomes a viable method. For each step of the time propagation, the matrix exponential $\exp(H(x)\Delta t)$ will be diagonalised numerically by employing the algorithm contained in the module "scipy.linalg.eig". This is done by solving the given matrix for its left and right eigenvectors,

$$A = PDP^{-1} \Longrightarrow D = P^{-1}AP\,, \tag{3.92}$$

which also applies to matrix exponentials on the form

$$\exp(A) = P\exp(D)P^{-1} \Longrightarrow \exp(D) = P^{-1}\exp(A)P\,. \tag{3.93}$$

The evolution of the system in time will be approximated by incremental propagation in steps of Δt, using the expression

$$\vec{c}(t + \Delta t) = P\exp(D)P^{-1}\vec{c}(t)\,, \tag{3.94}$$

where D is the diagonalising matrix and P and P^{-1} is and the right and left eigenvectors that solve the eigenvalue problem $P^{-1}(\Delta t H(t))P = D$. Now, using the ground state energy as the initial state of the system, each time step can be approximated by performing the matrix multiplication expressed in the above equation. Repeated an amount of times, this ultimately gives approximation for the probability differential with regards to energy density.

3.4 B-spline representation of the TISE

This section is intentionally kept brief, as the methods being employed within it are significantly less intricate than the ones involved in solving the 1D TIDE in sec. 3.2.

To begin, the stationery states that are solutions to the 1D TISE (2.58) are assumed to be approximated by a linear combination of B-spline basis functions. With ψ given as

$$\psi(x) = \sum_{j=1}^{N} c_j B_j(x)\,, \tag{3.95}$$

the 1D TISE (2.58) can be rewritten as follows.

$$\sum_{j=1}^{N} c_j \left[-\frac{1}{2} \frac{\mathrm{d}^2 B_j(x)}{\mathrm{d}x^2} + \phi(x) \cdot B_j(x) \right] = E \sum_{j=1}^{N} c_j B_j(x) \tag{3.96}$$

Eq. (3.96) is multiplied by the series consisting of the basis functions $\sum_{i=1}^{N} B_i(x)$ from the left, before integrating over the x-interval.

$$\sum_{i=1}^{N} \sum_{j=1}^{N} c_j \int_a^b \left[-\frac{1}{2} B_i(x) \frac{\mathrm{d}^2 B_j(x)}{\mathrm{d}x^2} + B_i(x) \cdot \phi(x) \cdot B_j(x) \right] dx = E \sum_{i=1}^{N} \sum_{j=1}^{N} c_j \int_a^b B_i(x) \cdot B_j(x)\, dx \tag{3.97}$$

Abbreviating the integrals in this equation

$$\begin{aligned} \text{LHS} \longrightarrow \mathrm{H}_{i,j} &\coloneqq \int_a^b \left[-\frac{1}{2} B_i(x) \cdot \frac{\mathrm{d}^2 B_j(x)}{\mathrm{d}x^2} + B_i(x) \cdot \phi(x) \cdot B_j(x) \right] dx\,, \qquad (3.98) \\ &\text{and} \\ \text{RHS} \longrightarrow \mathrm{S}_{i,j} &\coloneqq \int_a^b B_i(x) \cdot B_j(x)\, dx \qquad (3.99) \end{aligned}$$

makes formulating the eigenvalue problem as a matrix equation more practical. With λ being the eigenvalue from 1D TISE Hamiltonian (2.59), eq. (2.64) can be expressed as

$$\begin{pmatrix} \mathrm{H}_{1,1} & \mathrm{H}_{1,2} & \cdots & \mathrm{H}_{1,\mathrm{N}} \\ \mathrm{H}_{2,1} & \mathrm{H}_{2,2} & \cdots & \mathrm{H}_{2,\mathrm{N}} \\ \vdots & \vdots & \ddots & \vdots \\ \mathrm{H}_{\mathrm{N},1} & \mathrm{H}_{\mathrm{N},2} & \cdots & \mathrm{H}_{\mathrm{N,N}} \end{pmatrix} \begin{pmatrix} c_1 \\ c_2 \\ \vdots \\ c_N \end{pmatrix} = \lambda \begin{pmatrix} \mathrm{S}_{1,1} & \mathrm{S}_{1,2} & \cdots & \mathrm{S}_{1,\mathrm{N}} \\ \mathrm{S}_{2,1} & \mathrm{S}_{2,2} & \cdots & \mathrm{S}_{2,\mathrm{N}} \\ \vdots & \vdots & \ddots & \vdots \\ \mathrm{S}_{\mathrm{N},1} & \mathrm{S}_{\mathrm{N},2} & \cdots & \mathrm{S}_{\mathrm{N,N}} \end{pmatrix} \begin{pmatrix} c_1 \\ c_2 \\ \vdots \\ c_N \end{pmatrix}, \tag{3.100}$$

Regarding the choice of matrix dimension, the TISE (2.58) and TIDE (2.24) models differ somewhat. Whereas the eigenstate solutions to the 1D TIDE come in the form of wave spinors, as well as being permitted negative energy states, the TISE requires neither of these. As such, the 1D TISE will be solved numerically in a $N \times N$ eigenvalue matrix problem. The matrix representation of the eigenvalue problem (3.100) can be abbreviated

$$\boldsymbol{h}\vec{c} = E\boldsymbol{s}\vec{c} \tag{3.101}$$

Running the script, this method seems to yield less problems than the original attempts for the Dirac script. The system is inherently much simpler, in part due to having a significantly shorter Hamiltonian, but also due to not requiring some interaction between the large and small components of the Dirac system. The results of the solutions to the 1D TISE will therefore in full be presented in chapter 4.

With the wave functions and eigenvalues of the time-independent system completed, calculations on the time-evolution will commence.

3.5 1D TDSE in laser potential

Following eq. (2.73), the time-evolution of the 1D Schrödinger system is given by

$$\dot{c}_k(t) = \sum_{n=1}^{N} c_n(t)\Big[-iE_n\delta_{k,n} - iV_{k,n}^{'}\Big], \tag{3.102}$$

where $c_n(t)$ is the coefficient for the n-th eigenstate at the time t, E_n is its corresponding energy, and $V_{k,n}^{'}$ is defined by (2.72). The integral contained within $V_{k,n}^{'}$ is calculated by Gauss-Legendre integration, using the wave functions found by solving the TISE. Specifically, to facilitate the difference in time dependence within it, the integral is separated to two parts. From (2.72):

$$\begin{aligned} V_{k,n}^{'} &= A(t)\int_{\Omega}\left[i\psi_k(x)\cdot\frac{\mathrm{d}\psi_n(x)}{\mathrm{d}x} + \frac{A(t)}{2}\cdot\psi_k(x)\cdot\psi_n(x)\right]\mathrm{d}x \\ V_{k,n}^{'} &= iA(t)\int_{\Omega}\psi_k(x)\cdot\frac{\mathrm{d}\psi_n(x)}{\mathrm{d}x}\,\mathrm{d}x + \frac{A(t)^2}{2}\underbrace{\int_{\Omega}\psi_k(x)\cdot\psi_n(x)\,\mathrm{d}x}_{=\delta_{k,n}} \qquad (3.103) \\ &= iA(t)\int_{\Omega}\psi_k(x)\cdot\frac{\mathrm{d}\psi_n(x)}{\mathrm{d}x}\,\mathrm{d}x + \frac{A(t)^2}{2}\delta_{k,n} \qquad (3.104) \end{aligned}$$

The values given by $V_{k,n}^{'}$ also satisfy $V_{k,n}^{'} = V_{n,k}^{'*}$, as it is composed exclusively from Hermitian operators. To formulate the time propagation of the total wave function, it is useful to state it in the way of matrices.

Repeating the process to arrive at the expression for $\dot{c}_k(t)$ for every $1 \le k \le N$ facilitates the representation of equation (2.73) in matrix form,

$$\frac{\mathrm{d}}{\mathrm{d}t}\begin{pmatrix} c_1 \\ c_2 \\ \vdots \\ c_N \end{pmatrix} = -i\left[\begin{pmatrix} E_1 & 0 & \cdots & 0 \\ 0 & E_2 & \cdots & 0 \\ \vdots & \vdots & \ddots & \vdots \\ 0 & 0 & \cdots & E_n \end{pmatrix} + \begin{pmatrix} V_{1,1}^{'} & V_{1,2}^{'} & \cdots & V_{1,N}^{'} \\ V_{2,1}^{'} & V_{2,2}^{'} & \cdots & V_{2,N}^{'} \\ \vdots & \vdots & \ddots & \vdots \\ V_{N,1}^{'} & V_{N,2}^{'} & \cdots & V_{N,N}^{'} \end{pmatrix}\right]\begin{pmatrix} c_1 \\ c_2 \\ \vdots \\ c_N \end{pmatrix} \tag{3.105}$$

which can be shortened into the Hermitian, time-dependent Hamiltonian $H^{SE}(t)$, governing the time evolution of the system.

$$\dot{\vec{c}}(t) = -i\left(\underbrace{E\mathbb{1}_{N\times N} + \mathrm{V}_{N\times N}^{'}}_{=H^{SE}(t)}\right)\vec{c}(t) = -iH^{SE}(t)\vec{c}(t) \tag{3.106}$$

Or, more practically,

$$\dot{\vec{c}}(t) + iH^{SE}(t)\vec{c}(t) = 0 \tag{3.107}$$

This system of differential equations can, similar to the case of the Dirac equation, be solved by method of integrating factor,

$$\mu = \exp\left(i\int_0^t H^{SE}(\tau)\mathrm{d}\tau\right) \tag{3.108}$$

$$\longrightarrow \frac{\mathrm{d}\mu}{\mathrm{d}t} = i\mu H^{SE}(t) \tag{3.109}$$

$$\frac{\mathrm{d}}{\mathrm{d}t}(\mu\vec{c}(t)) = \mu\dot{\vec{c}}(t) + i\mu H^{SE}(t)\vec{c}(t) = 0 \tag{3.110}$$

and then taking the time-integral from $t \to t + \Delta t$.

$$\begin{aligned}
0 &= \int_t^{t+\Delta t} \frac{\mathrm{d}}{\mathrm{d}t}\left[\exp\left(i\int_0^{t'} H^{SE}(\tau)d\tau\right)\vec{c}(t')\right]\mathrm{d}t' && (3.111)\\
&= \left[\exp\left(i\int_0^{t'} H^{SE}(\tau)d\tau\right)\vec{c}(t')\right|_{t'=t}^{t'=t+\Delta t} && (3.112)\\
&= \exp\left(i\int_0^{t+\Delta t} H^{SE}(\tau)d\tau\right)\vec{c}(t+\Delta t) - \exp\left(i\int_0^{t} H^{SE}(\tau)d\tau\right)\vec{c}(t) && (3.113)
\end{aligned}$$

From here, (3.113) is multiplied with $\exp\left(-i\int_0^{t+\Delta t} H^{SE}(\tau)d\tau\right)$ from the left, yielding

$$\begin{aligned}
\vec{c}(t+\Delta t) &= \exp\left(i\left[\int_0^t H^{SE}(\tau)d\tau - \int_0^{t+\Delta t} H^{SE}(\tau)d\tau\right]\right)\vec{c}(t) && (3.114)\\
\vec{c}(t+\Delta t) &= \exp\left(-i\int_t^{t+\Delta t} H^{SE}(\tau)d\tau\right)\vec{c}(t)\,. && (3.115)
\end{aligned}$$

Applying Riemann integration to (3.115) as $\Delta t \ll 1$ gives

$$\vec{c}(t+\Delta t) = \exp\big(-iH^{SE}(t)\Delta t\big)\vec{c}(t)\,, \tag{3.116}$$

which will be solved numerically by diagonalising the matrix exponential,

$$\vec{c}(t+\Delta t) = P^{-1}\exp(D)P\,\vec{c}(t)\,, \tag{3.117}$$

in a very similar fashion to the time propagation presented in sec. 3.3's eq. (3.94).

3.6 The modeled vector potential

To be able to accurately predict the time-evolution of some system modeled by the 1D TDSE (2.66) and the 1D TDDE (2.51), it is important to present a well-defined model of the field (2.79) with which the systems are to interact. Repeating the expression for the vector potential $A(t)$ from (2.79):

$$A(t) = \frac{E_0}{\omega} \sin^2\left(\frac{\pi t}{T_{pulse}}\right) \sin(\omega t)\,, \tag{3.118}$$

The parameters within this expression influence the shape of the pulse, and thereby its interaction with the modeled systems, in various ways. The pulse is chosen to contain 15 periods, setting $T = 15 \cdot \frac{2\pi}{\omega}$, and an angular frequency of $\omega = 50\,a.u.$ Furthermore, outcomes from different configurations of the electric field strength E_0 will be investigated with the intent of comparing ionization probability for the 1D Dirac and Schrödinger models. Below is an illustration intended to show the shape of the laser pulse.

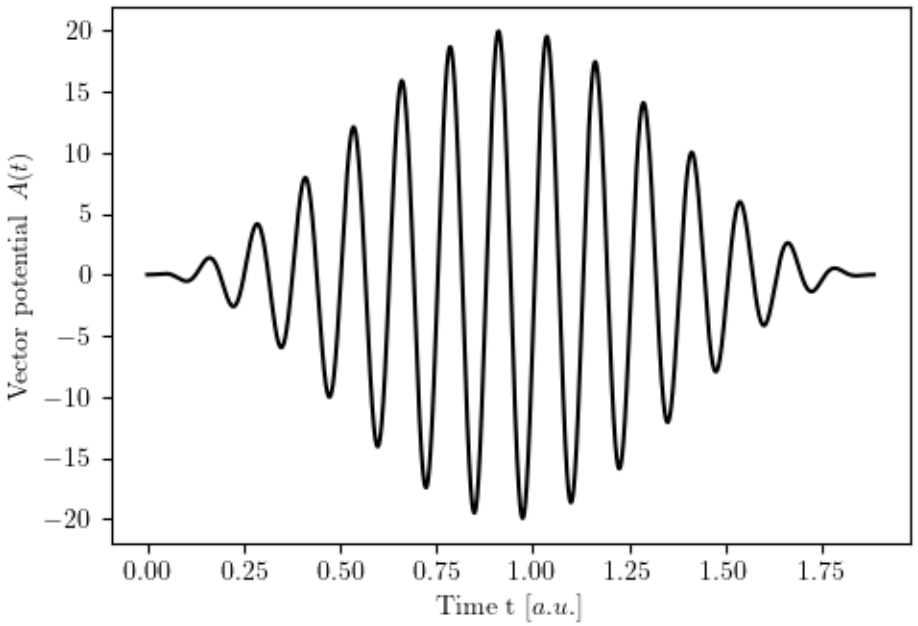

Figure 3.6a: Modeled vector potential $A(t)$ (3.118) with $T_{pulse} = 15 \cdot \frac{2\pi}{\omega}$, $\omega = 50$, $E_0 = 1000$, $n_{\Delta t} = 7000$

The configuration presented in the figure text of fig. 3.6a, notwithstanding the electric field strength amplitude E_0 (as explained in last paragraph), will be used as the standard configuration for most results presented in chapter 4.

3.7 Energy probability differential

In the physical world, the permitted energy states of a free electron is a continuum. Thus, to accurately represent numerical findings which contain a finite set of positive energy states, some approximations must be made to accommodate. The probability of observing an electron in a specific energy state i with corresponding energy E_i at some time t can be expressed as the absolute value squared of the coefficient $c_i(t)$ of the state:

$$P(i) = |c_i(t)|^2 \tag{3.119}$$

Now, seeing as the eigenstate bases of the 1D TIDE (3.20) and 1D TISE (2.58) which will be propagated in time by their respective propagators (3.91, 3.116) lacks the aforementioned continuum of free-electron states, this must be accounted for. The method in which this will be done is by expressing the probability distribution as a differential with regard to the density of numerical energy states from the model,

$$\frac{\mathrm{d}P(i)}{\mathrm{d}E} = P(i)\sigma(E_i) \simeq \frac{2}{E_{i+1} + E_{i-1}}\,, \tag{3.120}$$

as presented in [31].

Chapter 4

Numerical results

Before proceeding to the results of the numerical calculations carried out within this thesis, something should be pointed out. In general, and unless explicitly stated otherwise, results given in this chapter will have been based on the following parameters. The term Standard Configuration (SC) refers to the values listed in this table.

Parameter	Symbol	Standard configuration (SC)
Nuclear charge	Z	5
B-spline basis order	k	8
x–interval	(a, b)	$(-60, 60)$
Number of internal knots in knot sequence T	$n_{internal}$	16000
Edge splines for boundrary condition		$B_{initial}(x) = 0 = B_{final}(x)$
Number of positive energy states taken to propagation	n_{eigs}	1402
Number of time–intervals	$n_{\Delta t}$	7000
Angular frequency of the laser pulse	ω	50
Total pulse time	T_{pulse}	$15 \cdot \frac{2\pi}{\omega}$
Energy pobability differential	$\frac{\mathrm{d}P(i)}{\mathrm{d}E}$	$\frac{2\lvert c_i(t)\rvert^2}{E_{i+1}-E_{i-1}}$
Initial state of the system	$\vec{c}(0)$	$c_{g.s.}(0) = 1\,,\ c_{i\neq g.s.}(0) = 0$

Table 4.0-1: Standard configuration (SC) for results presented within this chapter.

4.1 Numerical solution to the 1D Schrödinger equation

Within section 4.1.1, numerical solutions to the modeled 1D TISE (2.58) will be presented, by representing the eigenstates of the equation in a a B-spline basis 3.95. Then in 4.1.2, the solutions found for the 1D TISE will be used as an eigenvalue basis to inspect the time–evolution of the system. This time–evolution will be caused by light–matter interactions between the modeled atom and some high-intensity laser pulse, and is governed by the time–propagator in (3.116).

4.1.1 Wave functions and eigenstates of the 1D TISE

Starting out by looking at the energy solutions to the 1D TISE (2.58) represented from a B–spline basis (3.95) in SC (table 4), as given in table 4.1.1 below.

State (n)	Numerical value (1D)	Analytic value (3D)	Absolute difference
1	−12.50000	−12.50000	$1.85 \cdot 10^{-12}$
2	−5.82258	−3.12500	$2.67 \cdot 10^{0}$
3	−3.34572	−1.38888	$1.96 \cdot 10^{0}$
4	−2.11945	−0.78125	$1.34 \cdot 10^{0}$
5	−1.47143	−0.50000	$0.97 \cdot 10^{0}$

Table 4.1.1: The 5 lowest energy solutions to the 1D TISE (2.58) in B–spline basis (3.95) and SC (table 4). Analytic values: Energy level determined by $E_n = -\frac{z^2}{2n^2}$. All energy values are listed in atomic units.

Immediately apparent is the near–identical values found for the ground state energy, in spite of the solutions being for systems with different numbers of dimensions. Modeling the Coulomb–potential as a soft–core potential (2.19) makes for high presicion in the ground state energy, whereas any excited state has had some error introduced from the approximation. This is the expected result, and should not impede the time–propagation of the system due to the introduction of the energy probability differential (3.120). Three wavefunctions corresponding to the energy states $n = \{1, 2, 3\}$ are illustrated below.

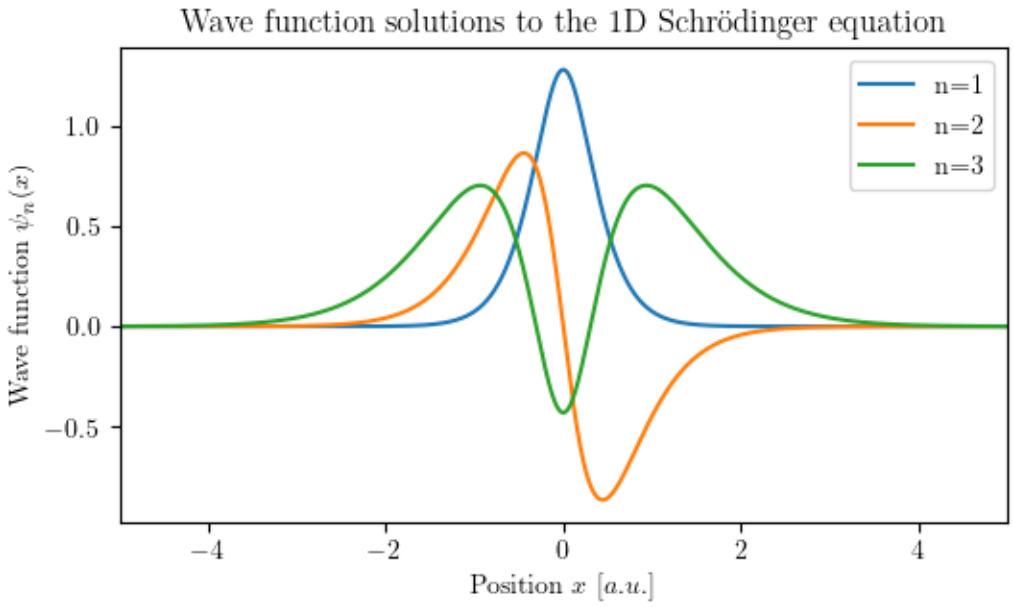

Figure 4.1.1: The three tightest–bound eigenstates of the 1D TISE (2.58) in B–spline representation (3.95) and SC (table 4).

Now, as the 1D TISE (2.58) for a particle in a central potential does not have analytic solutions, there isn't much to compare these wave functions that are presented in Fig. 4.1.1 with. The 1402 lowest energy solutions to the 1D TISE (2.58) are carried into another script, made to propagate the system in time.

4.1.2 Time–evolution after exposure to vector field

The results to be presented below are produced in the following fashion: First, an eigenvalue basis is constructed from the 1402 lowest energy solutions of the 1D TISE (2.58) in B–spline representation (3.95). Then, the modeled 1D system is propagated by applying the propagator from (3.116), by exposing the system to a laser pulse as in (3.118). This is done in standard configuration (SC), described in table 4. As was discussed in sec. 3.6, the electric field amplitude E_0 for the pulse will be adjusted between calculations to inspect the effect it has on the ionization probability of the modeled system. It is, to be precise, the same eigenvalue basis solving the 1D TISE (2.58) represented by B–spline basis (3.95) using SC (table 4) being propagated in time for all values of E_0, to keep results consistent with one another. Simulations were carried out in intervals of $100\,a.u.$ of electric field strength amplitude, starting from $E_0 = 100\,a.u.$ increasing up to $E_0 = 1500\,a.u.$

For low electric field strength amplitudes E_0, it will be shown that the energy probability differential 3.120 falls off dramatically at higher energy levels. Below is shown the energy probability differential with $E_0 = 100\,a.u.$, in fig. 4.1.2a. (NOTE: The interpolation which was performed on these emission spectra will be discussed in the corresponding section 4.2.2 on results in the Dirac framework)

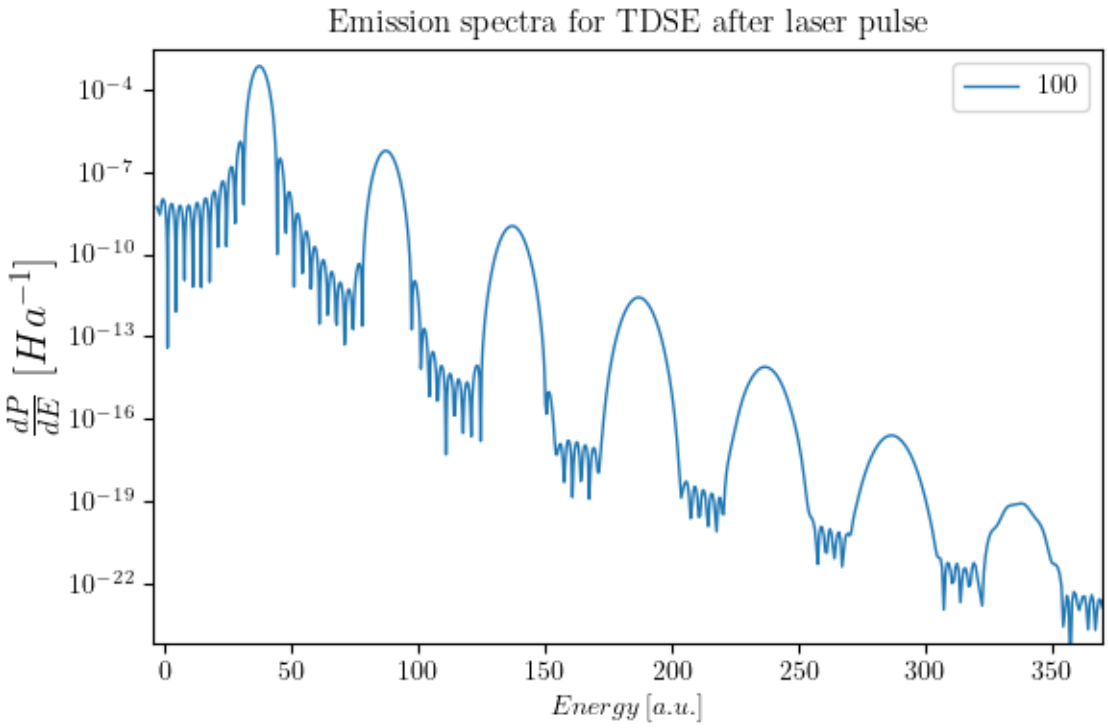

Figure 4.1.2a: Emission specter after propagating an eigenvalue basis from solving the 1D TISE (2.58) in B–spline basis (3.95), by applying the corresponding 1D TDSE propagator of (3.116) with $E_0 = 100\, a.u.$ and SC (table 4).

The graph in fig. 4.1.2a has been cut short, as values below 10^{-22} are more heavily influenced by machine precision. Due to the energy probability differential for the the multi–photon resonance differential being expressed in a logarithmic scale, it is necessary to inspect some system which experiences greater interaction with the laser pulse. Initial models were in fact done with a 1D model hydrogen atom, $Z = 1$. The energy probability differential resulting from the propagation of a 1D TISE (2.58) in B–spline basis (3.95) with $Z = 1$ in the propagator were orders of magnitude smaller than fig. 4.1.2a shows. The results became heavily influenced by "machine precision noise" to the point where they became unintelligible. Based on recommendation from supervisor M. Førre, the proton number $Z = 5$ is used in these calculations instead. A handy attribute of the configuration $Z = 5$, when combined with the angular frequency $\omega = 50\, a.u.$, is that the absorption of a single photon enough to ionize the hydrogenic model ($E_{g.s.} \sim -12.5$). As such, bound excited states are of smaller importance, which is helpful to the 1D model, as the soft–core approximation (2.19) of the Coulomb potential makes them less precise 4.1.1.

Further investigating the energy probability differential will be done, and some results are illustrated in fig. 4.1.2b below.

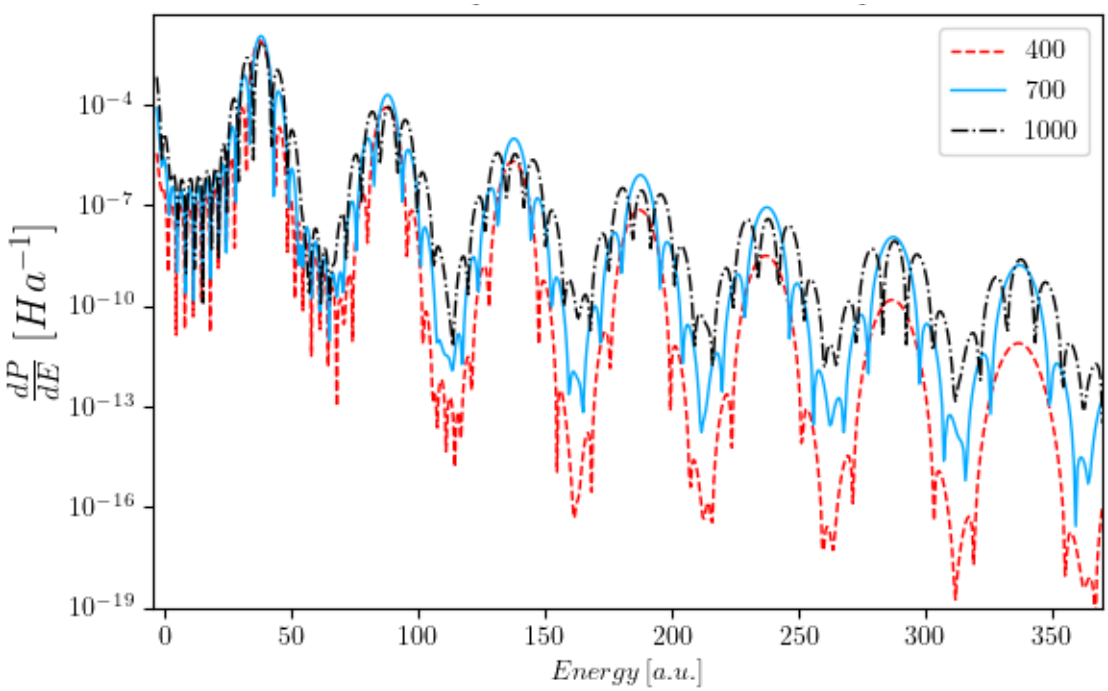

Figure 4.1.2b: Emission spectra found by propagating an eigenvalue basis from solving the 1D TISE (2.58) in B–spline basis (3.95), by applying the corresponding 1D TDSE propagator of (3.116) with

$$E_0 = \begin{cases} 400\,a.u. & \text{Red dashed line} \\ 700\,a.u. & \text{Blue solid line} \\ 1000\,a.u. & \text{Black dash-dotted line} \end{cases} \qquad \text{using SC (table 4)}$$

Inspecting fig. 4.1.2b, a pattern emerges: As the electric field strength amplitude increases, the multi–photon resonance peaks (located appx. every $n\omega + E_{g.s}\,, 1 < n \in \mathbb{Z}$, or $E_{MPR} = \{87.5,\ 137.5,\ 187.5,\ \dots\}$) become dominated by fluctuations. The black dash–dotted line in fig. 4.1.2b shows this feature especially pronounced, and the emission spectra for $E_0 = \{700,\ 1000,\ 1300\}\,a.u.$ are shown in fig. 4.1.2c below.

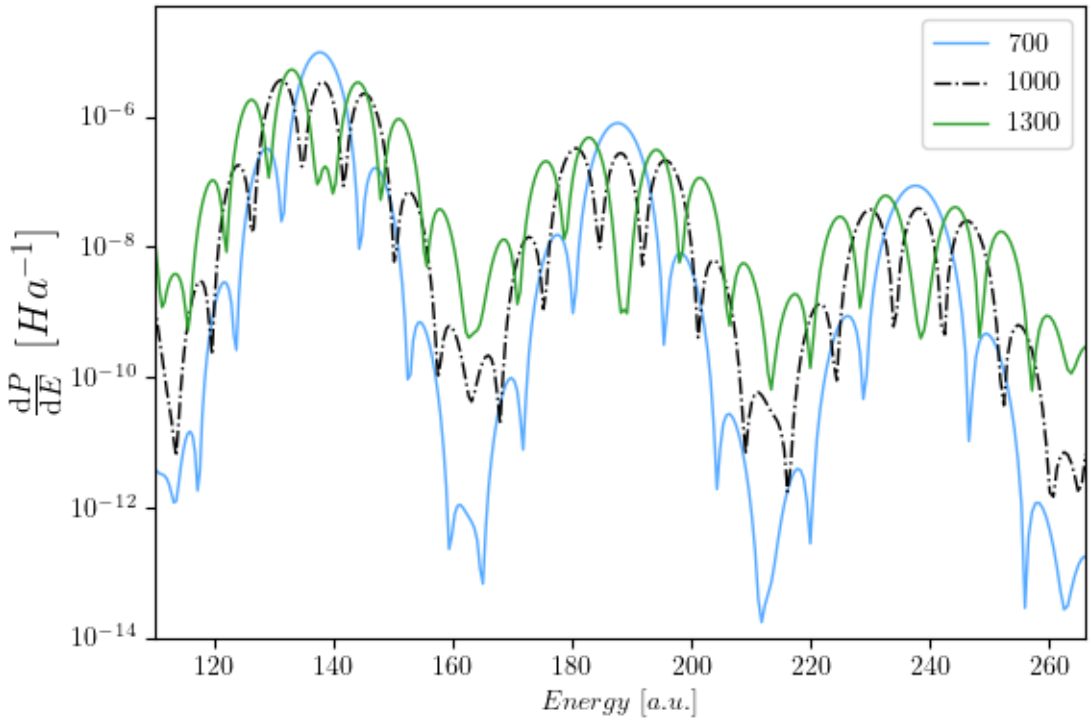

Figure 4.1.2c: $2^{\text{nd}}, 3^{\text{rd}}$ & 4^{th} photon resonance peaks of emission spectra found by propagating an eigenvalue basis from solving the 1D TISE (2.58) in B–spline basis (3.95), by applying the corresponding 1D TDSE propagator of (3.116) with $E_0 = \begin{cases} 700\,a.u. & \text{Blue solid line} \\ 1000\,a.u. & \text{Black dash-dotted line} \\ 1300\,a.u. & \text{Green solid line} \end{cases}$ using SC (table 4).

In fig. 4.1.2c, the fluctuations permeate the peaks of the $E_0 = 1300\,a.u.$ (green, solid line) to the point where the "centres of mass" are lower than the energy intervals surrounding them. Inferring from figs, 4.1.2b & c, it can be hypothesised that increasing the electric field strength amplitude E_0 by a significant amount could yield more noise–polluted curves. A reasonable proposition for the cause of these fluctuations could be found in the expression (3.118) for the vector field, quantized to facilitate numerical representation:

$$A(t_i) = \frac{E_0}{\omega} f(t_i) \sin(\omega t_i)\,, \qquad \text{with } f(t_i) \text{ as the pulse envelope.} \tag{4.1}$$

From (4.1) and assuming that the initial system is equal across all simulations using the identical eigenvalue basis (meaning e.g. the three that are illustrated in fig. 4.1.2c) in the SC (table 4), all differences in the resulting emission spectra must stem from the variation of the electric field strength amplitude E_0. One way this could produce "noise" in the time–propagation is by increasing incremental difference of the vector potential $\Delta A(t) = A(t) - A(t - \Delta t)$. Since $A(t)$ is linearly dependent on E_0, increasing the field strength by substitution as $E_0 \to nE_0$ for some $1 \ll n \in \mathbb{R}$ could significantly increase the requirements for time–resolution. That is, an increase to the electric field strength

amplitude E_0 might require a corresponding increase in the number of iterations $n_{\Delta t}$ over which the propagation must be performed, if it is to retain the resolution which can be observed at lower values of E_0. This problem, however interesting it is, does not fall directly within the main objective for the present work, and is therefore left to ponder at a later occasion.

In the previous sections 4.1.1 and 4.1.2, numerical models and solutions to the 1D TISE (2.58) represented in B–spline basis (3.95) were put forth. Subsequently, a solution of the modeled system using standard configuration (4) was utilised as a finite eigenvalue basis for the 1D TDSE time–propagator (3.116), for varying values of the electric field strength amplitude. Results from both the 1D TISE and TDSE were presented in illustrations, and some features of the emission spectra were discussed.

4.2 Numerical solution to the 1D Dirac equation

With numerical results from the non–relativistic 1D Schrödinger equation presented in sec. 4.1, this is an opportune spot to consider the corresponding results from a Dirac framework. To begin, some stationary eigenstates to the 1D TIDE (3.20) in a DKB B–spline representation (3.51) using SC (table 4) are shown.

4.2.1 Wave functions for TIDE

Solutions to the 1D TIDE (3.20) are shaped as wave spinors (2.28). Intrinsic to these solutions is the substantial difference in relative amplitude for the large and small component. As such, any results derived by solving the 1D TIDE (3.20) for a model hydrogenic atom with a soft-core potential (2.19) are presented in two parts, one for each of the large and small components. First, using SC (table 4), the large and small components of the solutions to the four lowest positive energy states are presented.

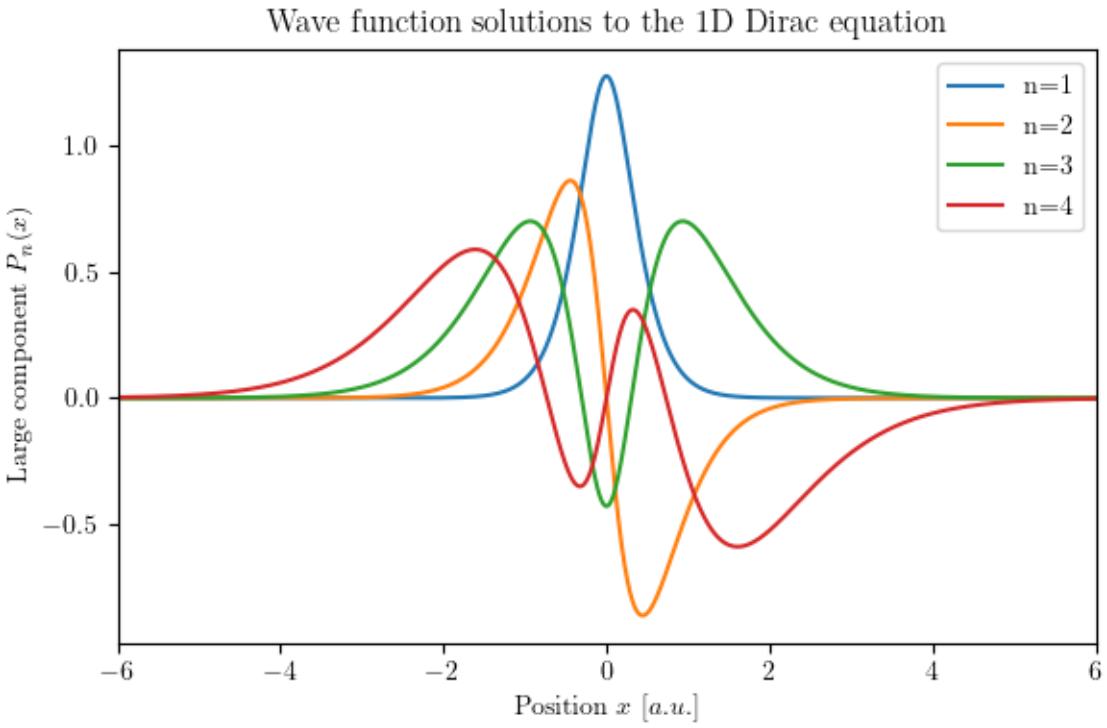

Figure 4.2.1a: Large components of the four lowest positive energy eigenstates of the 1D TIDE (3.20) in DKB B–spline representation (3.51) and SC (table 4).

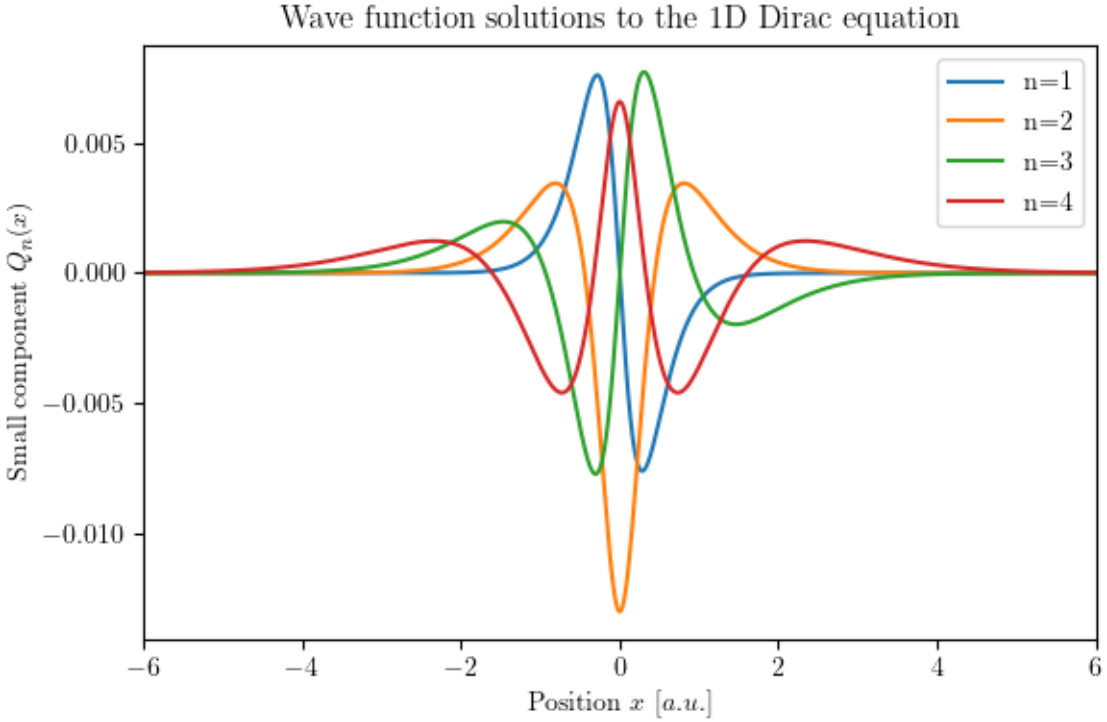

Figure 4.2.1b: Small components of the four lowest positive energy eigenstates of the 1D TIDE (3.20) in DKB B–spline representation (3.51) and SC (table 4).

When comparing Fig.4.2.1a and b with one another, it can be seen that each pair of $\begin{pmatrix} P_n \\ Q_n \end{pmatrix}$ contains exactly one odd and one even component. This infers significant implications for the Hamiltonian of interaction (3.79), specifically regarding the matrix elements $V_{k,n}$ (3.75). For clarity, $V_{k,n}$ is defined as

$$V_{k,n} = \int_b^a \left[P_k^*(x) \cdot Q_n(x) - Q_k^*(x) \cdot P_n(x)\right] \mathrm{d}x \,, \tag{4.2}$$

which can be separated to

$$V_{k,n} = \int_b^a P_k^*(x) \cdot Q_n(x) \,\mathrm{d}x - \int_b^a Q_k^*(x) \cdot P_n(x) \,\mathrm{d}x \,. \tag{4.3}$$

Examining the large and small components to positive energy solutions with more values of n, the following relation can be expressed:

$$P_n : \left\{ \begin{array}{ccc} \text{even} & \begin{pmatrix} n \\ \text{even} \end{pmatrix} & \text{odd} \\ \text{odd} & \begin{pmatrix} n \\ \text{odd} \end{pmatrix} & \text{even} \end{array} \right\} : Q_n \tag{4.4}$$

Now, as the product of one odd and one even function is an odd function, and the integral of a well–defined odd function $F_{odd}(x)$ in the interval interval $(-a, a)$ yields $\int_{-a}^{a} F_{odd}(x)\mathrm{d}x = 0$, the following expression can be made for the matrix elements of (4.3):

$$V_{k,n} = 0 \quad \forall \quad (k,n) \in \mathbb{Z} \quad \text{such that} \qquad k \mod 2 \equiv n \mod 2 \tag{4.5}$$

In other words, if the matrix elements $V_{k,n}$ for positive energy solutions were laid out on a chess board, you should only expect to find non–zero values in either the black or the white squares. Now, as the method used to express the components P_n and Q_n is a numerical one, the identity laid out in (4.5) is not exact. Using the MATPLOTLIB.PYPLOT.SPY() functionality on this matrix with precision 10^{-11} still results in a chess pattern, as illustrated below.

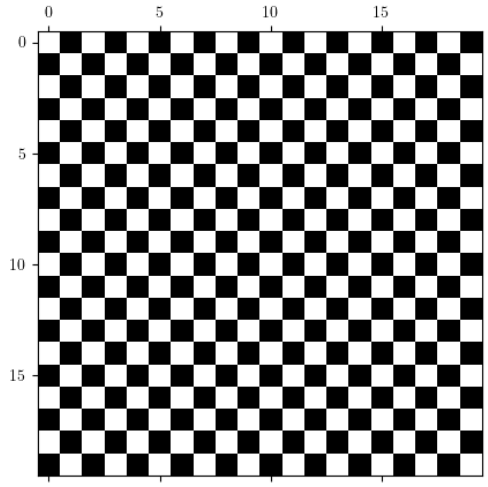

Figure 4.2.1c: Near–zero ($|V_{k,n}| < 10^{-11}$) [white squares] and non-zero [black squares] values in the matrix elements of $V_{k,n}$ (4.3) obtained by solving the 1D TIDE (3.20) in DKB B–spline representation (3.51) and SC (table 4).

From this result, it would seem that pairs of states which fulfil the condition for (k, n) laid out in (4.5) will interact singificantly less than (k, n)–pairings of states which do not fulfill the condition. In fact, this can immediately be seen when graphing out the resulting emission spectra given by time–propagation in (3.91).

4.2.2 Emission spectra for TDDE

Before proceeding to the numerical results to the modeled 1D TDDE (2.43), it is useful to retrace the steps leading up to this. First, the 1D TIDE (3.20) was solved in a DKB B–spline representation (3.51) using the Standard Configuration (4). A basis consisting of the eigenstate solutions to the 1D TIDE was then constituted, and the time–indepentent parts of the matrix elements in $V_{k,n}$ (3.75) were determined by integration. This matrix, as well as the eigenvalues to the 1D TIDE, is then passed on to the model time–propagator (3.91), which governs the time–evolution of the initial system while it interacts with the laser pulse (3.118). Ultimately, the entire process yields some vector $\vec{c}(t = T)$ containing the coefficients for each energy state in the post–interaction modeled system, enabling some representation of the energy probability differential (3.120) so that the emission spectra can be investigated.

The first figure of this subsection ties in heavily with fig. 4.2.1.c and the identity for $V_{k,n}$ presented in (4.5).

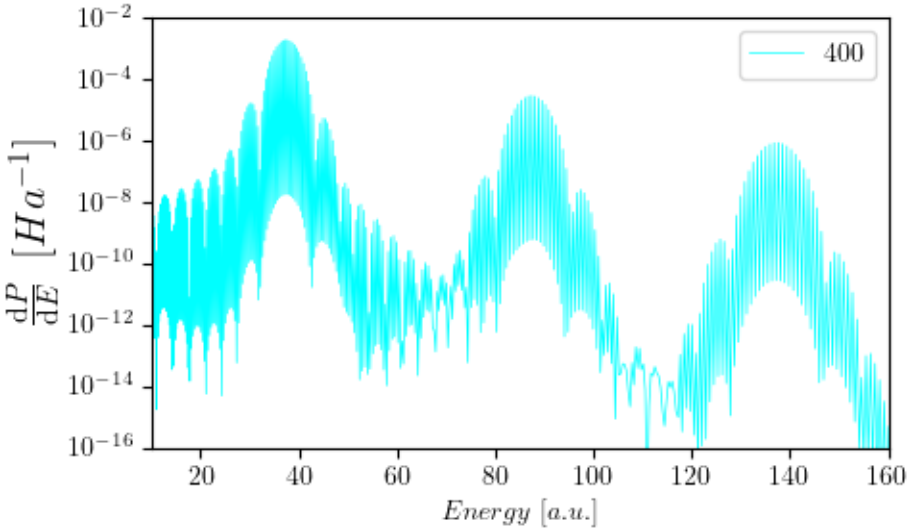

Figure 4.2.2a: Emission spectra found by propagating an eigenvalue basis from solving the 1D TIDE (3.20) in DKB B–spline basis (3.51), by applying the corresponding 1D TDDE propagator of (3.91) with $E_0 = 400\,a.u.$ using SC (table 4).

Figure 4.2.2a shows some glaring issues, and appear almost as if there are two emission spectra layered on top of each other. This appearance is not entirely false either, and looking at fig. 4.2.2b (which has the same data input as fig. 4.2.2a),

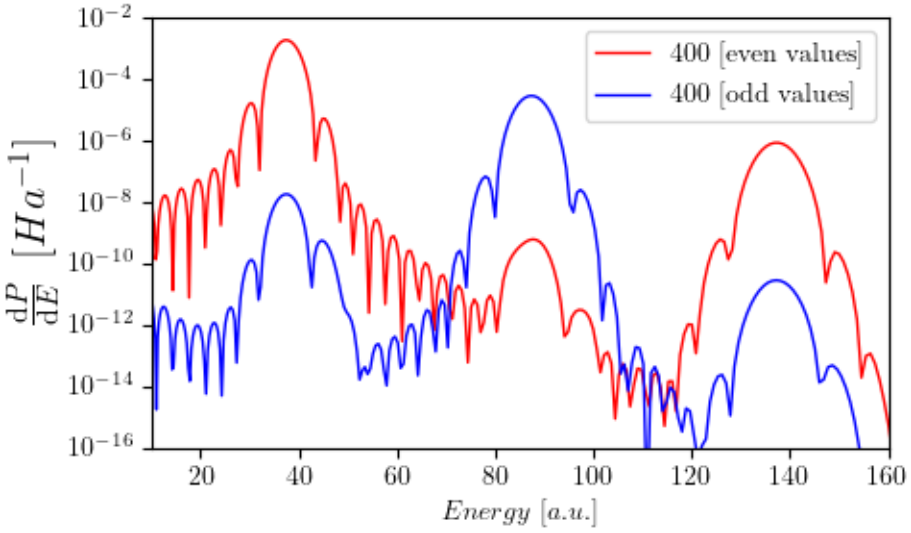

Figure 4.2.2b: Emission spectra found by propagating an eigenvalue basis from solving the 1D TIDE (3.20) in DKB B–spline basis (3.51), by applying the corresponding 1D TDDE propagator of (3.91) with $E_0 = 400\,a.u.$ using SC (table 4). Values are separated into odd [blue] and even [red] indices of the coefficient $c_i(t = T)$.

there are striking similarities. In 4.2.2a, the area which has been scrawled out is identical to the area which is encased by the emission spectra drawn in fig. 4.2.2b. The mechanism responsible for this splitting of the emission spectra is, or so I would think, related to the structure of the interaction matrix, specifically in the relation (4.5). Having become aware of this peculiarity, it can be accounted for by interpolating them to the same array of energy states. Subsequently, some emission spectra (corresponding to the electric field strength amplitudes E_0 that were in sec. 4.1.2 for the Schrödinger framework) will be illustrated in the below figures.

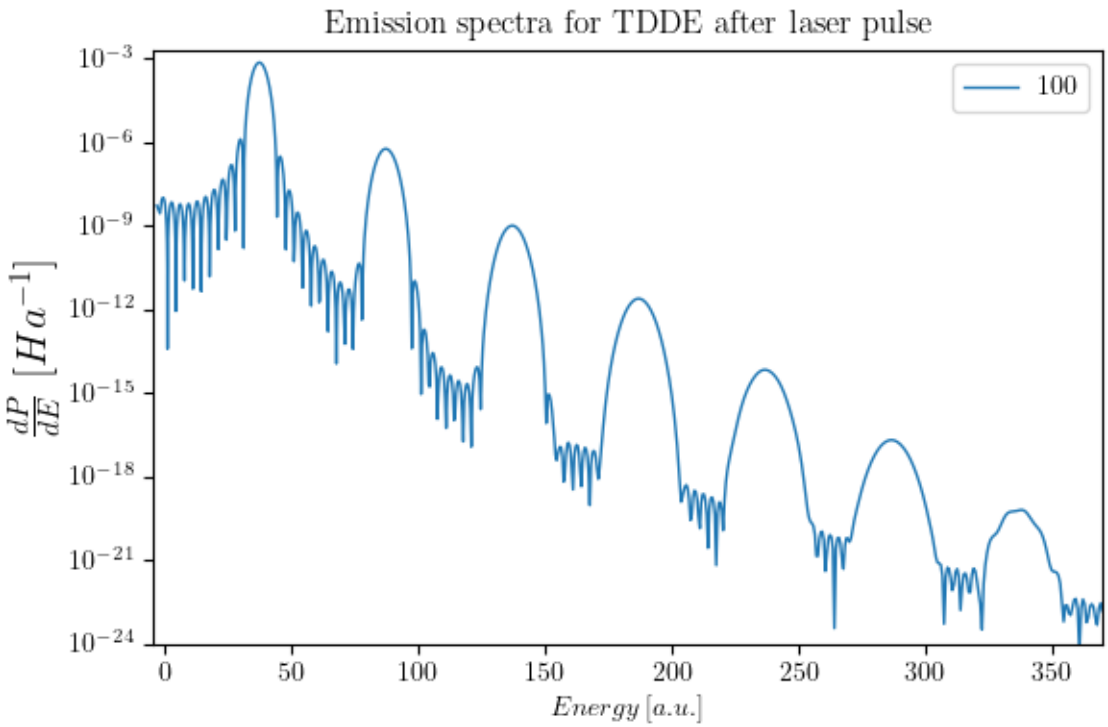

Figure 4.2.2c: Emission specter found by propagating an eigenvalue basis from solving the 1D TIDE (3.20) in DKB B–spline basis (3.51), by applying the corresponding 1D TDDE propagator of (3.91) with $E_0 = 100\, a.u.$ using SC (table 4).

Fig. 4.2.2c has been displayed above to illustrate the breakdown of the emission spectra into machine precision "noise". An explaination for this phenomenon has already been given, in the paragraph immediately succeeding fig. 4.1.2a.

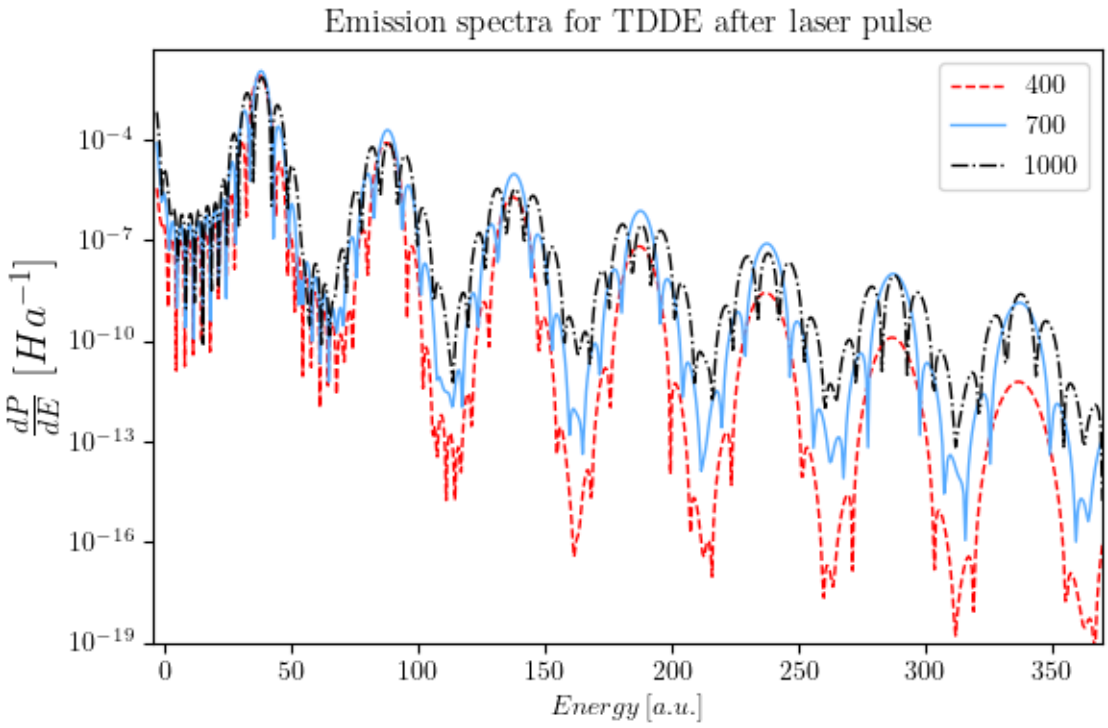

Figure 4.2.2d: Emission spectra found by propagating an eigenvalue basis from solving the 1D TIDE (3.20) in DKB B–spline basis (3.51), by applying the corresponding 1D TDDE propagator of (3.91)

$$\text{with } E_0 = \begin{cases} 400\,a.u. & \text{Red dashed line} \\ 700\,a.u. & \text{Blue solid line} \\ 1000\,a.u. & \text{Black dash-dotted line} \end{cases} \quad \text{using SC (table 4).}$$

Again for the sake of comparison, the emission spectra of three different electric field strength amplitudes E_0 are plotted on the same axis. The fluctuations that were discussed in the paragraph below fig. 4.1.2b and beneath 4.1.2c can also be spottet in the emission spectra hailing from time–evolution by the 1D TDDE (3.91).

To summarise section 4.2, the emission spectra which was produced by inserting an eigenvalue basis, which was obtained by solving the 1D TIDE (3.20) for a hydrogenic atom in a soft–core potential (2.19) in a DKB B–spline representation (3.51), into the time–evolution propagator 3.91 for the 1D TDDE (3.67). Using results from section 4.1 and 4.2, as well as some not–yet introduced results, the next section will attempt to find some perspective on how the shifts in the emission spectra for the Dirac and Schrödinger models which was presented in fig. 1.3 (red/blue shift), as well as in section 1.5.

4.3 Shifts in the emission spectra of the 3D Dirac and Schrödinger equation

To start off this section, it seems appropriate to shed some light on the background for the main problem of the current thesis. In previous studies [7, 8, 20, 23, 14] of the light-matter interactions of some numeric model of a hydrogenic atom in the presence of a high–intensity laser field, a shift in the emission spectra (such as the one illustrated in fig. 1.3) and/or ionization probabilities are observed when accounting for relativistic effects in calculations. These relativistic effects have been accounted for in several ways, most commonly by a) implementing some relativistic or semirelativistic corrections to the TDSE, and b) by modeling the system on some numerical adaptation of the TDDE. To observe the shift as vividly as required, M. Førre has contributed two emission spectra from numerical 3D model systems of hydrogenic atoms in the presence of a high-intensity laser pulse, both of which make use of the dipole approximation. The first emission specter is the result of some numerical, non-relativistic 3D Schrödinger system interacting with the pulse, while the second one is calculated from some relativistic 3D model system in the Dirac framework, interacting with the same pulse. For consistency, the spectra are generated with similar configurations as the SC (table 4). Specifically, the 3D emission spectra supplied by Førre, as well as the 1D emission spectra with which they are to be compared with, were made with the configurations presented in table 4.3-1 below.

Parameter	Symbol	Configuration
Proton number	Z	$Ze = 5\,a.u.$
Angular frequency	ω	$50\,a.u.$
Electric field strength amplitude	E_0	$1000\,a.u.$

Table 4.3-1: Configurations of input parameters used to model the 3D (supplied by M. Førre) and 1D (made by the author as part of the current thesis) emission spectra, for both Dirac and Schrödinger models.

With configurations as specified in table 4.3-1 above, the emission spectra from the modeled 3D hydrogenic atom are illustrated in section 4.3.1 below.

4.3.1 Emission spectra in 3D numerical models of Dirac and Schrödinger systems

From the outset (and to amend for the fairly inaccurate provisional illustration displayed in fig. 1.3), the emission spectra for the 3D Dirac and Schrödinger models supplied by M. Førre are presented in figures 4.3.1a+b.

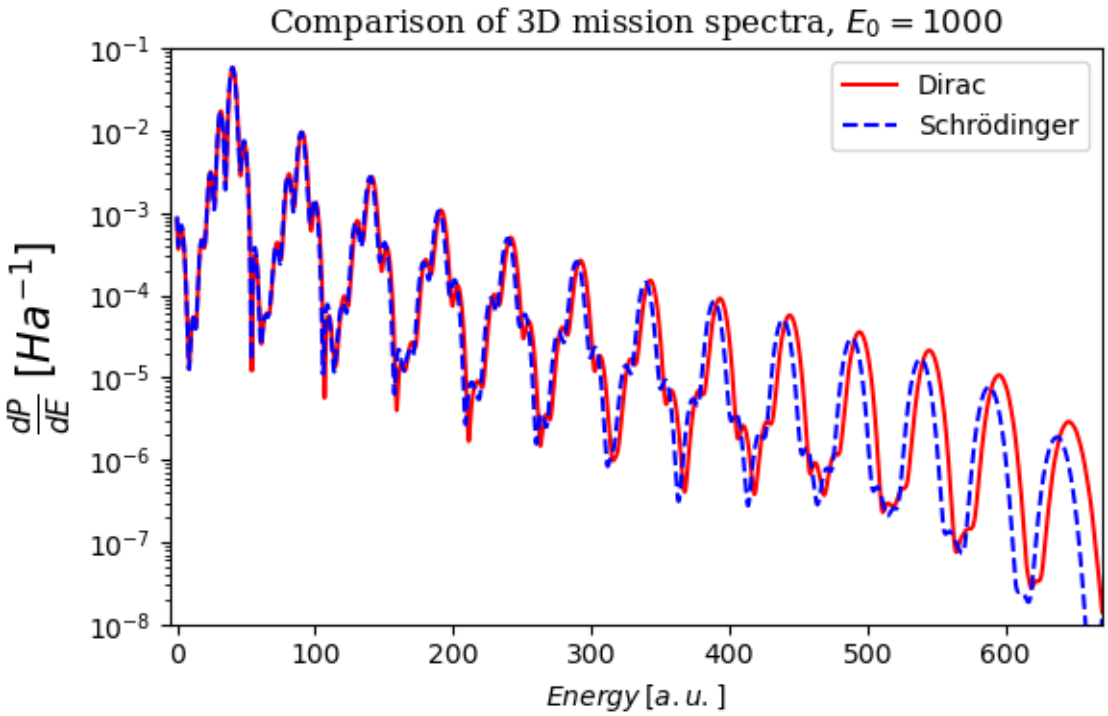

Figure 4.3.1a: Emission spectra obtained by solving the 3D TDDE (red line) and TDSE (blue dashed line) for some numerical dipole approximation model hydrogenic atom in a high-intensity laser pulse. Data supplied by M. Førre.

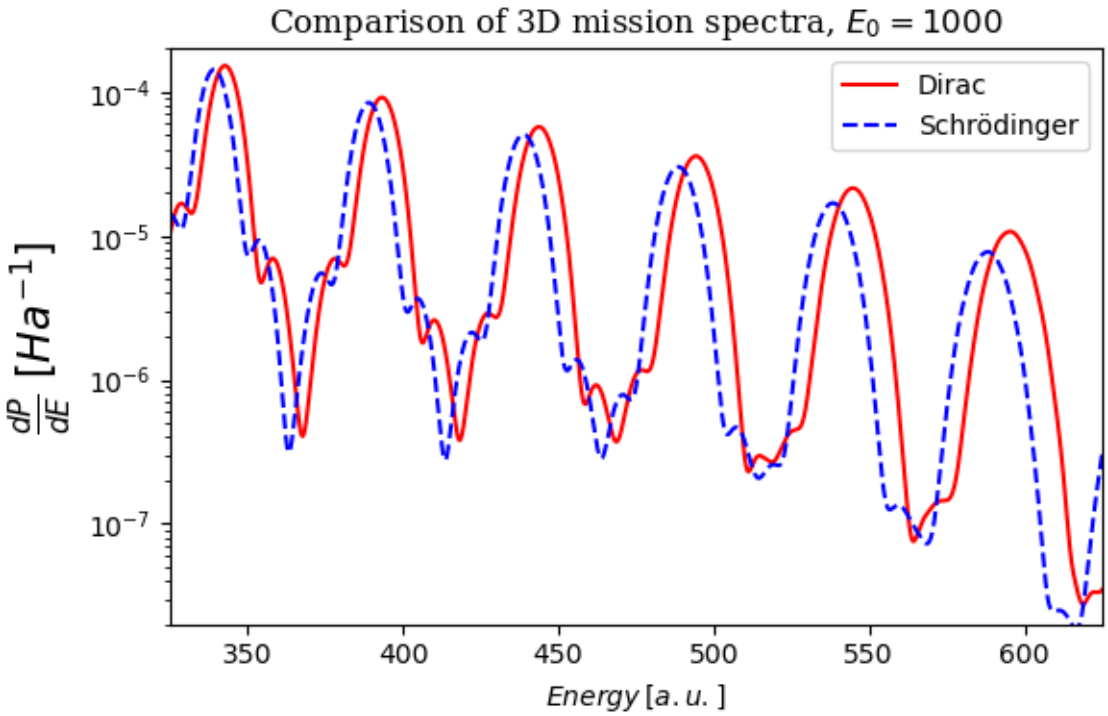

Figure 4.3.1b: Emission spectra obtained by solving the 3D TDDE (red line) and TDSE (blue dashed line) for some numerical dipole approximation model hydrogenic atom in a high-intensity laser pulse. Identical data set as fig. 4.3.1, upscaled for ease of inspection. Data supplied by M. Førre.

The data presented in figs. 4.3.1a & b clearly illustrates the shift occurring in the energy specter of a Dirac modeled system when compared to the non-relativistic Schrödinger model. Closer inspection of the peaks reveal that the multiphoton resonances from the Schrödinger emission specter has peaks in very close proximity to nonrelativistic expectations (as explained in the paragraph succeeding fig. 4.1.2). On the other hand, in the relativistic regime governed by the Dirac equation, the multi-photon resonence peaks are shifted further apart.

Now having discussed the data provided by Førre, it is time to compare the emission spectra of the 1D TDDE and TDSE models, for which illustrations have already been shown in sec. 4.1&4.2.

4.3.2 Comparison of emission spectra of 1D TDDE and TDSE model atoms

The process for finding the results that are presented within the current section has been discussed in detail in the final paragraphs of section 4.1.2 (for the numerical solutions in the Schrödinger framework) and section 4.2.2 (in the Dirac framework). The figures 4.3.2a & b below are framed and configured to be as similar to figs. 4.3.1a & b as possible, to make for easier comparison.

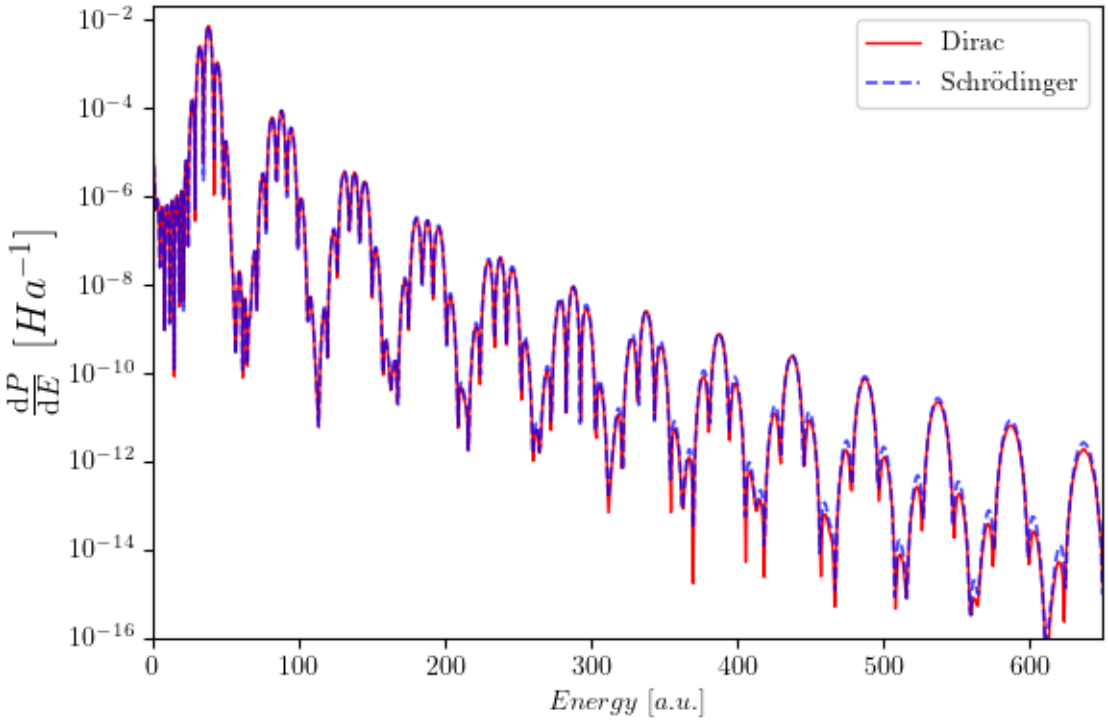

Figure 4.3.2a: Emission spectra found by propagating an eigenvalue basis from (1) solving the 1D TIDE (3.20) in DKB B–spline basis (3.51), by applying the corresponding 1D TDDE propagator of (3.91) (red, solid line), and (2) solving the 1D TISE (2.58) in B–spline basis (3.95), by applying the corresponding 1D TDSE propagator of (3.116) (dashed blue line). Both systems are propagated with $E_0 = 100\,a.u.$ in SC (table 4).

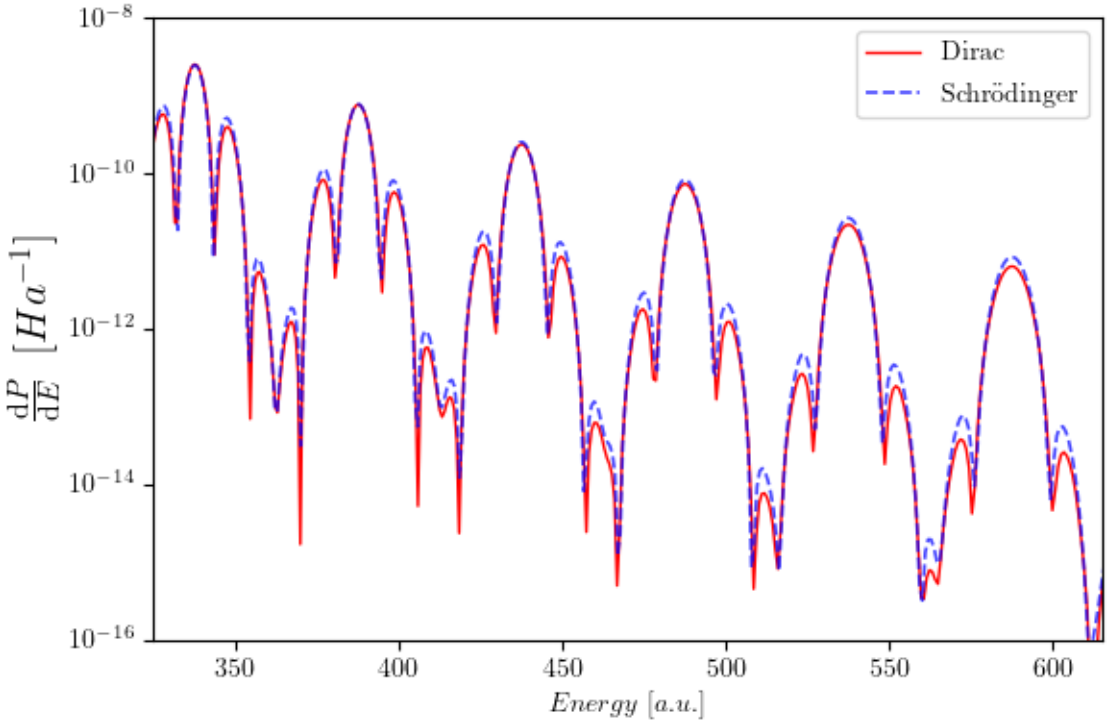

Figure 4.3.2b: Emission spectra found by propagating an eigenvalue basis from (1) solving the 1D TIDE (3.20) in DKB B–spline basis (3.51), by applying the corresponding 1D TDDE propagator of (3.91) (red, solid line), and (2) solving the 1D TISE (2.58) in B–spline basis (3.95), by applying the corresponding 1D TDSE propagator of (3.116) (blue, dashed line). Both systems are propagated with $E_0 = 1000\, a.u.$ in SC (table 4). Upscaled for ease of inspection.

From looking at these graphs, it is immediately apparent that the shift which was present in the emission specter hailing from the 3D Dirac modeled system, as in fig. 4.3.1a & b. Notwithstanding some differences in amplitude, the emission spectra of the 1D Dirac model (red line) and 1D Schrödinger model (blue dashed line) in figs. 4.3.2a & b are practically identical. Furthermore, this also seems to be the case for propagating either of the modeled systems in every electric field strength amplitude E_0 attempted throughout this work. Further illustrations are shown in fig. 4.3.2c below.

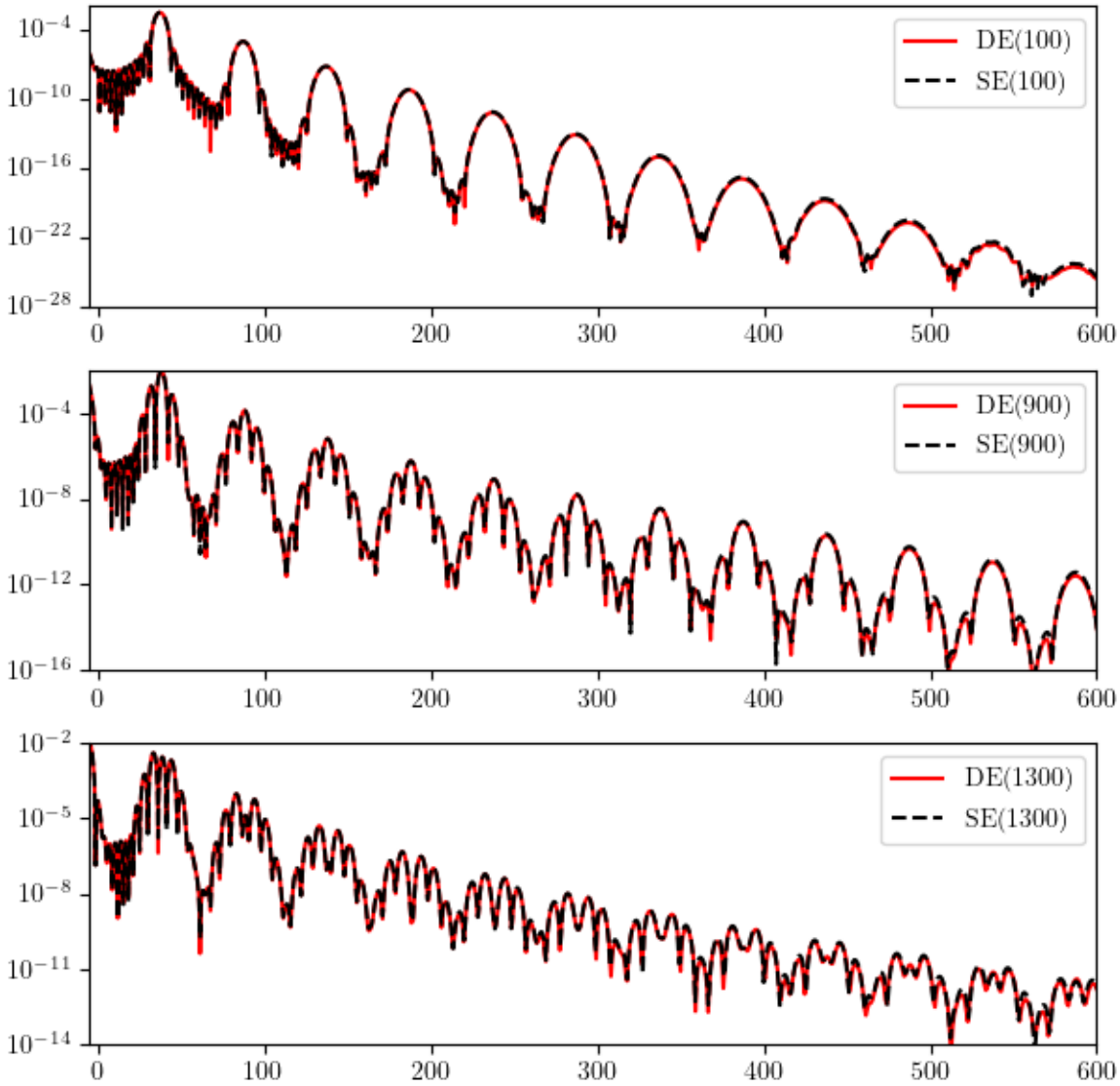

Figure 4.3.2c: Emission spectra found by propagating an eigenvalue basis from (1) solving the 1D TIDE (3.20) in DKB B–spline basis (3.51), by applying the corresponding 1D TDDE propagator of (3.91) (red, solid line), and (2) solving the 1D TISE (2.58) in B–spline basis (3.95), by applying the corresponding 1D TDSE propagator of (3.116) (black, dashed line). Both systems are propagated

$$\text{with } E_0 = \begin{cases} 100\,a.u. \\ 900\,a.u. \\ 1300\,a.u. \end{cases} \quad \text{in SC (table 4).}$$

From inspection of figure 4.3.2c, there is still no sign at all of the shift which could clearly be seen in fig 4.3.1a & b. With intent to determine whether the two models produce near-identical emission spectra for every E_0, figure 4.3.2d will contain data for 15 values of E_0, for both the 1D modeled atoms.

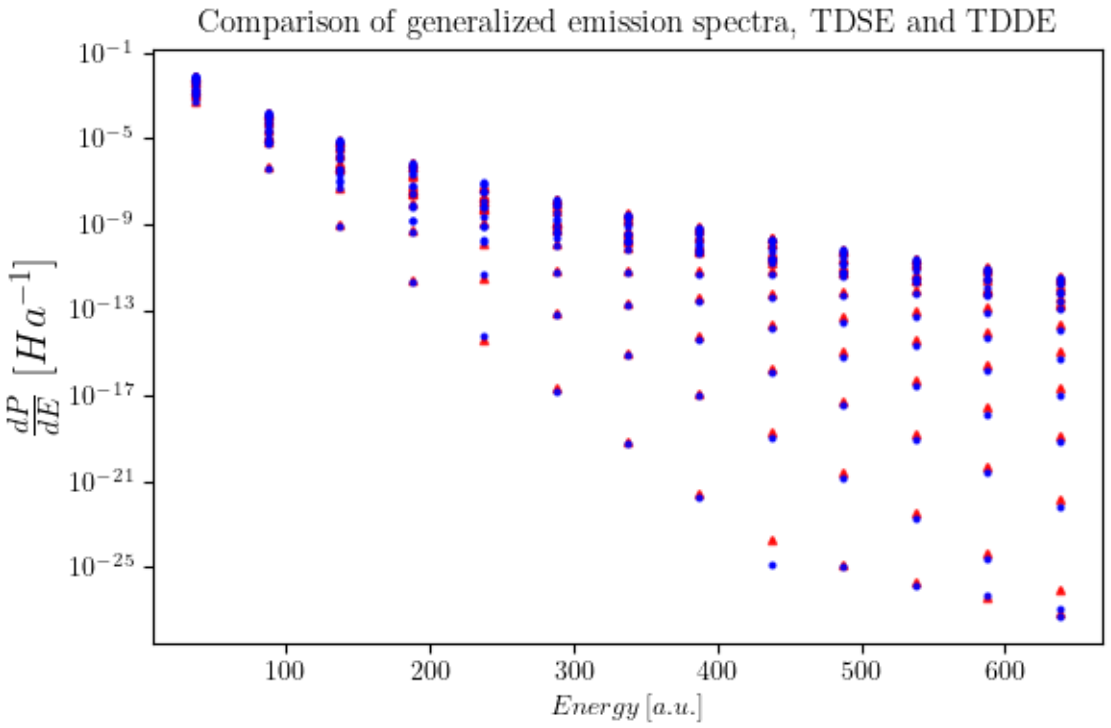

Figure 4.3.2d: Centre-of-mass approximations for the emission spectra of the numeric models of hydrogenic atoms after exposure to a high-intensity laser pulse. Results were found using the Dirac (red triangles, see sec. 4.2.2) and Schrödinger (blue dots, see sec. 4.1.2) systems using SC (table 4).

In the centre-of-mass plot from fig. 4.3.2, the y-value of each data point is determined individually for both the the 1D TDDE and TDSE models, for each electric field strength ampliture $E_0 = \{100, 200, \dots, 1400, 1500\}$, by finding the average y–value on the curve within an energy interval of $\pm 5\, a.u.$ of each peak. Although there is a noticeable difference between them, it does not give much in the way of energy shifts as the 3D model presented. For the sake of comparing the emission spectra of the 1D modeled systems to the 3D results provided by Førre, figure 4.3.2e is given below.

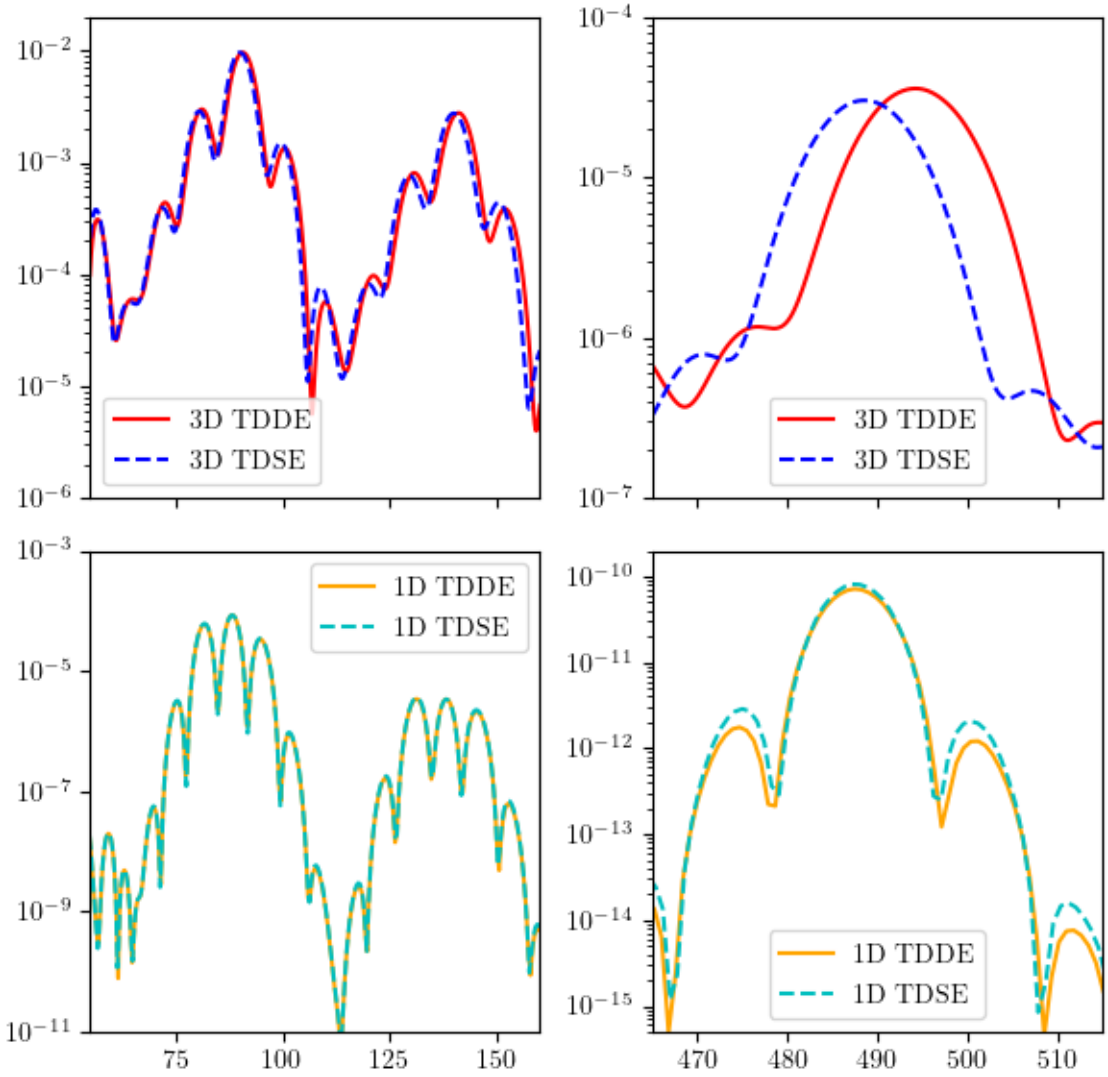

Figure 4.3.2e: Comparison of emission spectra with $E_0 = 1000\,a.u.$ for 4 different numeric models. Upper axes: Both 3D results are provided by M. Førre. 3D TDSE (dashed, blue line) and 3D TDDE (solid, red line). Lower axes: Results from 1D TDSE (dashed, green line) and 1D TDDE (solid, yellow line). All emission spectra use the configurations listed in table 4.3-1. 1D simulations also use SC (table 4).

From fig. 4.3.2e, one immediately apparent difference in the 1D and 3D emission spectra is the amplitude present in them. By some numeric or physical mechanism, it would seem that the 1D electron is less likely to interact with the electric field than an electron existing in a 3D modeled world is.

4.4 Ionization probability after exposure to a high-intensity laser pulse

As the results of the 1D TDDE model show no observable shift in the emission spectra, it can be useful to instead consider another potential use for the data sets produced over the course of the present work. Previous research has shown that relativistic effects, acting in some light-matter interaction for a numerical model hydrogenic atom in the presence of a high-intensity laser pulse, can manifest their influence in the ionization probability for the modeled system [14, 23]. To investigate this, the results (for which the method of obtaining have been discussed in sec. 4.1.2 (TISE) and 4.2.2 (TIDE)) are sorted by which electric field strength amplitude E_0 they were exposed to, as well as which model they were based on. Finding the probability of ionization after some model has been exposed to the high–intensity laser pulse can be done in the following way.

All systems have their initial state as the ground state ($c_{g.s.}(0) = 1$, $c_{i \neq g.s.}(0) = 0$). Ionization happens as the electron obtains enough energy break out of the central potential of the modeled atom, an as such the probability of ionization can be determined from the sum coefficients corresponding to unbound energy states at some point after the pulse has imparted its effect on the system. To be more precise, the probability of ionization for some system represented in an eigenvalue basis containing N eigenstates – of which the lowest n correspond to bound states – can be expressed as the series given below.

$$P_{ion} = \sum_{i=n+1}^{N} |c_i(T_{fin})|^2 \quad \text{for some } n \text{ such that } E_j > 0 \; \forall \; j > n \tag{4.6}$$

Inserting the same solutions as were illustrated in fig. 4.3.2d into eq. 4.6 yields results which are displayed in figure 4.3.3a, below.

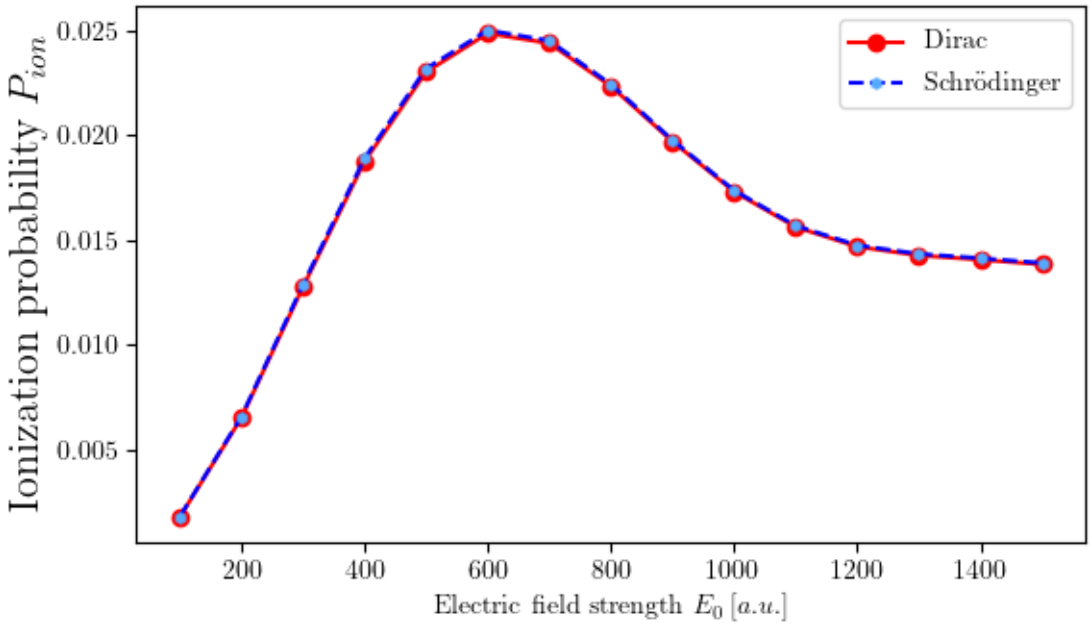

Figure 4.3.2d: Ionization probability for 1D Dirac and Schrödinger model atoms after being exposed to some high–intenstity laser pulse.

The resulting graph for the ionization probability is in agreement with the emission spectra from sec. 4.3.2: Relativistic effects are not noticeable in this modeled system.

4.5 Inclusion of negative energy states in the Dirac eigenvalue basis

During a meeting with my supervisor some days before the deadline for this thesis, we came to the realisation that the negative energy solutions from the 1D TIDE (3.20) had not included in the eigenvalue basis used to solve the TDDE 3.91. Neglecting to include these negative energy states in the eigenvalue basis has prevented the Dirac modeled system from exhibiting such relativistic effects that would cause a shift illustrated in figs. 4.3.1a & b. Consequently, the 1D TDDE must be solved by employing a slightly adjusted method, as will be described in the next paragraph.

To begin, the 1D TIDE (3.20) for a hydrogenic atom in a soft–core potential (2.19) is solved in the DKB B–spline representation (3.51). These solutions, now including both positive and negative energy solutions, are used to solve the 1D TDDE (3.67) by using the propagator from (3.91). The emission specter for the 1D Schrödinger model presented in fig. 4.3.2b is also illustrated, as well as the emission spectra provided by M. Førre.

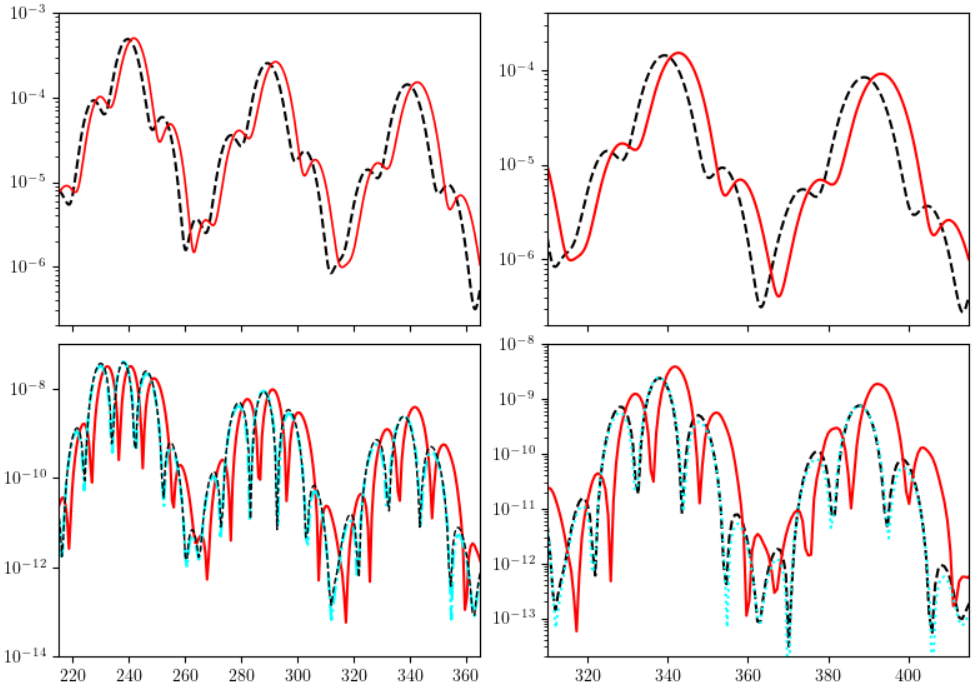

Figure 4.5a: Comparison of emission spectra approximated by the differential probability energy distribution $\frac{\mathrm{d}P}{\mathrm{d}E}$ with $E_0 = 1000\,a.u.$ for 5 different numeric models. Upper axes: Both 3D results are provided by M. Førre. 3D TDSE (dashed, black line) and 3D TDDE (solid, red line). Lower axes: Results from 1D TDSE (dashed, black line), 1D TDDE **without** negative energy states (dotted, cyan line). and 1D TDDE **with** negative energy states (solid, red line) All emission spectra use the configurations listed in table 4.3-1.

With the inclusion of negative energy states to the eigenvalue basis propagated in the 1D TDDE (3.91), a shift in the emission spectra caused by relativistic effects in the light-matter interaction with the high-intensity laser pulse is can be observed. For further inspection, the 1D spectra are displayed for a wider range of energy values in fig. 4.5b.

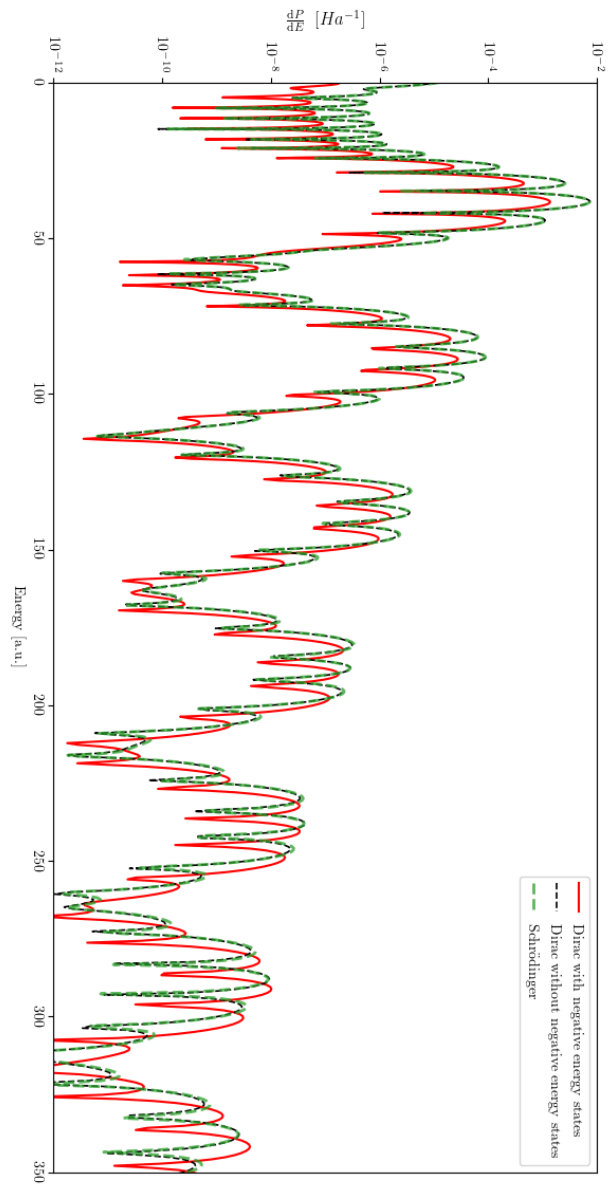

Figure 4.5b: Comparison of the probability differentials with regards to energy found by propagating an eigenvalue basis from (1): solving the 1D TIDE (3.20) in DKB B–spline basis (3.51), then applying the corresponding 1D TDDE propagator of (3.91) to the eigenvalue basis with (red, solid line) and without (black, dashed line) inclusion of the negative energy states; and (2): solving the 1D TISE (2.58) in B–spline basis (3.95), by applying the corresponding 1D TDSE propagator of (3.116) (green, dashed line). All modeled systems are propagated with the electric field strength amplitude $E_0 = 1000\, a.u.$

Chapter 5

Discussion, conclusion and future prospects

In the current work, a modeled one-dimensional hydrogenic system within a soft-core potential has been considered through varying methods and perspectives. The feasibility of representing the solutions of the 3D radial TISE (3.13) in a B-spline basis (3.15) was discussed. Following this, a similar method was implemented to solve the 1D TISE (2.58) for some one-dimensional model of a hydrogenic atom, for which the central potential was approximated as a soft-core potential (2.19) to avoid the singularity in $x = 0$. The process of representing solutions in a B-spline basis was subsequently applied to the 1D TIDE, and three approaches to achieve this were described and evaluated. Ultimately, the first two attempts were discarded in favour of the DKB representation (3.51), due to the prevalence of spurious states caused by expressing the eigenstates in the first two approaches.

After finding numerical solutions to the time-independent modeled systems for both the Dirac and Schrödinger equation, these solutions were taken as eigenvalue bases to inspect the time-evolution of the modeled systems when exposed to some modeled high-intensity laser pulse. An expression for predicting this time-evolution was derived by restructuring the time-dependent forms of both the 1D Dirac and Schrödinger equation to a time-propagator. This propagator was further simplified by requiring that it only operate in small, sequential intervals, thus making the matrix exponential contained within it Riemann-integrable. With a numerically solvable time-propagator, the modeled systems were evolved in time through sequential solutions to the eigenvalue problem posed for each time-step. In applying this propagator to the system, the light-matter interaction between the high-intensity laser pulse and the modeled 1D atom was examined. Through graphical representations, the relativistic effects seen in the 3D data could not be observed in the one-dimensional system. Furthermore, results obtained from solutions of the Dirac and Schrödinger equation yielded near-identical results. In some later calculations, the negative energy solutions of the modeled 1D TIDE were included in the basis for the time-propagator, revealing a shift of similar magnitude to the one observed from the 3D modeled system.

To answer the main problem put forth in the introduction: Yes. It is possible to observe relativis-

tic light-matter interactions between some one-dimensional model and a high-intensity laser pulse. Whether this implies that the shift is a real, physical mechanism or not does not fall under the perview of this thesis to formulate a definitive answer to. Additionally, knowledge that this relativistic effect can be described in a one-dimensional system could be of potential help for someone attempting to disentangle these interactions at a later date.

Bibliography

[1] H Bachau, E Cormier, P Decleva, J E Hansen, and F Martín. Applications ofB-splines in atomic and molecular physics. *Reports on Progress in Physics*, 64(12):1815–1943, nov 2001.

[2] Harold Cohen. *Integration*, pages 105–168. Springer New York, New York, NY, 2011.

[3] Carl De Boor. A practical guide to splines, 1978.

[4] G. W. F. Drake and S. P. Goldman. Application of discrete-basis-set methods to the dirac equation. *Phys. Rev. A*, 23:2093–2098, May 1981.

[5] F. Fillion-Gourdeau, E. Lorin, and A. D. Bandrauk. Galerkin method for unsplit 3-d dirac equation using atomically/kinetically balanced b-spline basis. *Journal of Computational Physics*, 307:122–145, 2016.

[6] M. Førre, J. P. Hansen, L. Kocbach, S. Selstø, and L. B. Madsen. Nondipole ionization dynamics of atoms in superintense high-frequency attosecond pulses. *Phys. Rev. Lett.*, 97:043601, Jul 2006.

[7] Morten Førre. Breakdown of the nonrelativistic approximation in superintense laser-matter interactions. *Phys. Rev. A*, 99:053410, May 2019.

[8] Morten Førre and Sølve Selstø. Schrödinger formulation of the nondipole light-matter interaction consistent with relativity. *Physical review. A*, 2020.

[9] David J. Griffiths and Darrell F. Schroeter. *Introduction to quantum mechanics*. Cambridge University Press, 2018.

[10] Richard L. Hall, Nasser Saad, K. D. Sen, and Hakan Ciftci. Energies and wave functions for a soft-core coulomb potential. *Phys. Rev. A*, 80:032507, Sep 2009.

[11] Walter C. Henneberger. Perturbation method for atoms in intense light beams. *Phys. Rev. Lett.*, 21:838–841, Sep 1968.

[12] J. D. Hunter. Matplotlib: A 2d graphics environment. *Computing in Science & Engineering*, 9(3):90–95, 2007.

[13] Jacek Karwowski, Artur Ishkhanyan, and Andrzej Poszwa. The eigenvalue problem of one-dimensional dirac operator. *Theoretical Chemistry Accounts*, 139(12), nov 2020.

[14] Tor Kjellsson, Sølve Selstø, and Eva Lindroth. Relativistic ionization dynamics for a hydrogen atom exposed to superintense xuv laser pulses. *Phys. Rev. A*, 95(4), Apr 2017.

[15] N. J. Kylstra, A. M. Ermolaev, and C. J. Joachain. Relativistic effects in the time evolution of a one-dimensional model atom in an intense laser field. *Journal of Physics B: Atomic, Molecular and Optical Physics*, 30(13):L449–L460, jul 1997.

[16] Tom Lyche, Carla Manni, and Hendrik Speleers. *Foundations of Spline Theory: B-Splines, Spline Approximation, and Hierarchical Refinement*, pages 1–76. Springer International Publishing, Cham, 2018.

[17] Franz Mandl and Graham Shaw. *Quantum field theory*. John Wiley & Sons, 2010.

[18] Daniel C. Mattis. How to reduce practically any problem to one dimension. In Jakob Bernasconi and Toni Schneider, editors, *Physics in One Dimension*, pages 3–10, Berlin, Heidelberg, 1981. Springer Berlin Heidelberg.

[19] K J Meharg, J S Parker, and K T Taylor. Beyond the dipole approximation for helium and hydrogen in intense laser fields. *Journal of Physics B: Atomic, Molecular and Optical Physics*, 38(3):237–254, jan 2005.

[20] Thore Espedal Moe and Morten Førre. Ionization of atomic hydrogen by an intense x-ray laser pulse: An ab initio study of the breakdown of the dipole approximation. *Phys. Rev. A*, 97:013415, Jan 2018.

[21] John C. Morrison. Modern physics for scientists and engineers, 2015.

[22] Tommy Ohlsson. *Relativistic Quantum Physics: From Advanced Quantum Mechanics to Introductory Quantum Field Theory*. Cambridge University Press, 2011.

[23] Ingunn Koren Rossland. Interaction of the hydrogen atom with laser fields: a study of relativistic effects in ionization processes. Master's thesis, 2018.

[24] M. Yu. Ryabikin and A. M. Sergeev. Stabilization window and attosecond pulse train production at atom ionization in superintense laser field. *Opt. Express*, 7(12):417–426, Dec 2000.

[25] V. M. Shabaev, I. I. Tupitsyn, V. A. Yerokhin, G. Plunien, and G. Soff. Dual kinetic balance approach to basis-set expansions for the dirac equation. *Physical Review Letters*, 93(13), September 2004.

[26] A. A. Silaev, M. Yu. Ryabikin, and N. V. Vvedenskii. Strong-field phenomena caused by ultrashort laser pulses: Effective one- and two-dimensional quantum-mechanical descriptions. *Phys. Rev. A*, 82:033416, Sep 2010.

[27] Andreas Skeidsvoll. Modeling interactions between hydrogen-like atoms and intense laser pulses with the Dirac equation. Master's thesis, 2018.

[28] Nicolas Teeny, Enderalp Yakaboylu, Heiko Bauke, and Christoph H. Keitel. Ionization time and exit momentum in strong-field tunnel ionization. *Phys. Rev. Lett.*, 116:063003, Feb 2016.

[29] The LyX Team. LyX 1.6.1 - The Document Processor [Computer software and manual]. Internet: http://www.lyx.org, 2009. Retrieved February 16, 2009, from http://www.lyx.org.

[30] Eite Tiesinga, Peter Mohr, David Newell, and Barry Taylor. Codata recommended values of the fundamental physical constants: 2018. (93), 2021-06-30 04:06:00 2021.

[31] Morten Tysse. Laser-atom interactions in the Dirac equation for hydrogen. Master's thesis, 2018.

[32] Pauli Virtanen, Ralf Gommers, Travis E. Oliphant, Matt Haberland, Tyler Reddy, David Cournapeau, Evgeni Burovski, Pearu Peterson, Warren Weckesser, Jonathan Bright, Stéfan J. van der Walt, Matthew Brett, Joshua Wilson, K. Jarrod Millman, Nikolay Mayorov, Andrew R. J. Nelson, Eric Jones, Robert Kern, Eric Larson, C J Carey, İlhan Polat, Yu Feng, Eric W. Moore, Jake VanderPlas, Denis Laxalde, Josef Perktold, Robert Cimrman, Ian Henriksen, E. A. Quintero, Charles R. Harris, Anne M. Archibald, Antônio H. Ribeiro, Fabian Pedregosa, Paul van Mulbregt, and SciPy 1.0 Contributors. SciPy 1.0: Fundamental Algorithms for Scientific Computing in Python. *Nature Methods*, 17:261–272, 2020.